

**Gas diffusion electrodes for high temperature polymer
electrolyte membrane fuel cells membrane electrode
assemblies**

by

Olivia Barron

A thesis submitted in fulfilment of the requirements for the

degree of Doctor Philosophiae

Department of Chemistry,

University of the Western Cape

Supervisor: Dr Sivakumar Pasupathi

December 2014

Student number: 2233175

Declaration

I declare that “*Gas diffusion electrodes for high temperature polymer electrolyte membrane fuel cells membrane electrode assemblies*” is my own work and that it has not been submitted for any degree or examination in any other university and that all the sources that I have used or quoted have been indicated and acknowledged by complete references.



Olivia Barron

December, 2014

Signed.....

Acknowledgements

- I firstly thank God for his love and grace that I have experienced, and for all the advantages he has provided me with in my life.
- I thank my parents for their love, support, and encouragement.
- I am profoundly grateful to Prof. Vladimir Linkov, Director of the South African Institute for Advanced Material Chemistry (SAIAMC) for affording me the opportunity to pursue my studies.
- I am thankful to Prof. Bruno G. Pollet, Director of the HySA Systems Competence Centre for his motivation and support throughout the duration of the study.
- Special thanks to Dr. Sivakumar Pasupathi, Key Program Manager at HySA Systems Competence Centre for his guidance, support and encouragement throughout the duration of the study.
- Thank you to Miranda Waldron (Centre for Imaging and Analysis, University of Cape Town), for her assistance in SEM characterisation of the samples.
- Special thanks to Dr. Lindiwe Khotseng for her support and guidance.
- Special thanks to Dr. Huaneng Su for his assistance and guidance throughout the duration of the research.
- Special thanks to the South African Department of Science and Technology (DST), whose financial contributions made this study possible.
- Thank you to the National Research Foundation (NRF) for their financial assistance.
- A very special thank you to my fellow colleagues who created a friendly and helpful work environment.

Abstract

The need for simplified polymer electrolyte membrane fuel cell (PEMFCs) systems, which do not require extensive fuel processing has led to increased study in the field of high temperature polymer electrolyte membrane fuel cells (HT-PEMFCs) applications. Although these HT-PEMFCs can operate with less complex systems, they are not without their own challenges; challenges which are introduced due to their higher operation temperature. This study aims to address two of the main challenges associated with HT-PEMFCs; the need for alternative catalyst layer (CL) ionomers and the prevention of excess phosphoric acid (PA) leaching into the CL. The first part of the study involves the evaluation of suitable proton conducting materials for use in the CL of high temperature membrane electrode assemblies (HT-MEAs), with the final part of the study focusing on development of a novel MEA architecture comprising an acid-controlling region. The feasibility of the materials in HT-MEAs was evaluated by comparison to standard MEA configurations.

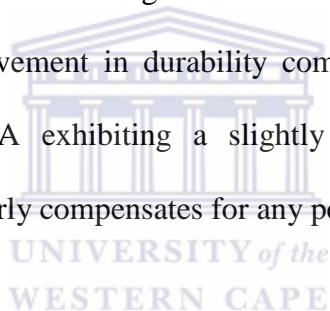
Firstly, the influence of $CsHSO_4$ inorganic solid acid was evaluated as a possible proton conductor in the CL of ABPBI (poly(2,5-benzimidazole))-based HT-PEMFCs. The gas diffusion electrodes (GDEs) were prepared by impregnating $CsHSO_4$ -binder (polytetrafluoroethylene (PTFE) or polyvinylidene difluoride (PVDF)) blends in the CLs. The binder loadings were fixed and the $CsHSO_4$ loading was varied. The microstructure of the electrodes was evaluated by mercury intrusion porosimetry (MIP) and the surface morphologies were observed by Scanning Electron Microscopy (SEM). Single cell tests and electrochemical characterisation were further performed to determine the influence of $CsHSO_4$ loading as well as the influence the $CsHSO_4$ -binder configurations had on each electrode. The GDEs containing $CsHSO_4$ in the CLs showed

good proton transfer dynamics and low resistance for fuel cell operation. An optimum loading of 10% $CsHSO_4$ in conjunction with either of the binders was observed, with $CsHSO_4$ -PVDF GDE achieving a maximum performance of 498.2 mW cm^{-2} at a cell voltage of +352 mV. A higher $CsHSO_4$ loading increased the charge transfer resistance and lowered the cell performance of these GDEs. A polymer binder is clearly required for stabilisation of $CsHSO_4$ GDEs. The failure of $CsHSO_4$ to meet the desired performance requirements led to the study of other suitable proton conducting materials.

Zirconium hydrogen phosphate (ZHP) was next evaluated as an ionomer candidate in the CL due to its good thermal stability and proton conductivity it displays at high temperatures. The ZHP, together with PTFE polymer binder was incorporated into the CLs of ABPBI (poly(2,5-benzimidazole))-based HT-PEMFCs to improve its performance and durability. The influence of ZHP content (normalised with respect to dry PTFE) on the CL properties was structurally characterised by SEM and MIP. Electrochemical analyses of the resultant membrane electrode assemblies (MEAs) revealed that a 30 wt.% ZHP/PTFE content in the CL is optimum for improving fuel cell performance, the resultant MEA delivered a peak power of 592 mW cm^{-2} at a cell voltage of 380 mV. EIS analysis indicated that 30% ZHP in the CL can increase the proton conductivity compared to the pristine PTFE-GDE. A short term stability test (~500 h) on the 30 wt.% ZHP/PTFE-GDE showed a remarkable high durability with a degradation rate as low as $\sim 19 \mu\text{V h}^{-1}$ at 0.2 A cm^{-2} , while $195 \mu\text{V h}^{-1}$ was obtained for the pristine GDE. The addition of ZHP to the CL was beneficial in terms of both performance and stability which is important for HT-PEMFCs.

The last part of the study involved the development of an acid-controlling region on the surface of the CLs. Ceramic carbides were chosen because of their good stability and

mechanical properties at the temperatures under consideration. Firstly, *SiC* layers of varying loadings were deposited onto the CL and evaluated, an optimum loading of 0.2 mg cm^{-2} was found to produce the best results compared to that of 0.5 mg cm^{-2} and 1.0 mg cm^{-2} *SiC*. Variation of the acid doping level in the *SiC* layer revealed an optimum amount of 2 mg cm^{-2} PA in the *SiC* layer produced the maximum peak power of 475 mW cm^{-2} at a cell voltage of 340 mV. The standard pristine MEA however showed a performance ~9% higher than the *SiC* MEA. Modification of the *SiC* layer with varying *NbC* contents revealed no improvement in performance. EIS analyses of the MEAs showed that the PTFE MEA had the lowest charge transfer resistance of $265, 75 \text{ m}\Omega \text{ cm}^{-2}$, followed closely by the 0.2 mg cm^{-2} *SiC* MEA with $280.80 \text{ m}\Omega \text{ cm}^{-2}$. Short-term stability analyses revealed that the 0.2 mg cm^{-2} *SiC* GDE (doped with 2 mg cm^{-2} PA) MEA showed a ~70% improvement in durability compared to the standard pristine MEA. Despite the *SiC* MEA exhibiting a slightly lower performance a ~70% improvement in durability clearly compensates for any performance losses.



Keywords

HT-PEMFCs

ABPBI

Proton conductor

CsHSO₄

ZHP

SiC

NbC

acid-controlling region



List of figures

Figure 1: Schematic of a Micro-CHP system in a household.....	2
Figure 2.1: Schematic diagram showing the basic principles of fuel cell operation	9
Figure 2.2: Characteristics of a typical polarisation curve	13
Figure 2.3: SOFC tubular design developed by Siemens-Westinghouse.....	18
Figure 2.4: Oxygen reduction at composite electrodes composed of Pt-Black (–) or Pt/ Carbon (– –) dispersed on an Au grid in contact with Nafion 117 membrane at a temperature of 50 °C, 5 mV s ⁻¹ scan rate	25
Figure 2.5: Structure of Nafion [®]	28
Figure 2.6: Effect of annealing on proton conductivity.....	29
Figure 2.7: Effect of annealing on water sorption	29
Figure 2.8: Fuel Cell performance comparison of MEAs with pristine and nanoscale oxide coated GDL using H ₂ /O ₂ at ambient pressure	31
Figure 2.9: Comparison of conventional machined channel flow fields and corrugated sheet flow fields: ◦, Corrugated sheet design with un-humidified fuel; •, Corrugated sheet design with humidified fuel; Δ, Conventional parallel flow field design with un- humidified fuel; ▲, Conventional parallel flow field design with humidified fuel.....	33
Figure 2.10: Cell voltage loss, VL, obtained experimentally with a PBI-based PEMFC with pure hydrogen and hydrogen containing different CO vol% at different temperatures.....	35
Figure 2.11: Chemical structures of (a) Poly(2,5-benzimidazole) or ABPBI and (b) Poly(2,2'- <i>m</i> -(phenylene)-5,5'-bibenzimidazole) or PBI	37
Figure 2.12: Relationship between the acid weight change by evaporation and the cell voltage drop at different cell temperatures	38

Figure 3.1: Images of (a) <i>in-house</i> HT-PEMFC test bench (b) Autopore IV Mercury intrusion porosimeter (c) high temperature single cell (d) Impedance test station: Autolab PGSTAT302 testing station.....	46
Figure 4.1: FT-IR spectra of the Cs_2SO_4 starting material, and the $CsHSO_4$ synthesised product.....	51
Figure 4.2: SEM micrographs showing the surface morphology and porous structure of GDEs prepared with various polymer binders and $CsHSO_4$ proton conductor. (a) PVDF - 200 °C; (b) PVDF and 20% $CsHSO_4$ - 120 °C; (c) PVDF and 10% $CsHSO_4$ - 120 °C; (d) PTFE and 20% $CsHSO_4$ - 120 °C; (e) PTFE and 10% $CsHSO_4$ - 120 °C; (f) 10% $CsHSO_4$ - 120 °C; (g) PTFE - 200 °C.....	53
Figure 4.3: Cumulative intrusion of the GDEs with various polymer binders and $CsHSO_4$ in the CL.....	55
Figure 4.4: Polarisation and power density curves for the MEAs with different polymer binders and $CsHSO_4$ proton conductor.....	56
Figure 4.5: Polarisation curves of the MEAs with different polymer binders and/or proton conductor in the CL of the GDEs.....	58
Figure 4.6: Power Density curves of the MEAs with different polymer binders and/or proton conductor in the CL of the GDEs.....	59
Figure 4.7: <i>In situ</i> impedance spectra of the MEAs with different polymer binders and $CsHSO_4$ at a cell voltage of 0.6V	61
Figure 4.8: <i>Tafel plots</i> for the ORR of the GDEs with different catalyst layer compositions.....	64
Figure 5.1: Surface morphologies with inserts of CL pore structure of (a) PTFE-GDE (GDE-1) and (b) 30% ZHP/PTFE-GDE (GDE-3)	68

Figure 5.2: Surface morphologies with inserts of CL pore structure of (a) 20% ZHP/PTFE-GDE (GDE-2), (b) 40% ZHP/PTFE-GDE (GDE-4) and 50% ZHP/PTFE-GDE (GDE-5).....	69
Figure 5.3: Mercury intrusion porosimetry curves showing the incremental intrusion of the PTFE-GDE (GDE-1) and the 30% ZHP/PTFE-GDE (GDE-3)	70
Figure 5.4: Mercury intrusion porosimetry curves showing the incremental intrusion for the GDEs with varying ZHP concentrations in the CL; GDE-1 (30% ZHP/PTFE), GDE-3 (20% ZHP/PTFE), GDE-4 (40% ZHP/PTFE) and GDE-5 (50% ZHP/PTFE)	71
Figure 5.5: Performance curves for the MEAs prepared with 40% PTFE in the CL (GDE-1) and 40% PTFE and 30% ZHP in the CL (GDE-3).....	72
Figure 5.6: <i>In-situ</i> impedance curves of the MEAs for GDE-1 and GDE-3, at a cell voltage of +0.6 V	73
Figure 5.7: Performance curves for the MEAs with different ZHP content in the CLs	74
Figure 5.8: Current density at 600 mV versus the ZHP content in CL	75
Figure 5.9: Maximum Power density versus ZHP content in CL.....	77
Figure 5.10: <i>In-situ</i> impedance curves for MEAs with differing ZHP contents in CL, at a cell voltage of +0.6 V... ..	78
Figure 5.11: <i>Tafel plots</i> for the ORR of the GDEs with different catalyst layer compositions.....	79
Figure 5.12: Stability of GDE-1 and GDE-2 MEAs performance, operating for 500 h at 0.2 A cm ⁻²	79
Figure 5.13: SEM images of the cross-sections of the MEAs after the durability test: (a) GDE-1 MEA and (b) GDE-3 MEA.....	81

Figure 6.1: (a) Schematic diagram showing an expanded view of a MEA with acid-controlling regions and (b) GDE with <i>SiC</i> layer	84
Figure 6.2: HR-SEM surface images of (a, c) Freudenberg CX 196 GDL and (b, d) Freudenberg C4 GDL at 1,000x magnification and 50,000x magnification	85
Figure 6.3: Incremental intrusion pore-size distribution measurements of the GDLs ..	86
Figure 6.4: Incremental intrusion pore-size distribution measurements of the Freudenberg GDEs	87
Figure 6.5: Cross-sections of Freudenberg C4 GDEs with (a) 0.2 mg cm ⁻² <i>SiC</i> , (b) 0.5 mg cm ⁻² <i>SiC</i> and (c) 1 mg cm ⁻² <i>SiC</i> loading	87
Figure 6.6: Incremental intrusion pore-size distribution measurements of the Freudenberg C4 GDE and the Freudenberg C4 GDEs with varying <i>SiC</i> layer loadings	88
Figure 6.7: Surface micrographs of Freudenberg CX 196 GDEs with: (a-c) 0.2 mg cm ⁻² <i>SiC</i> -PTFE layer, (d-f) 0.2 mg cm ⁻² <i>NbC</i> -PTFE layer, (g-i) 0.2 mg cm ⁻² <i>SiC</i> -PBI layer and (j-l) <i>SiC</i> -30% <i>NbC</i> layer.	90
Figure 6.8: Incremental intrusion pore-size distribution measurements comparing the unmodified Freudenberg CX 196 GDE and the <i>SiC</i> -GDE.....	92
Figure 6.9: Cumulative intrusion pore-size distribution measurements comparing the unmodified Freudenberg CX 196 GDE and the <i>SiC</i> -GDE.....	93
Figure 6.10: Incremental intrusion pore-size distribution measurements for the <i>SiC</i> layers with different binders	94
Figure 6.11: Incremental intrusion pore-size distribution measurements comparing the unmodified Freudenberg CX 196 GDE, <i>SiC</i> -GDE and <i>NbC</i> -GDE.....	95

Figure 6.12: SEM cross-sectional images of (a) 0.2 mg cm ⁻² NbC GDE, (b) SiC-PBI GDE, (c) SiC/10 wt.% NbC GDE, (d) SiC/30 wt.% NbC GDE, (e) SiC/50 wt.% NbC GDE, (f) SiC/70 wt.% NbC GDE, (g) SiC/90 wt.% NbC GDE.....	96
Figure 6.13: Incremental intrusion pore-size distribution measurements comparing SiC-GDE, NbC-GDE and SiC/NbC-GDEs	97
Figure 6.14: Performance curves comparing MEAs of standard Freudenberg C4 GDE and Freudenberg C4 GDE modified with 0.2 mg cm ⁻² SiC layer doped with 4 mg cm ⁻² PA (anode and cathode).....	99
Figure 6.15: <i>In-situ</i> impedance curves illustrating the effect of SiC layer on cell resistances, at a cell voltage of +0.6 V.....	100
Figure 6.16: <i>Tafel plots</i> for the ORR of the GDEs with differing structures.....	100
Figure 6.17: Performance curves comparing Freudenberg C4 GDEs with various SiC layer contents and 4 mg cm ⁻² PA loading (anode and cathode).....	102
Figure 6.18: <i>In-situ</i> impedance curves comparing Freudenberg C4 GDEs with various SiC layer loadings, doped with 4 mg cm ⁻² PA, at a cell voltage of +0.6V.....	103
Figure 6.19: <i>Tafel plots</i> for the ORR of the GDEs with different SiC layer loadings.....	104
Figure 6.20: Performance curves comparing MEAs of Freudenberg C4 GDEs with 0.2 mg cm ⁻² SiC layer content and various PA doping levels (anode and cathode).....	104
Figure 6.21: <i>In-situ</i> impedance curves illustrating the effect of PA doping content on Freudenberg C4 GDEs with 0.2 mg cm ⁻² SiC layer, at a cell voltage of +0.6V.....	105
Figure 6.22: <i>Tafel plots</i> for the ORR of the Freudenberg C4 0.2 mg cm ⁻² GDEs with varying acid doping levels.....	105

Figure 6.23: Performance curves comparing MEAs of Freudenberg CX 196 GDE with Freudenberg CX 196 GDE with 0.2 mg cm ⁻² SiC layer doped with 2 mg cm ⁻² PA (anode and cathode).....	107
Figure 6.24: In-situ impedance curves comparing MEA of a standard Freudenberg CX 196 GDE versus MEA of Freudenberg CX 196 GDE with 0.2 mg cm ⁻² SiC and 40% PTFE layer, doped with 2 mg cm ⁻² PA (anode and cathode), at a cell voltage of +0.6 V	108
Figure 6.25: Tafel plots for the ORR of the Freudenberg CX 196 GDEs with different GDE structures.....	110
Figure 6.26: Performance curves for MEAs comparing Freudenberg CX 196 GDEs with 0.2 mg cm ⁻² SiC layer content and various PA doping levels (anode and cathode).....	111
Figure 6.27: In-situ impedance curves for MEAs comprised of Freudenberg CX 196 GDEs with 0.2 mg cm ⁻² SiC and 40% PTFE layer, with various PA doping levels (anode and cathode), at a cell voltage of + 0.6 V.....	112
Figure 6.24: Performance curves for MEAs comparing Freudenberg CX 196 GDEs with 0.2 mg cm ⁻² SiC layer content and various binders in the SiC layer and 2 mg cm ⁻² PA doping (anode and cathode).....	108
Figure 6.25: In-situ impedance curves for MEAs comprised of Freudenberg CX 196 GDEs with 0.2 mg cm ⁻² SiC and various polymers, with 2 mg cm ⁻² PA doping (anode and cathode), at a cell voltage of + 0.6 V.....	110
Figure 6.26: Performance curves comparing MEAs of Freudenberg CX 196 GDE with Freudenberg CX 196 GDE with 0.2 mg cm ⁻² NbC layer doped with 2 mg cm ⁻² PA (anode and cathode).....	111
Figure 6.27: In-situ impedance curves comparing MEAs of Freudenberg CX 196 GDE and Freudenberg CX 196 GDE with 0.2 mg cm ⁻² NbC and 40% PTFE layer, doped with 2 mg cm ⁻² PA (anode and cathode), at a cell voltage of +0.6 V.....	112
Figure 6.28: Tafel plots for the ORR of the Freudenberg CX 196 0.2 mg cm ⁻² SiC GDEs with different H ₃ PO ₄ loadings.....	113

Figure 6.29: Performance curves comparing MEAs of Freudenberg CX 196 GDE with various <i>SiC</i> , <i>NbC</i> and combinations of <i>SiC/NbC</i> layers doped with 2 mg cm ⁻² PA (anode and cathode).....	114
Figure 6.30: <i>In-situ</i> impedance curves for the various ceramic carbide layers, at a cell voltage of +0.6V.....	115
Figure 6.31: <i>Tafel plots</i> for the ORR of the Freudenberg CX 196 GDEs with different polymers in the <i>SiC</i> layer.....	116
Figure 6.32: Performance curves comparing MEAs of Freudenberg CX 196 GDE with Freudenberg CX 196 GDE with 0.2 mg cm ⁻² <i>NbC</i> layer doped with 2 mg cm ⁻² PA (anode and cathode).....	117
Figure 6.33: <i>In-situ</i> impedance curves comparing MEAs of Freudenberg CX 196 GDE and Freudenberg CX 196 GDE with 0.2 mg cm ⁻² <i>NbC</i> and 40% PTFE layer, doped with 2 mg cm ⁻² PA (anode and cathode), at a cell voltage of +0.6 V.....	118
Figure 6.34: <i>Tafel plots</i> for the ORR of the Freudenberg CX 196 GDEs with different structures.....	118
Figure 6.35: Performance curves comparing MEAs of Freudenberg CX 196 GDE with various <i>SiC</i> , <i>NbC</i> and combinations of <i>SiC/NbC</i> layers doped with 2 mg cm ⁻² PA (anode and cathode).....	119
Figure 6.36: <i>In-situ</i> impedance curves for the various ceramic carbide layers, at a cell voltage of +0.6V.....	121
Figure 6.37: <i>Tafel plots</i> for the ORR of the Freudenberg CX 196 GDEs with varying carbide layers.....	122
Figure 6.38: Stability of the standard MEA and the <i>SiC</i> MEA, operating for 500 h at 0.2 A cm ⁻²	124
Figure 6.39: SEM images of the cross-sections of the MEAs after the durability test: (a) Freudenberg CX 196 MEA and (b) <i>SiC</i> MEA.....	125

List of tables

Table 1: Fuel cell types and features	15
Table 2: Impedance and Tafel slope characteristics of the MEAs.....	62
Table 3: Specifications of the GDEs.....	67
Table 4: Elemental Analysis (all results in wt.%).....	68
Table 5: Resistances of single cells with various GDEs.....	76
Table 6: Impedance and <i>Tafel slope</i> characteristics of the various Freudenberg C4 <i>SiC</i> MEAs.....	98
Table 7: Impedance and <i>Tafel slope</i> characteristics of the standard MEA <i>vs</i> the <i>SiC</i> MEA.....	108
Table 8: Impedance and <i>Tafel slope</i> characteristics of the Freudenberg CX 196 MEAs with various PA doping levels.....	113
Table 9: Impedance and <i>Tafel slope</i> characteristics of the MEAs with different binders in <i>SiC</i> layer.....	115
Table 10: Impedance and <i>Tafel slope</i> characteristics of the Freudenberg CX 196 MEAs with <i>SiC</i> and/or <i>NbC</i> layers.....	120

List of abbreviations

PEMFC	Polymer Electrolyte Membrane Fuel Cell/Proton Exchange Membrane Fuel Cell
LT-PEMFC	Low Temperature Polymer Electrolyte Membrane Fuel Cell
HT-PEMFC	High Temperature Polymer Electrolyte Membrane Fuel cell
MEA	Membrane Electrode Assembly
GDE	Gas Diffusion Electrode
GDL	Gas Diffusion Layer
CL	Catalyst Layer
ABPBI	Poly(2,5-benzimidazole)
PBI	Polybenzimidazole
CNTs	Carbon nanotubes
PFSA	Perfluorosulfonic acid
PA	Phosphoric acid
CCS	Catalyst-coated substrate
CCM	Catalyst-coated membrane
EIS	Electrochemical Impedance Spectroscopy
TPB	Triple Phase Boundary
HOR	Hydrogen Oxidation Reaction
ORR	Oxygen Reduction Reaction
PEM	Polymer Electrolyte Membrane
AFC	Alkaline Fuel Cell
DMFC	Direct Methanol Fuel Cell
PAFC	Phosphoric Acid Fuel Cell
MCFC	Molten Carbonate Fuel Cell

SOFC	Solid Oxide Fuel Cell
MPL	Microporous Layer
HR-SEM	High resolution Scanning Electron Microscopy
EDS	Energy Dispersive X-ray Spectroscopy
MIP	Mercury Intrusion Porosity
UP	Ultra Pure
PA	Phosphoric Acid
EBSD	Electron Backscatter Diffraction
ZHP	Zirconium hydrogen phosphate
R & D	Research and development
slpm	standard litres per minute



List of symbols

E	Theoretical potential
ΔG	Gibbs free energy of change
W_{el}	Electrical energy
n	number of electrons transferred
F	Faraday constant
T	Temperature
R_{CT}	Charge Transfer Resistance
R_{Ω}	Ohmic Resistance



Table of contents

Contents

Declaration	ii
Acknowledgements	iii
Abstract	iv
List of figures	viii
List of tables	xv
List of abbreviations	xvi
List of symbols	xviii
Chapter 1: Introduction	1
1.1 Background.....	1
1.2 Rationale of the study.....	3
1.3 Research Objectives.....	7
Chapter 2: Literature Review	8
2.1 Fuel cell overview	8
2.1.1 Background.....	8
2.1.2 Principle of Operation.....	11
2.2 Classification of Fuel Cells	14
2.2.1 Alkaline Fuel Cell.....	16
2.2.2 Molten Carbonate Fuel Cell	16
2.2.3 Solid Oxide Fuel Cell.....	17
2.2.4 Phosphoric Acid Fuel Cell.....	19
2.2.5 Direct Methanol Fuel Cell	21
2.2.6 Polymer Electrolyte Membrane Fuel Cell.....	22
2.3 Low Temperature PEMFCs.....	23
2.3.1 Electrode Reactions	23

2.3.2 PEMFC Performance	26
2.3.3 Components.....	27
2.4 High Temperature PEMFCs.....	33
2.4.1 Advantages associated with high temperature operation.....	34
2.4.2 Disadvantages associated with high temperature operation.....	36
Chapter 3: Experimental Method	39
3.1 Materials	39
3.2 Deposition Method.....	40
3.3 Fabrication of CsHSO ₄ GDEs.....	40
3.3.1 Synthesis of CsHSO ₄	40
3.3.2 Preparation of CsHSO ₄ GDEs	41
3.4 Fabrication of ZHP GDEs	41
3.5. Fabrication of SiC and/-or NbC GDEs.....	42
3.5.1 Preparation of Standard GDE.....	42
3.5.1 Preparation of SiC and/-or NbC Layer.....	42
3.6 Physical Characterisation Techniques	43
3.6.1 Scanning Electron Microscopy and Energy Dispersive X-ray Spectroscopy	43
3.6.2. Fourier Transform Infrared Spectroscopy.....	44
3.6.3 Mercury Intrusion Porosimetry.....	44
3.7 Electrochemical Characterisation of the MEAs.....	45
3.7.1 MEA and Cell Assembly	45
3.7.2 Single cell performance evaluation.....	46
3.7.3 Electrochemical Impedance Spectroscopy.....	47
Chapter 4: Evaluation of CsHSO₄ as a proton conductor in the catalyst layer of HT-PEMFCs.....	48
4.1 Introduction.....	48
4.2 Results and discussion.....	51
4.2.1 Structural analysis	51
4.2.2 Electrochemical Analysis	56

4.3 Conclusions.....	65
Chapter 5: Evaluation of ZHP for improved proton conductivity in the catalyst layer	67
5.1 Introduction.....	67
5.2 Results and Discussion	68
5.2.1 Influence of ZHP on the catalyst layer structure	68
5.2.2 Single cell performance	72
5.2.3 Influence of ZHP content on MEA performance.....	75
5.2.4 Stability	80
5.3 Conclusions.....	83
Chapter 6: Development of ceramic carbide acid-controlling region	84
6.1 Introduction.....	84
6.2. Results and discussion.....	86
6.2.1. Structural Evaluation of GDEs.....	86
6.2.2 Electrochemical evaluation of MEAs.....	99
6.2.2.1 Effect of GDL on performance.....	99
6.2.2.2 Influence of SiC loading on performance of Freudenberg C4 GDEs	102
6.2.2.3 Single cell performance of Freudenberg CX 196 based MEAs.....	108
6.2.2.3 Influence of PBI in SiC layer	115
6.2.2.4 Influence of NbC layer	117
6.2.2.5 Effect of NbC addition to SiC layer	120
6.2.2.6 Stability	124
6.3 Conclusions.....	127
Chapter 7: Final conclusions, Recommendations, Future work and Outputs	128
7.1 Final conclusions.....	128
7.2 Recommendations and Future work.....	130
7.3 Outputs.....	130

7.3.1 Publications.....	130
7.3.2 Conferences	132
References	133



Chapter 1: Introduction

1.1 Background

Fuel cells are considered to be one of the most promising technologies for clean and efficient power generation in the present century, with polymer electrolyte membrane fuel cells (PEMFCs) being amongst the most actively studied fuel cells in recent years. The vast majority of research has been devoted into the research and development (R & D) of PEMFCs for transportation. In order to achieve the transport industries requirements, PEMFCs have to overcome some intrinsic challenges such as durability and cost of system components.

The main component of a PEMFC is the membrane electrode assembly (MEA), which is comprised of the polymer electrolyte membrane, gas diffusion layers (GDLs) and the catalyst layers. In order for the electrode reactions to occur, the catalyst needs to be at the boundaries of three phases, i.e. electron conductive phase (carbon), ion conductive phase (polymer electrolyte), and gas or liquid phase of reactants and products (pores) [1]. The point where the reactants, catalyst, and electrolyte come into contact is referred to as the 'triple-phase boundary' (TPB). This TPB area depends greatly on the method of MEA fabrication as well as structural parameters such as catalyst and ionomer loading [2]. The catalysts used to facilitate the electrode reactions which occur in the MEA are normally expensive platinum group metal catalysts. Research has focused on reducing costs by finding alternative catalysts as well as improving the efficiency of the catalyst utilisation.

Low temperature polymer electrolyte membrane fuel cells (LT-PEMFCs), utilising a solid polymer membrane as the electrolyte have been widely studied. The electrolyte membrane requires water to conduct protons and this limits the temperature range to

below 100 °C, which lowers the system efficiency. LT-PEMFCs are used as small-scale power sources in vehicles, portable and in residential use. Recent trends however are looking at the commercialization of 1kW-class domestic cogeneration systems using both electricity and electrically generated waste heat. Because higher temperatures result in a higher cell voltage, a stumbling block to the commercialisation of combined heat and power (CHP) systems is the inherent need to humidify LT-PEMFCs, as a result the R & D focus has shifted to high temperature polymer electrolyte membrane fuel cells (HT-PEMFCs) which do not require humidification and have improved operational efficiency [3]. **Fig. 1** illustrates a micro-CHP system in a household.

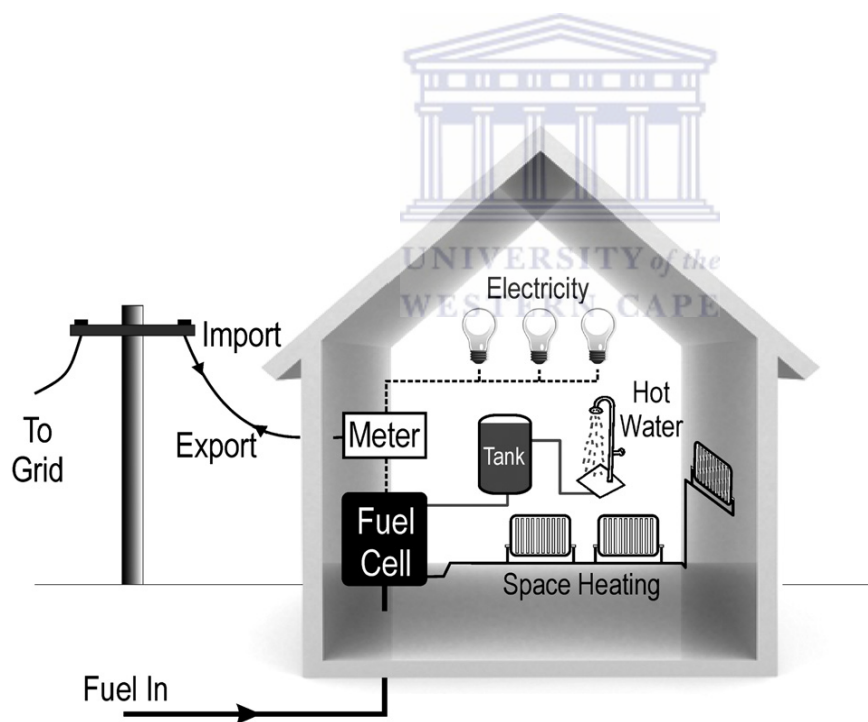


Fig. 1 Schematic of a Micro-CHP system in a household [4]

HT-PEMFCs have the advantage of having a high carbon monoxide (CO) tolerance (between 1 and 2%), which give them the ability to operate using reformat gas, whereas LT-PEMFCs require a CO content of 50ppm or lower. LT-PEMFCs can as a

result not utilise reformat fuel unless additional reactors are added to reduce *CO* content. A further advantage of HT-PEMFCs is the quality of heat which is made possible due to higher operating temperature. These enable the use of smaller and simpler fuel processing and ancillary systems, which aids in improving the overall efficiency of the fuel cell system [5].

1.2 Rationale of the study

Operation at elevated temperatures (120-200 °C) comes with its own set of challenges for HT-PEMFCs. HT-PEMFCs must have sufficient heat resistance under zero humidification conditions and should be based on polymer electrolyte membranes that can chemically couple with acids capable of proton conduction. Novel materials that provide high performance and high durability under such conditions are a prerequisite for HT-PEMFC. Acid-doped polybenzimidazole (PBI) membranes that are temperature resistant for operation above 100 °C have been developed and it has been reported that Pt nanocatalysts supported on multiwall carbon nanotubes (CNTs) showed a higher durability and stability (attributed to improved corrosion resistance and lower surface oxide formation) than that supported on carbon black [6]. Different techniques of gas diffusion electrode (GDE) fabrication have been developed based on perfluorosulfonic acid (PFSA) membranes for LT-PEMFCs, however, little effort has been made to fabricate gas diffusion electrodes for PBI-based membranes for HT-PEMFCs [7]. PBI is a basic polymer with good mechanical and chemical stability in the 120-200 °C temperature range, however, in order to be proton conducting the membrane has to be doped with an acid, typically phosphoric acid (PA). PA is a weak acid that supports conductivity in anhydrous conditions *via* the formation of a hydrogen-bonded network. PA is also utilised as an ionomer in the catalyst layers of

HT-PEMFCs based on PBI-membranes. This introduces a new set of problems as phosphate anions are strongly adsorbed onto the surface of Pt catalyst particles leading to catalyst deactivation and low performance [8, 9]. HT-PEMFCs are expected to have a performance three times greater than that of LT-PEMFCs due to improved reaction kinetics at higher temperature, but this has yet to be seen, with catalyst deactivation being one of the reasons for this lower performance. There is therefore an urgent need to find a more suitable ionomer material for the catalyst layer in PBI-based HT-PEMFCs.

Other challenges facing HT-PEMFCs include; the high corrosion rate of the amorphous carbon catalyst support, the dissolution and sintering of catalyst particles at high temperature and the accelerated degradation of the MEA due to the open circuit voltage in the zero-load state [10]. The proposed study aims to address the above issues by developing gas diffusion electrodes, by systematically introducing components, particularly various proton conductors, and optimizing the thickness, porosity and electrical conductivity, suitable for HT-PEMFC operation.

At the present time, there are only two modes for fabricating MEAs, in which the electrocatalyst can either be applied onto the GDL; called the catalyst-coated substrate (CCS) method, or directly onto an electrolyte membrane; called catalyst-coated membrane (CCM) method [11, 12]. Tang et al. [13] performed a comparative investigation on PEM fuel cells with MEAs made in the conventional manner (CCS MEAs) and CCM MEAs. Their findings showed that cells with a CCM MEA exhibit significantly higher performance than those prepared with conventional CCS MEAs. Although CCM MEAs exhibit improved performance over CCS MEAs, it is quite challenging to make the CCM for HT-PEMFCs. In the CCS method the substrate,

typically carbon cloth/paper made up of a porous network of carbon fibres, is coated with a catalyst layer, followed with the attachment of the electrolyte membrane between two GDEs by hot-pressing to form the completed MEA structure [7]. The structural modification of the MEA will affect the mass transport of the reactant gas and water produced during the reaction. Ion and electron transfer is also affected by structure of the catalyst layer, and this in turn affects the overall cell performance [14]. ABPBI poly(2,5-benzimidazole) membranes can be produced at low cost, provide improved water and phosphoric acid uptakes as well as good mechanical strength, as compared to PBI [15]; these properties make it a good choice for use as the electrolyte membrane.

The development and optimisation of catalyst layers and electrolyte membrane receive the majority of attention in HT-PEMFC research, while the properties of the entire GDE are often overlooked when developing the MEA for any novel proton conducting material. GDEs serve a critical role in the MEA of HT-PEMFCs; they should be able to provide strength, transport electrons, and retain their mass transfer functions at elevated temperature [16]. They are responsible for the permeation of reactant gases from the flow fields to the catalyst layer, *via* through-plane and in-plane gas access and product permeation from the catalyst layer to the flow fields. In addition they have to exhibit good electronic conductivity and thermal stability. These properties depend on the pore size distribution, thickness, hydrophobic content and carbonization or graphitization conditions of the diffusion electrodes [17].

In fuel cell electrodes, mass transport of reactants and products to and from the reaction zones should not be rate limiting relative to the desired chemical reaction rates. Concentration gradients occur if the mass transport limiting, and this leads to

losses in cell voltage and efficiency. The gas diffusion backings are typically porous carbon cloth or carbon paper to ensure that mass transport is not rate limiting [18]. PEMFCs operating at temperatures $\leq 80^{\circ}\text{C}$ under atmospheric pressure usually involve two-phase mass transport as water is present in both the liquid and vapour states as reactant gases have to be humidified in order to maintain adequate membrane hydration. However, HT-PEMFCs operating at temperatures greater than 100°C and atmospheric pressure, only have a single water phase (water vapour), so transport of water in the MEA will be easier to balance but leaching of phosphoric acid from the membrane poses a new set of problems [6]. The cathode flooding problem in HT-PEMFCs is not as severe as in LT-PEMFC, and transport of the reactant gases to the electrode layers is expected to be enhanced. There is also a reduction in the quantity of liquid water, and this increases the exposed surface area of the electrocatalysts and improves the ability of the reactants to diffuse into the reaction layer [19]. The development of a materially compatible GDE for HT-PEMFCs which are durable under high operating temperatures is essential for completion of HT-PEMFC technology.

Optimisation of the GDE component of the MEA inevitably leads to optimisation of the entire MEA structure. MEA optimisation leads to improved performance of the fuel cell, and MEAs which are more durable as the structural components are specific and selective to HT-PEMFCs. An integral part of the optimisation process is to find a way to prevent the formation of excessive phosphoric acid in the catalyst layer, this would include finding a catalyst layer ionomer other than PA, and preventing the PA from the ABPBI membrane from leaching into the catalyst layer by adding an acid-controlling layer to the GDE structure. GDEs have to be developed for HT-PEMFCs which are capable of providing long-term durability and stability. For this reason

materials are chosen that are capable of withstanding high temperatures for a sustainable period of time.

1.3 Research Objectives

The main objective of this work will be to develop a unique GDE structure that is capable of providing improved performance and durability for HT-PEMFC MEAs.

Within the context of the main objective, the specific objectives of the study were:

- i. Demonstrate new materials capable of acting as a suitable catalyst layer ionomer and effectively improving proton transfer at the interface between the electrolyte membrane and electrode, ultimately increasing *Pt* utilisation and optimising the catalyst layer for HT-PEMFCs by:
 - Introducing various materials capable of proton conduction at high temperature into the catalyst layer of GDEs for MEAs.
 - Characterising the performance and stability of these MEAs.
- ii. Develop, demonstrate and characterise a novel MEA architecture which involves the introduction of an acid-controlling region for HT-PEMFC MEAs by:
 - Identifying suitable materials for the acid-controlling region.
 - Optimising the acid-controlling region.
 - Characterising the performance and stability of these MEAs

Chapter 2: Literature Review

The literature review gives a brief background pertaining to fuel cells, which includes but is not limited to; history, types, developments and identification of problems areas associated with various aspects of their application. The identification of the problem areas will form the basis for which the GDE structure will be modified for the purpose of enhanced performance and stability.

2.1 Fuel cell overview

2.1.1 Background

Fuel cells are electrochemical devices that are capable of directly converting chemical energy to electrical energy, with a concomitant production of water and heat as long as there is a constant supply of reactant gases. A schematic diagram of a typical PEM fuel cell is shown in **Fig.2.1**. Fuel cells are capable of providing high efficiencies and low emissions as well quiet operation [20]. The energy conversion takes place between two electrodes, an anode and a cathode, and in this respect a fuel cell is very similar to a battery. The major differences between fuel cell and batteries are related to energy storage and conversion, with a battery being a closed system with the anode and cathode being the charge transfer medium and the electrodes themselves taking an active part in the redox reaction as reactants. Fuel cells are, however, are open systems where the anode and cathode serve as charge transfer media, with the reactants taking part in the redox reaction delivered from outside the cell [21]. Typically, a fuel cell is composed of two electrodes, an anode and a cathode which is separated by an electrolyte. The fuel (usually hydrogen) is oxidised at the anode into protons and electrons, and oxygen (usually supplied from air) is reduced at the

cathode into oxygen molecules. A selectively permeable electrolyte membrane allows only positive ions to pass through from the anode to the cathode, while acting as an insulator for electrons.

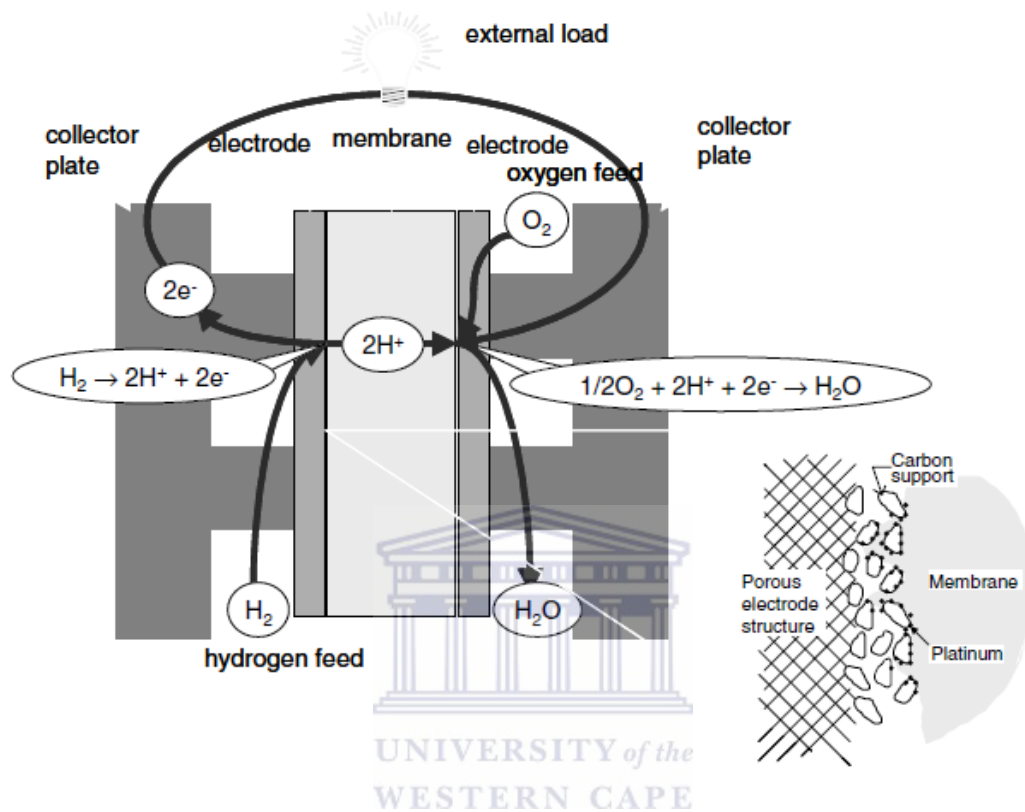


Fig. 2.1 Schematic diagram showing the basic principles of fuel cell operation [22].

In order for the system to become stable the electrons have to recombine with oxygen molecules and the positively charged ions, so they travel through an external circuit where they can power a given load before they reach the cathode where this reaction takes place [23]. The individual electrode chemical reactions involved and the overall chemical reaction taking place in a fuel cell are given as:

Anode reaction:



Cathode reaction:



Overall reaction:



Although fuel cell technology has gained a new surge in interest over the past three decades, fuel cell technology is not a recent invention; in fact the first fuel cell was invented in 1842 by Sir William Grove. This fuel cell which produced electricity by combining hydrogen and oxygen consisted of two electrodes submerged in sulphuric acid solution [24, 25]. Over the next 100 years fuel cell technology suffered with the emergence of internal combustion engines (ICE), with no real advances being made, until the technology once again experienced a surge of interest in the late 1950s. Scientists William Thomas Grubb and Leonard Niedrach at General Electric (GE) at this time worked on developing fuel cells for generating electricity for the spacecraft, leading to the eventual development of the first Proton Exchange Membrane Fuel Cell (PEMFC) [26]. The National Aeronautics and Space Administration (NASA) at this time realised the incredible advantages this technology posed and used a 12 kW Alkaline fuel cell in the Apollo and Gemini space programs [23], suffice it to say the technology really took off at this time with further development occurring in stationary and portable power applications.

The increasing global demand for energy, rising cost of fossil fuels, energy security and the increased environmental degradation the earth faces due to ever-increasing industrialisation as the worlds' population grows has led to heightened interest in high energy density power sources such as fuel cells [27-30]. Certain types of fuel cells such as PEMFCs, have already been successfully commercialised in specific fields

such a portable electronics and as back-up power supplies. Fuel cells can operate with very high electrical efficiencies of up to 70% or efficiencies of up to 90% if waste heat is captured and reused [21]. ICEs on the other hand are only capable of achieving efficiencies of 15-20%, the remainder of the energy contained in the fuel is lost on friction, incomplete burning of the fuel, and other inherent inefficiencies characteristic of ICEs. Fuel cells are capable of achieving higher efficiencies than ICEs, because unlike ICEs, fuel cells are not limited by the Carnot efficiency, but they do have a theoretical limit to their efficiency.

2.1.2 Principle of Operation

The energy driving the transfer of electrons in an electrochemical cell is called the Gibbs free energy (G), and since fuel cells are electrochemical cells the energy driving the electrochemical reaction is the same. The maximum amount of electrical energy (W_{el}) generated by the fuel cell corresponds to the change in Gibbs free energy, ΔG of the overall chemical reaction given in **Eq. 2.3** by:

$$W_{el} = -\Delta G = -nFE \quad (2.4)$$

In the absence of any voltage losses which occurs when no current is flowing, and n electrons are transferred, the change in Gibbs free energy produced by the electrochemical reaction is related to the theoretical potential of the fuel cell E , by the following reaction:

$$E = \frac{-\Delta G}{nF}$$

(2.5)

Where F is Faraday's constant (96.485 Coulombs/electron-mol), and since n , F and ΔG are all known, the theoretical potential of the H_2/O_2 fuel cell under ideal conditions can be calculated according to the following:

$$E = -\frac{\Delta G}{nF} = \frac{237.340 \text{ kJ mol}^{-1}}{2 * 96.485 \text{ C mol}^{-1}} = 1.23 \text{ V}$$

(2.6)

The theoretical potential value of 1.23 V is obtained at standard conditions, i.e., at a temperature of 25 °C and at atmospheric pressure and when the water product is in the liquid phase. The value of Gibbs free energy is however, not constant and varies with temperature, pressure and purity of reactants. At a higher temperature of say for instance, 200 °C the water product is in the gaseous phase and the value for ΔG is reduced to -220.40 kJ mol⁻¹, the theoretical potential of the H_2/O_2 fuel cell decreases to 1.14 V [31, 32]. The fuel cell output voltage of ~1.2 V is very small, so for most practical fuel cell applications, the unit cells have to be arranged into a cell stack to achieve the voltage and power output level required for the application [33]. **Eq. 2.6** above gives the no-loss open circuit voltage (OCV) of a fuel cell, when no current is drawn from the system. Electrical energy from the fuel cell is however, only obtained when a current is drawn, but simultaneous drops in the cell voltage occur due to various irreversible loss mechanisms. Even the OCV suffers from inherent losses, which can be attributed to gas leaks across the membrane due to poor sealing or

cracks in the membrane or to partial electronic conductivity, hence the actual OCV of a fuel cell is usually less than 1.23 V [20, 23, 31]. These voltage losses are commonly referred to as overpotential η , overvoltage or polarisation, which is defined as the deviation of the actual cell potential from the theoretical potential [34]. Besides the voltage losses occurring at OCV attributed to crossover of reactants and electronic conductivity of the membrane, there are three main contributions to voltage loss that increases with current; activation overpotential, ohmic overpotential and mass transport (concentration) overpotential.

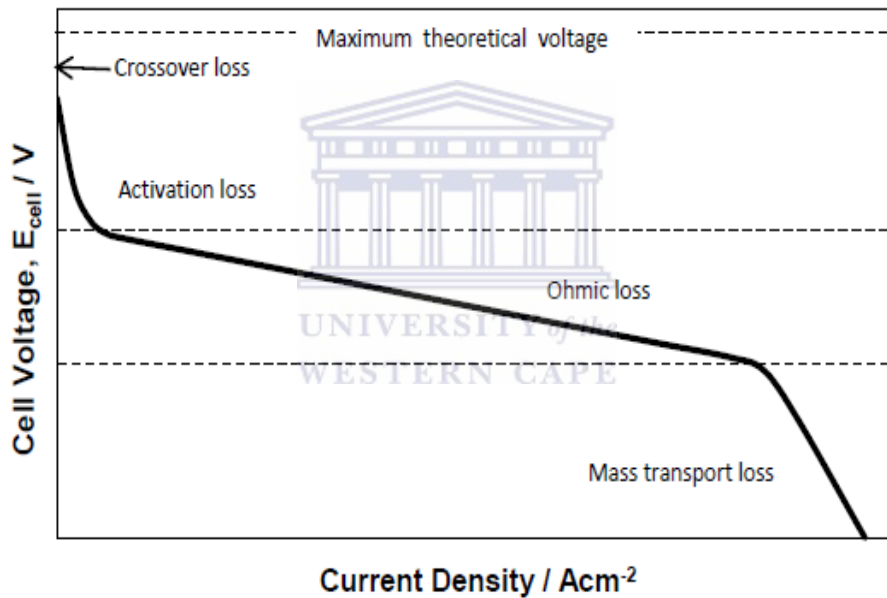


Fig. 2.2 Characteristics of a typical polarisation curve [35].

Fig. 2.2 shows a typical fuel cell polarisation curve illustrating the performance losses in the cell [35]. A polarisation curve is one of the main diagnostic methods for characterising a fuel cell and its performance. The performance characteristics are influenced by various factors such as catalyst loading, catalyst layer structure, electrolyte properties, flow field design, operating conditions and uniformity of local conditions over the entire active area of the electrode [32]. The shape of the curve is

the result of the four major irreversible voltage losses. The first overpotential arises due to reactant crossover and internal stray currents. At low current densities there is an initial rapid fall in voltage caused by activation losses, which is associated with sluggish electrode kinetics. The overpotential at medium current density results in a fairly linear region and is attributed to ohmic losses, which occur due to the resistance of the electrolyte to the flow of ions and the resistance of the electrode material and various cell components to the flow of electrons, as well as contact resistances. This voltage drop is directly proportional to current density and results in the linear shape of the curve. The final overpotential associated with the high current density region is caused by mass transport losses, due to the change in concentration of reactants at the surface of the electrodes resulting from the continuous consumption of the reactants in the electrochemical reaction. This mass transport loss is the result of a failure to transport sufficient reactant to the electrode surface, and as a consequence a concentration gradient is established [22, 33, 35]. The performance of a fuel cell is improved by thermodynamics and electrical efficiency of the system. Where the thermodynamic efficiency depends on fuel processing, water management and temperature control of the system, the electrical efficiency depends on the various overpotentials over the fuel cells like activation, ohmic and mass transport losses [23].

2.2 Classification of Fuel Cells

Fuel cells are typically classified according to the choice of electrolyte and the type of fuel it employs. Because ion conduction is a thermally activated process, the choice of electrolyte, which may be either liquid or solid determines the operating temperature range of the fuel cell as well as the type of ions which may be carried across the

electrolyte [20]. The operating temperature and lifetime of a fuel cell dictates not only the physicochemical properties, but also the thermomechanical properties of the materials used in the cell components (i.e. electrodes, electrolyte, interconnect, current collectors, etc.) [33]. There are at present six major different types of fuel cells: (i) PEMFC, (ii) alkaline fuel cell (AFC), (iii) solid oxide fuel cell (SOFC), (iv) molten carbonate fuel cell (MCFC), (v) phosphoric acid fuel cell (PAFC) and (vi) direct methanol fuel cell (DMFC). Fuel cells are further classified based on their operation temperature. PEMFCs, DMFCs, AFCs and PAFCs typically operate at low temperature (50-250 °C), whereas SOFCs and MCFCs operate at higher temperatures (650-1000 °C) [23]. **Table 1** depicts the different fuel cell types and their characteristic features.

Table 1: Fuel cell types and features

Fuel Cell Type	Fuel	Electrolyte	Mobile ion	Electrical Efficiency	Operating Temperature
PEMFC	H_2	Solid polymer membrane (Nafion)	$(H_2O)_nH^+$	~58%	<100 °C
AFC	H_2	Aqueous H_2	OH	~60%	150-200 °C
PAFC	H_2	H_3PO_4	H^+	>40%	150-200 °C
MCFC	Hydrocarbons, CO	$(Na,K)_2CO_3$	CO_3^{2-}	45-47%	600-700 °C
SOFC	Hydrocarbons, CO	$(Zr,Y)O_{2-\delta}$	O^{2-}	35-43%	700-1000 °C
DMFC	CH_3OH	Solid polymer membrane (Nafion)	H^+	35-40%	<100 °C

2.2.1 Alkaline Fuel Cell

The alkaline fuel cell, developed by Sir Francis Bacon in the 1930s is one of the most developed fuel cell technologies. It utilises a circulating liquid alkaline electrolyte, potassium hydroxide (KOH) which also acts as an effective heat transfer and water management medium [36]. The hydrogen and oxygen kinetics are more facile in alkaline than acid electrolytes, hence resulting in higher cell voltages. These higher cell voltages are not only due to better kinetics but are also attributed to the fact that the ORR *via* the intermediate peroxide, HO_2^- in alkaline electrolytes is more facile. Non-noble metal catalysts, such as Raney nickel, can hence be used for the fuel cell electrode. The AFC requires pure H_2 and O_2 reactants due to its electrolytes' susceptibility to CO_2 , which contaminates the electrolyte by clogging its pores [21]. The CO_2 reacts with the KOH electrolyte to form potassium carbonate (K_2CO_3), effectively reducing the OH^- ion concentration, causing a decrease in the ionic conductivity of the electrolyte and increasing the viscosity of the electrolyte. Ultimately having a negative impact on electrode kinetics and diffusion properties [37]. Potential problems due to CO_2 contamination can be overcome by using a scrubber to remove CO_2 or by changing the electrolyte at regular service intervals [36].

2.2.2 Molten Carbonate Fuel Cell

Molten carbonate fuel cells allow for internal reforming due to their high operating temperature (600-700 °C), and can as a result use both H_2 and CO_2 as fuels. They are capable of achieving high total efficiencies of ~80% due to the use of the waste heat in CHP systems [38]. The ORR kinetics are greatly improved by these higher

temperatures thereby eliminating the need for high loadings of the precious metal catalysts [39]. The electrolyte is usually a mixture of binary alkali carbonates, such as *Li/Na* carbonate or *Li/K* carbonate which is retained in a ceramic matrix of *LiAlO₂*. At these high temperatures the alkali carbonates form a highly conductive molten salt, with the carbonate ions (CO_3^{2-}) providing the ion conduction [33]. Morita *et al.*[40] showed that *Li/Na* exhibits a higher conductivity than *Li/K*, *Li/Na/K* and *Na/K* carbonates at the same temperature. The high operating temperatures provide good reaction rates enabling the use of inexpensive nickel-based catalysts. Anodes of MCFCs are typically a mixture of *Ni/Al* or *Ni/Cr*, which are used as *Ni* isn't stable enough and creeps into the molten carbonate electrolyte melt, thereby reducing the active surface area. The cathodes are typically composed of *NiO*, which are active enough for the ORR at high temperature, although *NiO* dissolution is also a problem. Addition of small quantities of magnesium to the cathode and electrolyte improves the stability, however alternative doped lithium oxide materials such as *LiCoO₂* used in conjunction with *NiO* have vastly improved the stability [39]. Tanimoto *et al.*[41] showed that the addition of appropriate quantities of *CaCO₃* or *BaCO₃* to a *Li-Na* carbonate electrolyte significantly reduced the *NiO* solubility in the electrolyte ultimately resulting in a 15-20% improvement in lifetime compared to the undoped material. MCFCs unlike other fuel cells rely on the balance of capillary pressure within the pores of the electrodes to establish the interfacial electrolyte/electrode boundaries [42].

2.2.3 Solid Oxide Fuel Cell

Solid oxide fuel cells (SOFCs) operate at temperatures of 700-1000 °C and commonly use the solid non-porous metal oxide yttria-stabilised zirconia (YSZ) as the electrolyte

which conducts ions via the oxide (O^{2-}) ion [33, 43, 44]. SOFCs are more stable than MCFCs as they employ a solid metal oxide as their electrolyte and hence no leakage due to a liquid electrolyte can occur. Electrolyte management issues that arise with PAFCs and MCFCs do not occur and there is no need for precious metal electrocatalysts due to the high operating temperature. SOFCs, like MCFCs can utilise both H_2 and CO_2 as fuels [31]. Typical materials for the porous electrodes are lanthanum strontium manganites ($(LaSr)MnO_3$) for the cathodes and Ni -based cermet for the anode, with common interconnect materials composed of lanthanum calcium chromites [45]. The zirconia in the Ni -based cermet anodes inhibits the sintering of the metal particles and provides a thermal expansion coefficient comparable to that of the electrolyte. Although lanthanum strontium manganites are typically used for the cathode, other materials such as p-type conducting perovskite structures which exhibit mixed ionic and electronic conductivity are also attractive cathode materials [31, 45].

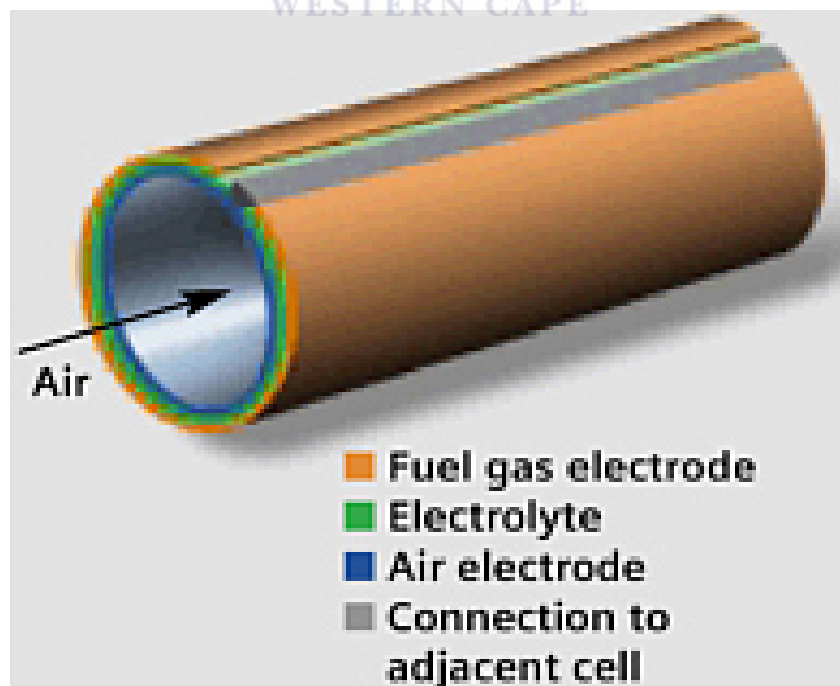


Fig. 2.3 SOFC tubular design developed by Siemens-Westinghouse [46].

Different SOFC designs have been developed over the years, with the tubular design shown in **Fig. 2.3** probably being the best known. The tubular design was developed by Westinghouse (now known as Siemens-Westinghouse) and has a self-sealing structure which improves thermal stability and eliminates the need for good thermal-resistant sealants. The tubular design has two system types, one where gas flows parallel to the tube axis and one where the gas flows perpendicular to the tube axis. Another common design is the planar configuration in which the single cell is configured as flat plates connected in series. The planar design is more efficient and cheaper than the tubular design path of the current is shorter and it is easier to stack than the tubular design, although sealing between the cells has proven to be difficult in the planar configuration [33, 39]. The main challenges facing SOFCs are associated with their high operation temperature. These high temperatures exclude the use of metals which are typically cheaper to produce than the ceramics, for any of the non-electrochemical components of the fuel cell and also increase the probability of cracks developing upon thermal cycling. Additionally, the components should exhibit thermo-mechanical compatibility; *i.e.* the thermal expansion coefficients must match, and the materials should have sufficient strength in order to withstand mechanical stresses due to differences in thermal expansion [20].

2.2.4 Phosphoric Acid Fuel Cell

The phosphoric acid fuel cell operates at temperatures of 175-180 °C and is based on 100% concentrated phosphoric acid electrolyte immobilised in a porous matrix. PAFCs are among the most advanced systems regarding commercial development, with their use mainly focussed on stationary power applications [39]. Operating temperature of a PAFC is a compromise between electrolyte conductivity which

increases with increasing temperature, and lifetime of the fuel cell which decreases with increasing temperature [47]. While the chemical reaction involved in PAFCs is the same as in PEMFCs if pure H_2 is used as the fuel, PAFCs unlike AFCs and PEMFCs are much less sensitive to impurities such as CO and S in the fuel [23]. Phosphoric acid is chosen as the electrolyte due to its excellent thermal, chemical and electrochemical stability in addition to being the only inorganic acid with a low enough volatility at temperatures above $150\text{ }^\circ\text{C}$ to be suitable for use as an electrolyte in fuel cells [47]. The use of concentrated phosphoric acid minimises the water vapour pressure allowing for easier water management in the cell [33]. The phosphoric acid electrolyte is retained in a 0.1-0.2 mm thick SiC matrix, whose ohmic resistance is controlled by the thickness of the matrix, hence a 0.1-0.2 mm thick SiC matrix has a fairly low ohmic resistance, but the mechanical properties of such a matrix is fairly limited [48]. Various methods have been employed to improve the SiC matrix characteristics in order to improve the cells performance, Song *et al.* [49] for instance found that by using a matrix with a mixture of fine and coarse SiC particles a thin matrix layer could be fabricated which decreased the cells ohmic resistance and increased the cells performance. Neergat *et al.* [50] produced a high performance PAFC by using Pt/Co as a cathode catalyst and employing an electrolyte matrix composed of a combination of $SiC/ZrSiO_4$. PAFCs use GDEs which typically employ platinum or platinum alloys as anode and cathode electrocatalysts due to the slow ORR kinetics. The GDEs are comprised of a carbon backing substrate, coated with a microporous layer (MPL) and a lastly catalyst layer (CL) of Pt/C bonded with PTFE. The carbon has various functions; (i) it serves as a medium to disperse the Pt catalyst to ensure that a good utilisation of the Pt catalyst is achieved, (ii) to provide micropores in the GDE for maximum gas diffusion to the catalyst and electrode-

electrolyte interface and (iii) to effectively increase the electrical conductivity of the catalyst [31]. The use of carbon imposes certain limitations on the fuel cell; at potentials higher than +0.8 V carbon corrosion and *Pt* dissolution becomes an issue [47, 51].

2.2.5 Direct Methanol Fuel Cell

Direct methanol fuel cell uses methanol as the fuel and air as the oxidant, however, pure methanol cannot be used, but a mixture of methanol with water is required. The methanol fuel is fed directly to the anode without the intermediate step of reforming the methanol into H_2 . In order for the energy density of the fuel to be maintained, the original fuel feed must be pure methanol, and the water should be stored in the fuel cell system, with the methanol added to this water [39, 48]. Methanol is a liquid under DMFC operating conditions, hence it has a high energy density and can be produced from natural gas and renewable biomass resources. Although DMFCs commonly operate on liquid methanol/water mixtures, gaseous methanol/water mixtures can also be used [31, 39]. DMFCs have applications in the small portable power markets due to their low operating temperature, quick refueling and the capability of achieving longer lifetimes than batteries. They are capable of replacing batteries as methanol theoretically has superior specific energy densities in comparison to rechargeable batteries such as lithium-polymer and lithium-ion polymer systems [52]. Typically perfluorinated sulphonic acid ion exchange membranes developed by DuPont marketed as Nafion[®] are used as the electrolyte membrane in DMFCs. The acid polymer electrolyte relies on absorbed water to ionize acid groups and enable proton transport [53]. Although the majority of the methanol is oxidised to protons, electrons and CO_2 at the anode, some of the methanol is directly transported to the cathode through the membrane. This permeation of methanol from the anode to the cathode

via the membrane is termed methanol crossover, and it creates a mixed potential due to the methanol oxidation interfering with oxidation reduction reaction resulting in a decrease in the cathode potential. Not only does methanol crossover lead to mixed potentials, but it also lowers the efficiency since it wastes the fuel [39, 54].

Electrodes are porous gas diffusion media with noble metals such as *Pt/C* used as electrocatalysts. The methanol oxidation reaction (MOR) is sluggish compared to the hydrogen oxidation reaction (HOR), and it was found that alloying certain metals (*Re, Ru, Os, Rh, Mo, Pb, Bi, and Sn*) to *Pt* can enhance that activity of the binary electrocatalyst [39]. Zang *et al.*[55] prepared a *Pt* catalyst supported on core-shell structured *SiC@C* with a nanoscale *SiC* core covered by a graphitic carbon shell. The *Pt/SiC@C* electrocatalyst showed much higher activities for the methanol electro-oxidation and ORR than *Pt/SiC*, and more importantly showed greater stability in comparison to traditional *Pt/C*. They attributed the increased performance to the high dispersion of *Pt* on the *SiC@C* support and the high stability of the support in acid medium.

2.2.6 Polymer Electrolyte Membrane Fuel Cell

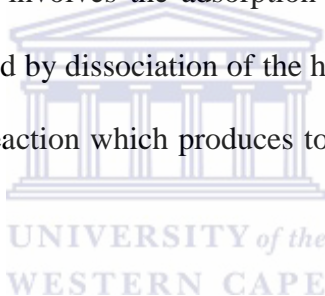
Polymer electrolyte membrane fuel cells (PEMFCs) are similar to DMFCs in that they both utilise a solid polymer, typically Nafion[®] as the electrolyte membrane. They are typically used in transport and stationary applications, and like DMFCs operate at fairly low temperatures of around 70-100 °C. The low operating temperature necessitates the need for sophisticated catalysts and electrodes to address the slow reaction kinetics [31]. At these low temperatures the fuel has to be relatively high purity *H₂* gas, due to the sensitivity of the *Pt* electrocatalyst to *CO* and *H₂S* in the feedstock, hence the fuel needs to undergo extensive fuel processing as the anode is

easily poisoned by even trace level of impurities [21, 33]. The proton conductivity of the Nafion[®] membrane introduces the inherent need for sufficient membrane hydration, the product water should not evaporate faster than it is produced in order to maintain sufficient membrane hydration [33]. A more in-depth discussion on PEMFCs follows, as PEMFCs are the fuel cell type on which this study is focussed.

2.3 Low Temperature PEMFCs

2.3.1 Electrode Reactions

Unlike the ORR, the hydrogen oxidation reaction (HOR) proceeds quite readily on *Pt*-based electrocatalysts. HOR involves the adsorption of H_2 onto the surface of the catalyst (see **Eq. 2.7**), followed by dissociation of the hydrogen gas molecule, and the proceeding electrochemical reaction which produces to hydrogen ions as seen in **Eq. 2.8**.



Where $Pt_{(s)}$ is an available surface site and $Pt-H_{ads}$ is an adsorbed H -atom on the active Pt active site [39]. The overall reaction for the HOR can be seen in **Eq. 2.1**.

Despite the use of *Pt*-based electrocatalysts the ORR has the slowest electrochemical kinetics and hence is the determining factor in the overall reaction rate [56]. Due to the high thermodynamic potential of the ORR (1.23 V vs NHE at standard conditions), no electrode materials can remain pure, hence at 1.23 V the electrode

materials undergo oxidation which changes the surface properties of the electrodes.

So at high potentials on *Pt* electrodes the following reaction occurs:



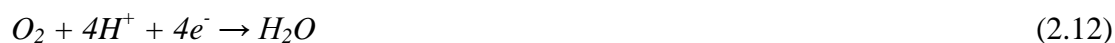
The *Pt* surface in the presence of O_2 is thus a mixture of *Pt* and *PtO*, hence a steady-state OCV of 1.23 V is almost never observed due to the formation of *PtO*. Thus in the fuel cell environment, a mixed value for the thermodynamic potential of O_2/H_2O and *Pt/PtO* can occur because two reactions occur: *Pt* oxidation and O_2 reduction [57].

In aqueous electrolytes the ORR can proceed *via* two mechanisms; an indirect 2-electron reduction pathway from O_2 to hydrogen peroxide (H_2O_2) (**Eq. 2.10** and **Eq. 2.11**), and a direct 4-electron reduction pathway from O_2 to H_2O (**Eq. 2.12**). The 4-electron pathway is preferred as the reaction has a greater Faradaic efficiency and it does not involve the peroxide species in solution.

2-electron reduction pathway:



4-electron reduction pathway:



Although the 4-electron pathway is preferred it involves a number of steps in which molecular oxygen has to be dissociated at the *Pt* surface and recombined with the hydrogen protons and electrons to form water [39]. Other factors such as geometry, crystal structure, d-band vacancy of the metal catalyst *etc.* can influence the kinetics of a reaction at a particular electrode. Kucernak *et al.* [58] study of the HOR and ORR under real fuel cell conditions noted that *Pt*-black shows higher specific catalytic activity towards the ORR than *Pt*-carbon at high potentials, this performance benefit was however reduced at lower potentials (see **Fig. 2.4**). This size effect does not however influence the HOR, as exchange current density values of 0.022 A cm^{-2} and 0.026 A cm^{-2} was observed for *Pt*-black and *Pt*-carbon respectively.

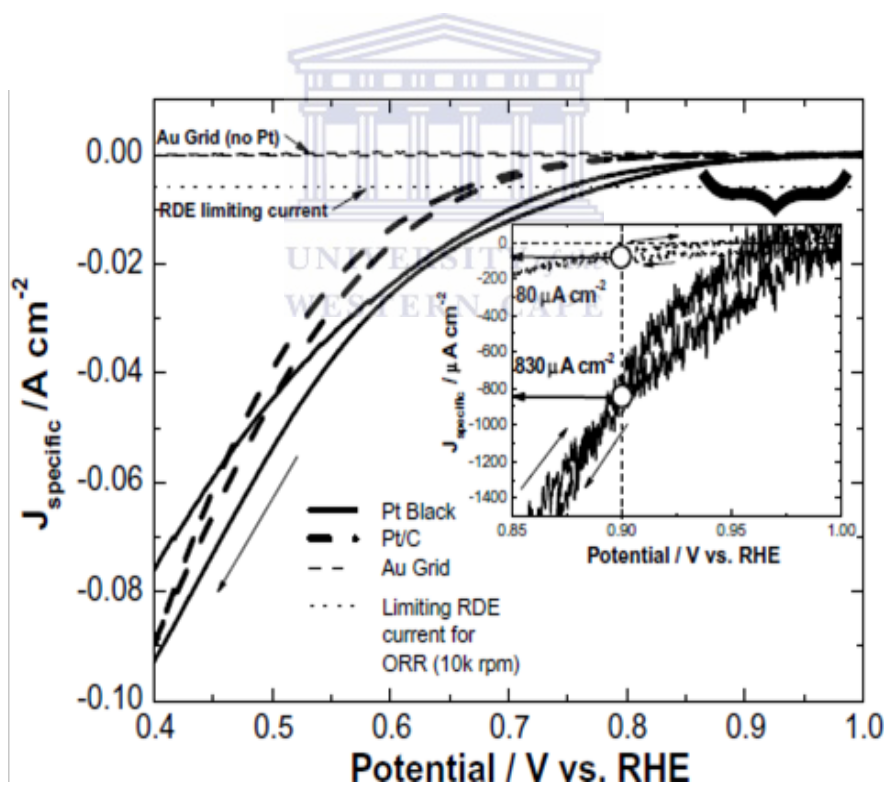


Fig. 2.4 Oxygen reduction at composite electrodes composed of Pt-Black (—) or Pt/Carbon (---) dispersed on an Au grid in contact with Nafion 117 membrane at a temperature of $50 \text{ }^\circ\text{C}$, 5 mV s^{-1} scan rate [58].

2.3.2 PEMFC Performance

The performance of a PEMFC in a kinetically controlled system can be represented by the *Tafel* equation:

$$E = E_{\text{rev}} + b \log i_0 - b \log i \quad (2.13)$$

$$b = -2.3 RT/\alpha nF \quad (2.14)$$

Where E , E_{rev} , b , i , i_0 , n and α are the electrode potential, reversible potential, *Tafel* slope, current density, exchange current density, the number of electrons transferred in the rate determining step and the transfer coefficient, respectively [59]. Since all the parameters in the *Tafel slope* are known, the parameters determining the *Tafel slope* are actually α and n . The higher the values for the *Tafel slope*, the faster the overpotential increases with current density. Hence, for an electrochemical reaction to achieve a high current at low overpotential, the reaction should have a low *Tafel slope* or a large αn . Two *Tafel slopes* are usually obtained for the ORR; 60 mV dec^{-1} and 120 mV dec^{-1} , respectively, depending on the materials used in the electrode and on the potential range.

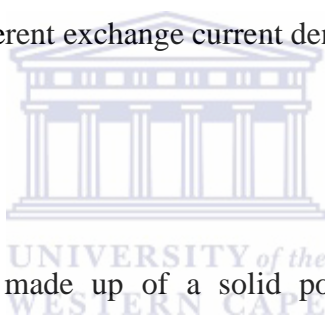
The electron transfer coefficient is a crucial factor in determining the *Tafel slope*. For ORR, the transfer coefficient is dependent on temperature. On a *Pt* electrode, the transfer coefficient of ORR is directly proportional to the temperature, in the range of 20–250 °C. Relative humidity (RH) has also been found to affect the transfer coefficient.

Exchange current density is an important kinetic parameter which represents the electrochemical reaction rate at equilibrium. For the electrochemical reaction:



both the forward and reverse reactions can occur. At equilibrium, the net current density of the reaction is zero. The current density of the forward reaction equals that of the reverse reaction. This current density, called the exchange current density determines how rapidly the electrochemical reaction can occur. The exchange current density of an electrochemical reaction depends not only on the reaction but also on the electrode surface on which the electrochemical reaction occurs.

For example, on a *Pt* electrode, the exchange current density of hydrogen oxidation is several orders larger than that of ORR. The O_2 reduction reaction shows a higher exchange current density on a *Pt* electrode than on an *Au* electrode. Electrode materials or catalysts therefore have a strong effect on the ORR kinetics, with different materials giving different exchange current densities [60].



2.3.3 Components

A typical PEMFC stack is made up of a solid polymer electrolyte membrane, electrically conductive GDE and bipolar plates [33].

Electrolyte membrane:

As discussed previously Nafion[®] is the most widely used membrane in PEMFCs, it is highly conductive due to its structural properties. The chemical structure of Nafion[®] is depicted in **Fig. 2.5**. PEMFCs based on Nafion[®] have typically been operated in a temperature range between 50 and 90 °C [33]. The upper limit of the temperature range is due to the difficulty in maintaining membrane water hydration at temperatures at or above 100 °C. Another important factor which influences the upper limit of the operational temperature is the glass transition temperature (T_g) of

Nafion[®], which is approximately 110 °C for the protonated polymer. Operation at temperatures above the T_g can lead to polymer chain rearrangement, which can ultimately cause structural changes in the membrane and lower the membrane, stability and lifetime [15].

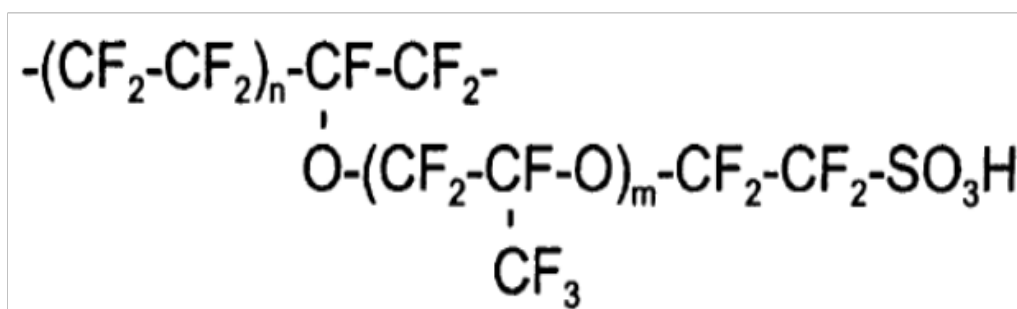


Fig. 2.5 Structure of Nafion[®] [61].

The extensive research performed on Nafion[®] over the past few decades has shown that the polymers' performance and intrinsic properties are dependent on not only its chemical identity (ion exchange capacity, anionic functional group and counter cation), but also on the polymer film method of synthesis (casting or melt-extrusion). Other factors such as the thermal history of the polymer (drying, exposure to high temperature and membrane pre-treatment) and chemical history of the membrane (exposure to various cations and solvents) also play a role in the polymers' performance and properties [62]. For instance, Hensley *et al.*[62] showed that after a short heat treatment of commercial Nafion[®] membranes at 165 °C, the proton conductivity, water permeability, equilibrium water sorption, and self-diffusion coefficient of water and protons increased in all films, with the greatest improvements exhibited by the thin films (<50 μm). Older hydrolysed N111-F is referred to as “HP” (hydrolysed precursor) and newer hydrolysed N111-F is called “HP NEW”. The

influence of annealing on proton conductivity and water sorption can be seen in **Fig. 2.6** and **Fig. 2.7**.

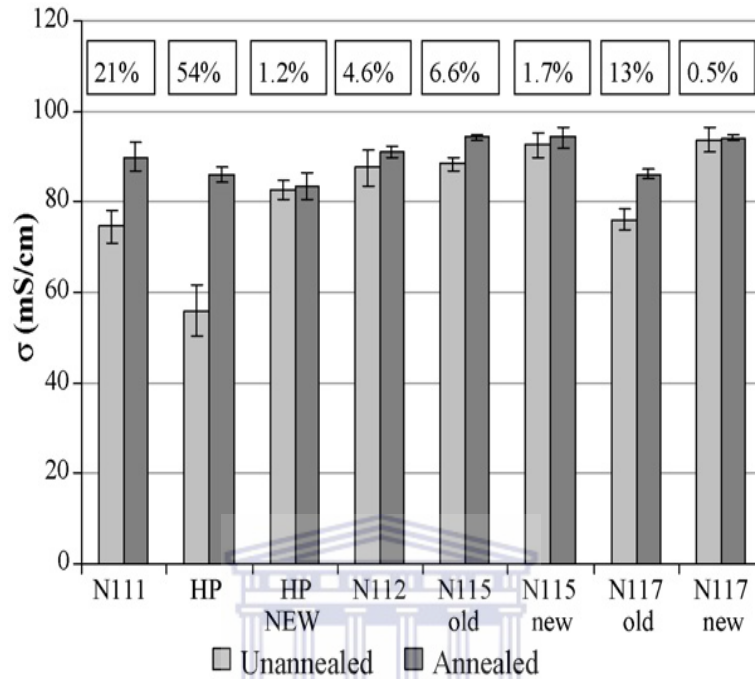


Fig. 2.6 Effect of annealing on proton conductivity [62].

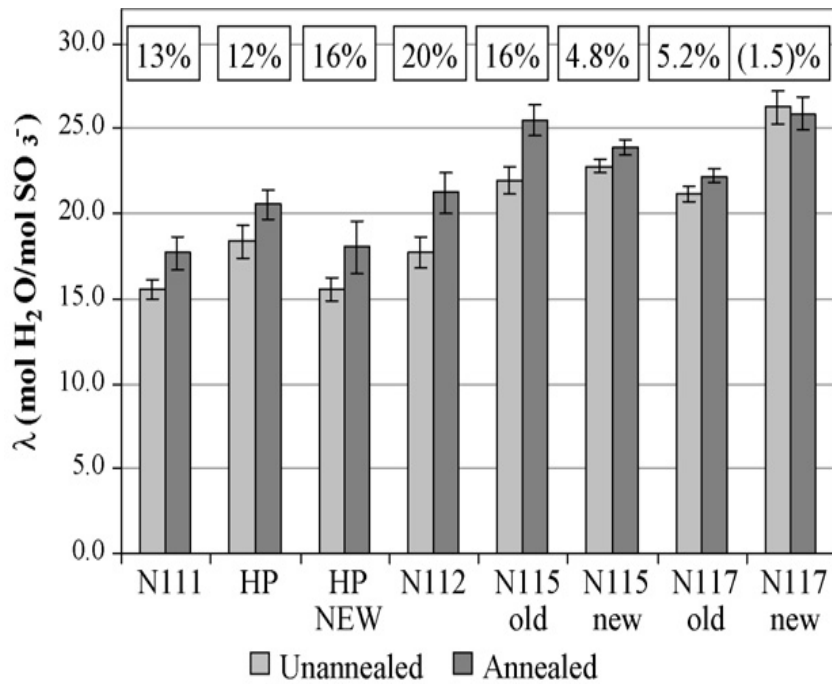
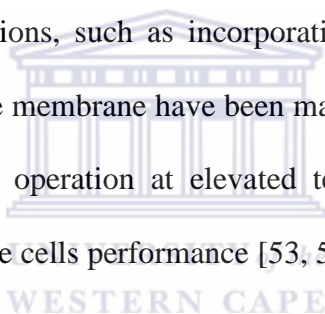


Fig. 2.7 Effect of annealing on water sorption [62].

Efforts to operate PEMFCs at higher temperatures for improved reaction kinetics and improved tolerance to impurities such as *CO* has led to the extensive research into the development of membranes that are capable of operating at higher temperatures and reduced humidity [61]. Since most solid polymer membranes rely on absorbed water to ionise the acid groups and permit proton transport, a dry membranes' conductivity is several orders of magnitude lower than that of a fully hydrated as the membrane proton conductivity is directly proportional with the water activity in the membrane. An increase in the fuel cell temperature raises the vapour pressure required to keep a given amount of water in the membrane, thus increasing the probability that membrane dehydration will occur and significantly reduce proton conductivity [53]. Various membrane modifications, such as incorporating inorganic materials (*TiO₂*, *ZrP*, *ZrO₂*, and *Al₂O₃*) into the membrane have been made to improve mechanical and electrical properties so that operation at elevated temperatures above 100 °C is possible without sacrificing the cells performance [53, 56, 63-65].



Gas diffusion electrodes:

The electrodes in PEMFCs are typically porous GDEs that have to ensure the supply of reactant gases to the active sites where the precious metal electrocatalyst is in contact with the ionic and electronic conductor [39]. The GDE is composed of the GDL and the electrode catalyst layer. A MPL is typically coated onto a porous conductive gas diffusion media (GDM), and together these two layers form the GDL. The GDM is typically carbon-based and commonly incorporates a hydrophobic material such as polytetrafluorethylene (PTFE), to prevent water from flooding the pores in the GDM and allow the reactant gases access to the catalyst sites. The GDM serves to (i) act as a gas diffuser, (ii) provide mechanical support, (iii) provide an

electrical pathway for the electrons and (iv) remove product water from the electrodes [33]. These properties are dependent on pore size distribution, thickness, hydrophobic content, and carbonisation or graphitisation conditions of the diffusion substrate [17]. Electrode catalyst layers are in close contact with the membrane and the GDL, and it is on the catalyst surface where the electrochemical reaction takes place. Although a large number of catalysts have been investigated, *Pt*-based catalysts are the superior catalysts for the ORR. In the manufacturing process the CL may be either directly deposited on the GDL or it can be deposited onto the membrane [33]. The GDE properties have a significant impact on the performance and durability of PEMFCs. For instance, Cindrella *et al.* [66] modified the GDL by depositing nanoscale inorganic metal oxides onto the surface of the GDL and observed that at low RH conditions (50% RH) certain modified GDLs exhibited improved performance to the pristine GDLs (see **Fig. 2.8**). Researchers' have also extensively studied the use of alternative catalyst supports, such as *TiO*₂, *WC*, *S-ZrO*₂, [67]

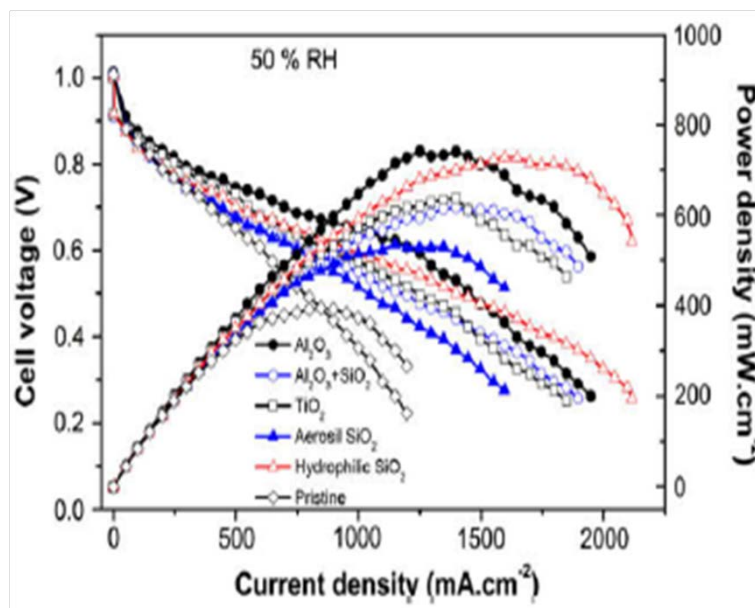


Fig. 2.8 Fuel Cell performance comparison of MEAs with pristine and nanoscale oxide coated GDL using *H*₂/*O*₂ at ambient pressure [66].

Bipolar plates:

As was previously discussed, the voltage that a fuel cell produces is quite small, so in order to meet the power requirements of the application, many cells have to be connected in series in order to increase the output voltage. This collection of cells in series is referred to as a 'stack'. An easy way to do this is to connect the edge of each anode to the cathode of the next cell, all along the line, although this method seems easy it would introduce more problems, as the electrons would have to travel across the face of the electrode to the current collection point at the edge. Although the electrodes are good conductors, even a tiny drop in voltage would be important as the voltage each cell generates is so small. This method is therefore not normally used, instead cells are interconnected by means of a bipolar plate. The bipolar plate makes connections across the entire surface of one cathode and the anode of the next cell [48]. In addition to carrying the electrical current away from each cell, they also distribute the reactant gases homogeneously to each individual cell and separate each individual cell to facilitate water management within the cell.

Non-porous graphite plates were first used due to their high electrical conductivity and their chemical stability in the fuel cell environment. Although graphite plates meet the aforementioned requirements, they are brittle and lack mechanical strength, with the added disadvantage of requiring the machining of the flow field channels, which adds to the total manufacturing cost. Composite graphite powders and polymer mixtures are alternatives to pure graphite plates [68]. Nikam *et al.* [69] demonstrated that corrugated metal sheets as bipolar plates could provide improved performance as seen in **Fig. 2.9** over conventional machined bipolar plates.

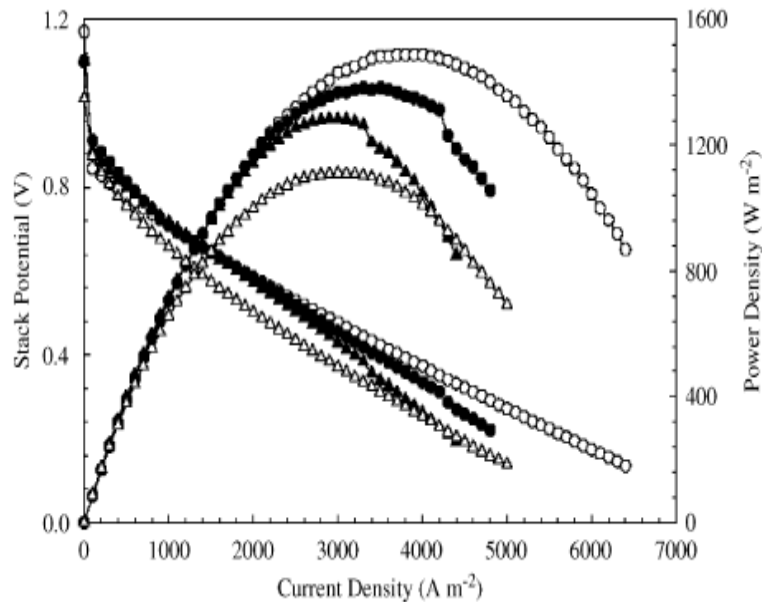


Fig. 2.9 Comparison of conventional machined channel flow fields and corrugated sheet flow fields: \circ , Corrugated sheet design with un-humidified fuel; \bullet , Corrugated sheet design with humidified fuel; Δ , Conventional parallel flow field design with un-humidified fuel; \blacktriangle , Conventional parallel flow field design with humidified fuel [69].

2.4 High Temperature PEMFCs

High temperature operation levels are more favourable for various applications, and considering the preceding discussion on LT-PEMFCs it becomes clear that a large majority of the issues we have with low temperature operation of PEMFCs could be solved by increasing the operation temperature. Increasing the operating temperature is however, not without its challenges. For instance, higher operating temperatures results in faster degradation processes, so one cannot simply use the same components one would use for low temperature operation; this introduces a whole new set of structural parameters that have to be considered.

2.4.1 Advantages associated with high temperature operation

PEMFCs function best when they use a high purity H_2 as the fuel source, but pure H_2 it is unlikely to be the fuel source due to economic considerations in production and storage. Instead hydrogen from reformed fuel, such as natural gas, gasoline or alcohol is more likely to be used in PEMFCs [70]. Reformate gas streams obtained from the after partial oxidation will contain ~3.0 vol. % of CO . This is normally reduced to less than 1 vol. % of CO by a water gas shift reaction. The CO tolerance of a HT-PEMFC using a high temperature membrane at its operation temperature is sufficiently high; hence, the PROX (preferential oxidation) reactor which preferentially oxidises CO over noble metal catalysts can be excluded. This is however, not the case with a LT-PEMFC using a low temperature membrane, leading to much higher capital costs [71].

In LT-PEMFCs the anode platinum catalyst is especially susceptible to small amounts of CO in the fuel; even these small amounts poison the catalyst and lead to lower cell performances. Li *et al.*[72] demonstrated the CO poisoning effect in Pt/C based electrocatalyst is temperature dependent, with a HT-PEMFC operating at a temperature of 200 °C able to tolerate 3% CO in the fuel whereas a LT-PEMFC operating at a temperature of 85 °C are only able to tolerate 1% CO in the fuel. This improved tolerance of HT-PEMFCs to CO was confirmed by Das *et al.* [73] who used Pt -alloys as the electrocatalyst. Their findings seen in **Fig. 2.10** showed that 2% CO and 5% CO can be tolerated equally at low current density ($<0.3 \text{ A cm}^{-2}$) at 180 °C without any cell performance loss.

Operating fuel cells at temperatures $>100\text{ }^{\circ}\text{C}$ allows for easier removal of waste heat due to the larger temperature difference between the fuel cell and the surrounding environment. This results in a much simpler cooling system, thus increasing the mass-specific and volume-specific power density of the fuel cell system [59]. Cho *et al.* [74] found that subjecting LT-PEMFCs to thermal cycling of the environment chamber from $80\text{ }^{\circ}\text{C}$ to $-10\text{ }^{\circ}\text{C}$ caused a degradation in performance due to the phase transformations and volume changes of water in the fuel cell. These volume changes of water can deform the catalyst layer, and lead to a reduction in the specific surface area resulting in decreased *Pt* utilisation. Since HT-PEMFCs are expected to contain minimal quantities of liquid water, hence subjecting them to sub-zero temperatures will have less of an impact, thus improving their stability and durability under these conditions [59].

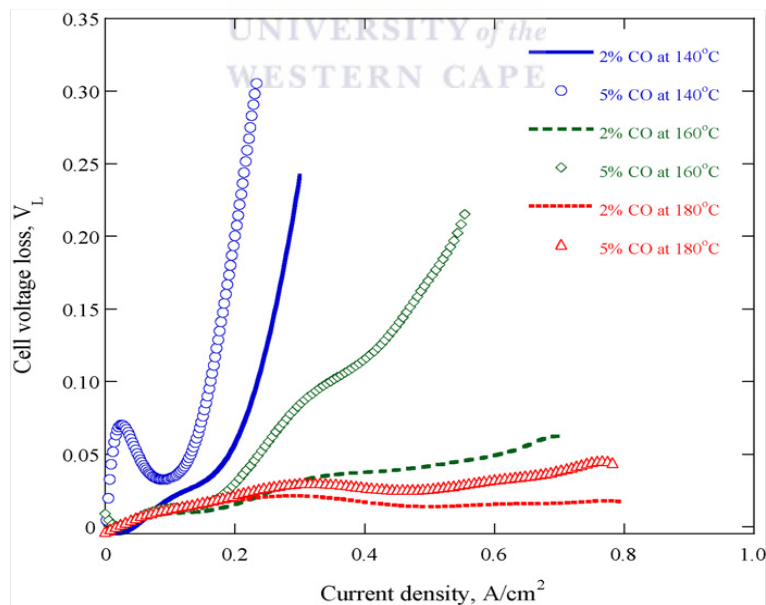
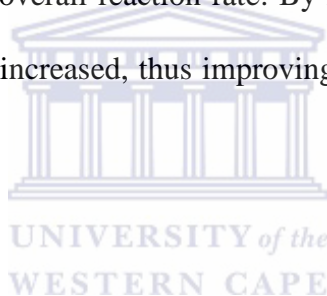


Fig. 2.10 Cell voltage loss, V_L , obtained experimentally with a PBI-based PEMFC with pure hydrogen and hydrogen containing different CO vol% at different temperatures [73].

HT-PEMFCs are preferred to LT-PEMFCs in micro-CHP systems, due to (i) the higher quality of waste heat generated and (ii) their improved CO tolerance, which would allow them to run on reformat fuel, as reformat fuel typically contain 3% CO in their fuel. Since the temperature of the exhaust stream for HT-PEMFCs ($>100\text{ }^{\circ}C$) is higher than that of LT-PEMFC ($<80\text{ }^{\circ}C$), the excess high quality waste heat generated in HT-PEMFCs is easier to transfer to the thermal circuit of the household and is available for hot water and space heating [4, 75].

The ORR in LT-PEMFCs is the major cause for the large overpotential at the cathode, and is thus responsible for the slow electrochemical kinetics; hence the ORR is the rate determining step for the overall reaction rate. By increasing the temperature the ORR kinetics is significantly increased, thus improving the performance of the MEA as a whole [56].



2.4.2 Disadvantages associated with high temperature operation

The main disadvantage associated with high temperature operation of PEMFCs is that the durability of the cell materials will become more severe as the operation temperature increases [6]. HT-PEMFCs based on PBI membranes are not dependent on humidification for membrane strength and conductivity. These membranes are however, dependent on PA doping for their ionic conductivity and membrane strength. The chemical structures for ABPBI and PBI membranes are depicted in **Fig.**

2.11.

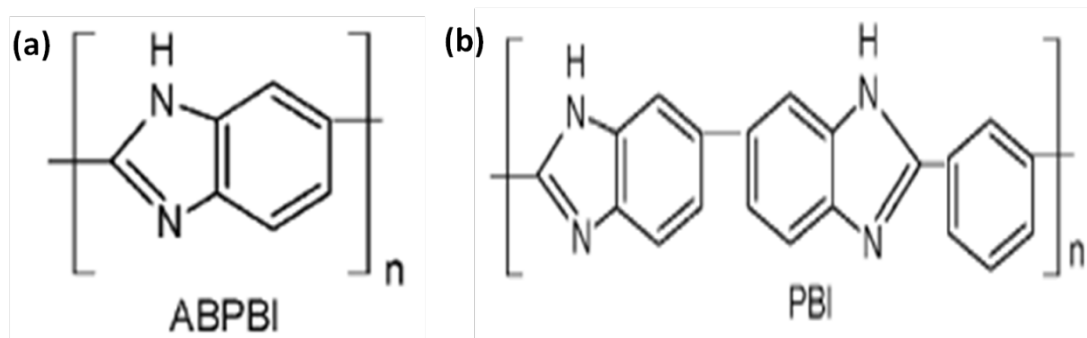


Fig. 2.11 Chemical structures of (a) Poly(2,5-benzimidazole) or ABPBI and (b) Poly(2,2'-*m*-(phenylene)-5,5'-bibenzimidazole) or PBI [76].

Raising the temperature improves the cell voltage but makes it difficult to maintain long-term durability [77]. Oono *et al.*[3] investigated the relation of PBI-based HT-PEMFCs operation temperature and cell durability in terms of deterioration mechanisms. They noted a reduction in cell voltage of ~20 mV during the long-term testing; this was considered to be caused both by agglomeration of the electrode catalyst particles in the early stages of operation, in addition to crossover effects caused by the loss of phosphoric acid in the terminal stage regardless of cell temperature. The relation between cell voltage, time and acid loss at different temperatures is shown in **Fig. 2.12**. The study performed by Oono *et al.* demonstrates that not only does high operation temperatures affect the durability and stability of cell components; but also that the degradation of components can occur simultaneously. The degradation of GDEs, which affects not only HT-PEMFCs, but LT-PEMFCs as well is an area of concern in fuel cell technology. The issue of chemical and morphological instability of the catalyst layer is however, cause for greater concern at elevated temperatures.

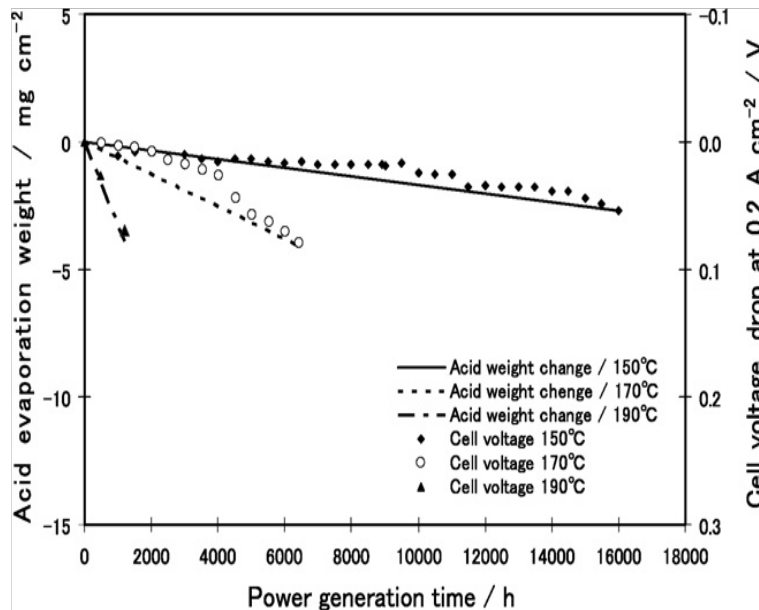


Fig. 2.12 Relationship between the acid weight change by evaporation and the cell voltage drop at different cell temperatures [3].

Corrosion of the carbon support may occur if the cathode is held at high oxidation potentials for too long, resulting in the generation of oxygen atoms at the catalyst. At elevated temperature, these may react with the carbon substrate and/or water to generate gaseous products such as CO and CO_2 . Over time the formation of these gaseous products leads to the destruction of the carbon support, leading to a reduction in carbon content within the catalyst layer. This reduction of carbon content reduces the surface available for the Pt catalyst, consequently forcing the Pt particles to aggregate effectively reducing the electrochemical active surface area of Pt [59, 78]. These factors clearly demonstrate the need for further R & D for HT-PEMFCs.

Chapter 3: Experimental Method

Chapter 3 serves as an introduction to the research design in terms of experimental approaches with regards to preparation and characterisation of all GDEs and MEAs of interest in this work. A detailed description which entails all sample preparation, characterisation, and data treatment will be discussed. The chapter will serve as an introduction for all materials used in this study, followed by a review of all characterisation methods, and a detailed description of all experimental parameters used in this study.

3.1 Materials

40 wt% *Pt/C*, HiSpec 4000 (Johnson Matthey, UK) was used as received as the catalyst material for both the anode and cathode catalyst layers prepared in all experiments. A 60 wt.% PTFE emulsion (Electrochem Inc, USA), 5 wt.% PVDF in DMAc solvent (Sigma Aldrich, USA) and a 5 wt.% PBI/DMAc (lab-made) were used as polymeric binders. All water used was obtained from a water purification system, Zeneer Power III (Human Corporation, SA). The UP water obtained had a conductivity of 18.3 MΩ. Isopropanol (Johnson Matthey, UK) or DMAc was used as the dispersing medium for all catalyst ink formulations. Commercially available GDLs, H2315 CX 196 and H2315 C4 (Freudenberg, Germany), was used as received. Fumapem[®] AM (Fumatech, Germany) ABPBI membrane with a thickness of ~35 μm was used as the electrolyte membrane. Membrane doping was achieved by immersing the membranes in 85% Phosphoric Acid at 95 °C for 24 h to obtain an acid doping level of about 3.8 molecules of H_3PO_4 per polymer repeating unit (PRU). Any superficial acid was gently removed by tissue prior to the MEA assembly. Cs_2SO_4 99.99% metals basis (Johnson Matthey, UK) and 98% H_2SO_4 (Kimix, SA) was used

to synthesise a 40 wt.% $CsHSO_4$ /aq. solution. Zirconium hydrogen phosphate, $Zr(HPO_4)_2$ (Sigma Aldrich, USA) was used as an additive in the CL. Silicon Carbide, SiC β -phase 99.8% metals basis (Johnson Matthey, UK) and Niobium Carbide, NbC 99% metals basis (Johnson Matthey, UK) were used to prepare the acid-controlling region on the surface of the CL.

3.2 Deposition Method

All GDEs analysed in this study were prepared via the manual spray technique. An airbrush (Prona RH-CP, Taiwan) using nitrogen carrier gas was used to manually spray all prepared GDEs. The Freudenberg GDLs were weighed before and after catalyst ink deposition to determine the catalyst loading. The dispersed catalyst ink was deposited in successive layers until the desired amount of catalyst had been deposited, with each layer being dried with a warm air dryer (Russell Hobbs, UK) before the next layer was added. The platinum loading of all anodes and cathodes prepared for this study was $\sim 1.0 \text{ mg cm}^{-2}$ Pt unless otherwise stated.

3.3 Fabrication of $CsHSO_4$ GDEs

3.3.1 Synthesis of $CsHSO_4$

$CsHSO_4$ was synthesised by dissolving 35.3 g of Cs_2SO_4 in 200ml ultrapure water. 21.7 g of H_2SO_4 was diluted in 50 ml ultrapure water. The diluted H_2SO_4 solution was slowly added drop-wise by a burette to the Cs_2SO_4 solution, while heating the Cs_2SO_4 solution to 60 °C and stirring at 250 rpm. The resultant crystals formed were dried overnight at 100 °C. Fourier transform infrared (FT-IR) spectroscopy was used to confirm the formation of $CsHSO_4$.

3.3.2 Preparation of CsHSO₄ GDEs

Catalyst ink formulations were obtained *via* ultrasonically (38 kHz) mixing *Pt/C*, UP water, IPA or DMAC solvent, *CsHSO₄* proton conductor and/or PTFE or PVDF binder in an ultrasonic bath (Grant Instruments, UK) for 2 hours before use. A ratio of 3:1 was utilised with respect to the *Pt/C*:UP water configuration in the catalyst ink mixture. The binder and *CsHSO₄* contents were normalized in relation to the *Pt/C* electrocatalyst, with 15 wt.% PVDF and 40 wt.% PTFE binder concentrations used in the catalyst ink formulations, with the *CsHSO₄* content varied. The catalyst ink was deposited onto the commercial GDL by the deposition method previously described. The binder content in the CL of these GDEs vary, with some values obtained from literature [5] or optimised by the authors. The GDEs were cured in a vacuum oven (Binder GmbH, Germany), with the GDEs containing only the polymer binders in the CL cured at 200 °C, and the GDEs containing the *CsHSO₄* proton conductor as well as the binder-*CsHSO₄* combinations cured at 120 °C.

3.4 Fabrication of ZHP GDEs

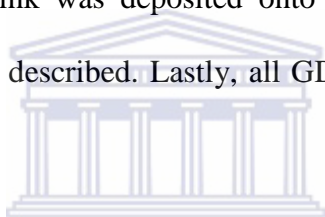
Catalyst ink formulations composed of *Pt/C*, UP water, ZHP and/or PTFE binder were obtained *via* ultrasonic (38 kHz) dispersion in IPA for 2 hours [79]. A ratio of 3:1 was utilised with respect to the *Pt/C*:UP water configuration in the catalyst ink mixture. The PTFE binder was normalised in relation to the *Pt/C* electrocatalyst, with 40 wt.% PTFE concentration used in all formulated inks, whereas the ZHP was normalised in relation to dry PTFE with varying concentrations used in the ink formulations. The catalyst ink was deposited onto the commercial GDL by the deposition method previously described. The PTFE binder loading in the CL was fixed at 40 wt.%, while the ZHP loading in the CL was varied from 20-50% in

relation to dry PTFE. Finally, all prepared GDEs were cured at 200 °C in a vacuum oven.

3.5. Fabrication of SiC and/-or NbC GDEs

3.5.1 Preparation of Standard GDE

Catalyst ink mixtures were obtained *via* ultrasonic (38 kHz) mixing of *Pt/C*, PTFE binder, UP water and IPA dispersion medium for 2 hours. A ratio of 3:1 was utilised with respect to the *Pt/C*:UP water configuration in the catalyst ink mixture. The PTFE binder content of 40 wt.% PTFE was normalised in relation to the *Pt/C* electrocatalyst. The catalyst ink was deposited onto the commercial GDL by the deposition method previously described. Lastly, all GDEs were cured at 200 °C in a vacuum oven.



3.5.1 Preparation of SiC and/-or NbC Layer

SiC and/-or *NbC* formulations were prepared by ultrasonic (38 kHz) mixing of *SiC* and/-or *NbC* powder, PTFE/ PBI binder, UP water and IPA for 1.5 hours. A ratio of 3:1 was utilised with regards to the *SiC/NbC*:UP water configuration in the ink mixtures. The PTFE binder content was normalised in relation to the *SiC* or *NbC* powder, with 40 wt.% PTFE used in all formulations. A PBI content of 10 wt.% PBI was used in relation to the *SiC* powder. The *SiC* and/-or *NbC* ink mixture was then deposited onto the standard GDE using the same deposition method as described for the catalyst ink mixtures. The GDEs containing solely *SiC* layers had variations of 0.2 mg cm⁻², 0.5 mg cm⁻² and 1 mg cm⁻² in the *SiC* content, whereas the GDEs containing solely a *NbC* layer had a fixed content of 0.2 mg cm⁻² *NbC*. The GDEs containing a mixture of *SiC/NbC* layer had a 0.2 mg cm⁻² fixed content of *SiC*, with the *NbC*

content normalised with regards to the *SiC*. The *NbC* content in these mixed GDEs were varied from 10-70% *NbC* in relation to the 0.2 mg cm^{-2} *SiC*. All GDEs prepared in this manner were then dried at $80 \text{ }^\circ\text{C}$ for 2 hours in a vacuum oven, followed by sintering at $350 \text{ }^\circ\text{C}$ under Nitrogen in a muffle furnace (Kiln Contracts, SA). The GDEs were then impregnated with predefined amounts of PA, by pipetting a mixture of PA and ethanol (1:6 ratio by volume) onto the surface of the GDEs followed by drying in a vacuum oven for a minimum of 72 hours to remove the ethanol and obtain an even PA distribution in the *SiC* and /-or *NbC* layer.

3.6 Physical Characterisation Techniques

3.6.1 Scanning Electron Microscopy and Energy Dispersive X-ray

Spectroscopy

A high-resolution Scanning Electron Microscope (SEM) (Nova NanoSEM 230, FEI) was used to observe the surface morphology and porous microstructure of the GDEs. The SEM micrographs are obtained by the interaction of an accelerated highly mono-energetic electron beam originating from the cathode filament, with the atoms of a sample surface. The beam is focused into a fine probe which is rastered over the surface of the sample, with the scattered electrons captured by the detector, modulated and amplified to produce an exact reconstruction of the sample surface and particle profile [80-82]. Energy dispersive X-ray Spectroscopy (EDS) was used to obtain elemental profiles of the ZHP-GDE. EDS is a trace analytical technique used to obtain surface chemical composition of materials. The technique includes both qualitative and quantitative analysis, as well as mapping the elemental distribution on the surface of the sample material. Advantages of using EDS in the quantitative analysis are that extremely small quantities of the elemental components can be detected, the technique

is precise and accurate and is primarily non-destructive when the electrostatic charging is not too severe. Measurements are performed based on the interactions between high-energy electrons and the sample surface. EDS measurements were conducted in conjunction with SEM, with the electron beam from the microscope used as the electron source for EDS [83].

3.6.2. Fourier Transform Infrared Spectroscopy

Fourier transform infrared (FT-IR) spectroscopy is a technique used to identify compounds. It is based on the principle that chemical bonds have specific frequencies at which they vibrate which correspond to natural energy levels. The technique results in changes in the vibrational energy of the molecule as a result of the absorption of electromagnetic radiation in the infrared region of the spectrum. Molecules resonate in the form of bending, stretching *etc.*, any absorbed energy would be utilised to change the energy levels associated with the resonance. A double beam spectrophotometer that comprises an IR sources produces a beam of light that is split into two beams that measures the samples' energy at different wavelengths. One beam passes through the sample while the other beam passes through the solvent. The beam is passed through a monochromator before being reflected back to the detector [84].

3.6.3 Mercury Intrusion Porosimetry

The pore-size distributions of the GDEs were determined by performing mercury intrusion porosimetry on the GDEs. Mercury intrusion porosimetry (MIP) obtains the pore-size distributions by injecting mercury into the samples at fixed pressures while recording the injected volume of mercury under quasi-steady conditions. The pressure and volume are related using various expressions for capillary pressure and radii as a means for determining the distribution of effective pore sizes. At high pressures the

mercury enters the small pores and at low pressures larger pores are sampled [85]. An Auto Pore IV 9500 (Micromeritics, USA) porosimeter shown in **Fig. 3(b)**, applying pressures between 0.0145 to 4136.85 bar, was used for porosity measurements.

3.7 Electrochemical Characterisation of the MEAs

3.7.1 MEA and Cell Assembly

The MEAs were obtained by sandwiching the acid-doped ABPBI membrane between the anode and cathode GDEs together inside a single cell fixture (Pragma Industries, France) without any prior hot-pressing procedure. PTFE tape was used to seal the MEA and act as a gasket. The single cell fixture shown in **Fig. 3(c)**, consists of two graphite plates with serpentine flow fields with an active area of 5 cm². A thermocouple and electrical heaters are embedded in the plates enable temperature control of the cell by a Cell Compression Unit (CCU, Pragma Industries, France). The cell fixture was placed in the CCU, which controlled the cell temperature at 160 °C and maintained the piston pressure of 2 N mm⁻² during operation.

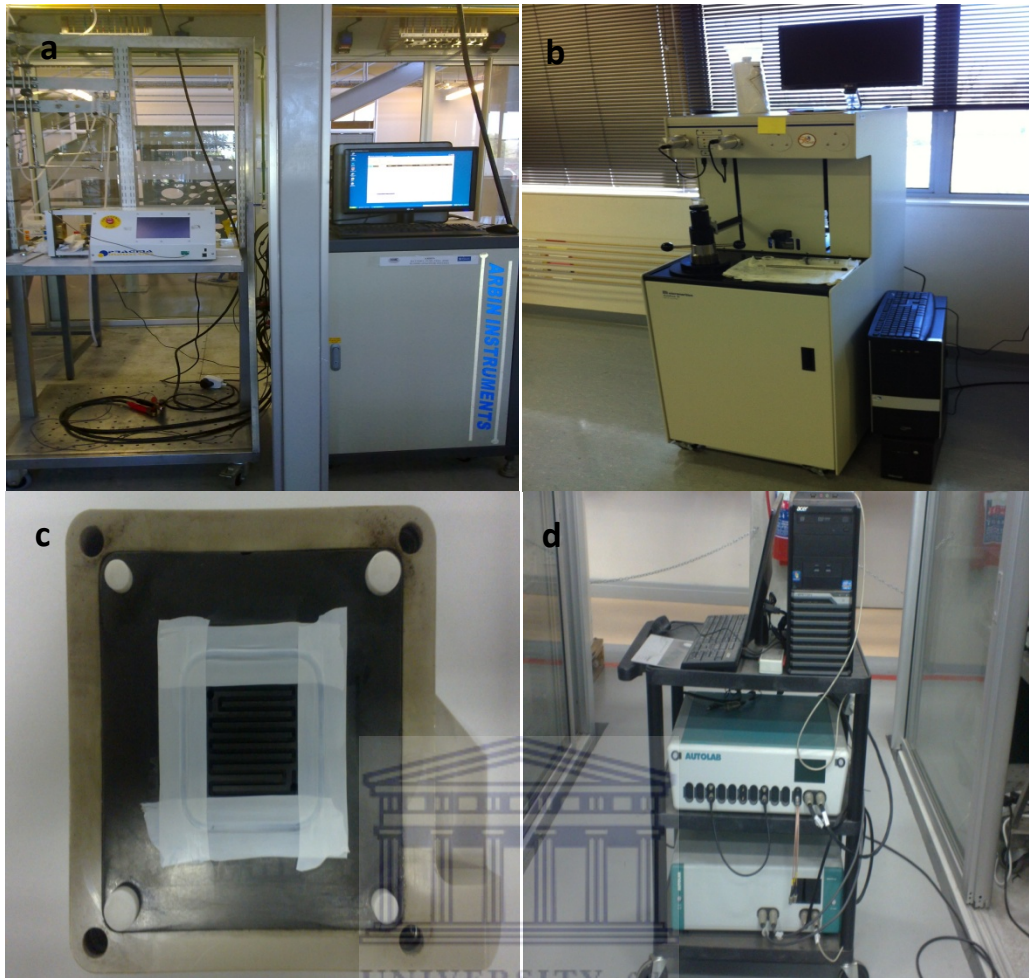


Fig. 3: Images of (a) *in-house* HT-PEMFC test bench (b) Autopore IV Mercury intrusion porosimeter (c) high temperature single cell (d) Impedance test station: Autolab PGSTAT302 testing station.

3.7.2 Single cell performance evaluation

An *in-house* HT-PEMFC test-stand shown in **Fig. 3(a)** was used to perform electrochemical evaluations on the MEAs. The test-stand consists of an electronic load, Arbin BT2000 (Arbin Instruments, USA) connected to a computer and a cell fixture in the CCU. Dry gases were used as the fuel and oxidant, with pure hydrogen fed to the anode and air was fed to the cathode with flow rates of 0.5 slpm and 1.0 slpm respectively. The MEAs were activated prior to testing, by applying a constant voltage of +0.55 V until a stable performance was achieved. The polarisation curves

were recorded by measuring the cell voltage as a function of current between Open Circuit Voltage (OCV) and +0.2 V. Stability analyses were performed at 1.0 A.

3.7.3 Electrochemical Impedance Spectroscopy

Electrochemical Impedance Spectroscopy (EIS) is an analytical technique used to measure the frequency dependence of the impedance of a fuel cell by applying a small perturbation signal (AC potential or current) of known amplitude and frequency to the fuel cell and measuring the current (or potential) response. EIS is a useful tool to distinguish individual contributions of each component, such as the electrolyte and gas diffusion electrode to the fuel cell performance, and is capable of identifying individual contributions to the total impedance of a fuel cell from different electrode processes [86]. A Potentiostat/Galvanostat Autolab PGSTAT 302N (Metrohm, Netherlands) equipped with a Frequency Response Analyser (FRA) and a 20 A current booster (Autolab BSTR 20A, Metrohm) shown in **Fig. 3(d)**, was used to perform Electrochemical Impedance Spectroscopy (EIS) measurements. The measurements were carried out at a cell voltage of +0.6 V, in the 0.1 Hz - 20 kHz frequency range with an amplitude of +0.01 V. Autolab Nova software was used to generate and simulate the impedance data.

Chapter 4: Evaluation of CsHSO₄ as a proton conductor in the catalyst layer of HT-PEMFCs

4.1 Introduction

Higher operational temperatures are expected to result in higher fuel cell performances [87]. HT-PEMFC operation requires novel/modified materials capable of withstanding these higher temperatures. For instance, acid doped polybenzimidazole (PBI) membranes that are temperature resistant for operation above 100 °C were investigated by Savinell *et al.* [88] for their possible use in PEMFCs, these membranes were shown to exhibit good proton conductivity, good mechanical and thermal stability as well as having a low reactant gas permeability. Weng *et al.* [89] showed that PBI has a distinct advantage over Nafion[®]/H₃PO₄ composite electrolytes in that PBI was shown to have an electro-osmotic drag coefficient of nearly zero for temperatures up to 200 °C, whereas the Nafion[®] composite electrolyte was shown to have an electro-osmotic drag coefficient in the range of 0.2-0.6. This essentially means that when protons are transported through PBI electrolyte they do not 'drag' water molecules with them, thus ensuring membrane hydration and preventing anode dehydration even at high operating temperatures. The PA used to dope these PBI membranes are often utilised as ionomers in the catalyst layer (CL) of PBI-based HT-PEMFCs [5, 90, 91]. More recently, PA doped poly(2,5-benzimidazole) (ABPBI) has been shown to have improved proton conductivity over PA doped PBI, as well as being cheaper to produce since it can be produced from a single commercially available monomer (3,4-diaminobenzoic acid (DABA)) by condensation in polyphosphoric acid (PPA) [92-94]. Theoretically HT-PEMFCs are expected to have improved performance over LT-

PEMFCs due to faster reaction kinetics achieved at higher operating temperature, however, this has yet to be achieved mainly due to catalyst deactivation by strong phosphate anion adsorption from the phosphoric acid ionomer onto the platinum (Pt) electrocatalyst, as well as other factors such as; the low solubility and diffusivity of oxygen in phosphoric acid [95], catalyst agglomeration and electrochemical carbon corrosion also contribute to the cell performance loss [78, 96].

The above mentioned factors show that there is still a clear need to improve MEA of HT-PEMFCs. On the membrane aspect, researchers' efforts have focused on improving the conductivity of the membrane, membrane strength [97-104], and membrane acid retention [100, 105, 106]. While research focus on the GDE has mainly looked at; improving the electrocatalyst [107], and reducing the sources of performance degradation for the GDE by optimising both the CL [7, 8, 77, 108-113] and GDL [7, 114]. The structure and composition of the CL plays a critical role in the MEA performance, and in the case of PBI-based MEAs the CL is composed of the electrocatalyst (typically *Pt/C*) which catalyses the electrochemical reactions, H_3PO_4 which acts as a proton conductor and facilitates proton transport, as well as a polymer binder to maintain the structural integrity of the CL. The polymer binder influences the structural properties of the electrode; it also maintains the structural integrity which affects mechanical stability and the porosity which in turn influences reactant permeability, and catalyst distribution influencing Pt utilisation. All of these factors contribute to the performance of the GDE.

Currently different types of polymer binders such as polytetrafluoroethylene (PTFE), polyvinylidene fluoride (PVDF), polyurethane, PBI, and various other polymers that

are capable of incorporating H_3PO_4 into their structure have been utilised in the CL of PBI-based HT-PEMFCs [110, 111, 115]. The aforementioned polymer binders have been studied and their influence on Pt utilisation has been evaluated [110, 115]; there is however, a need for an alternative to H_3PO_4 electrolyte in the catalyst layer to improve the low oxygen solubility and the sluggish ORR kinetics and catalyst deactivation occurring due to the H_3PO_4 electrolyte [95].

The present study aims to evaluate $CsHSO_4$ as a proton conductor in the CL for HT-PEMFCs and report for the first time that an inorganic solid acid such as $CsHSO_4$ can operate at 150-200 °C and undergoes a transformation at approximately 140 °C into a 'superionic' phase and exhibits high conductivity of 10^{-2} S.cm⁻¹. From the list of inorganic solid acids that exhibit good proton conductivity at elevated temperature, $CsHSO_4$ was chosen as the best candidate for use in HT-PEMFCs due to its high conductivity in the temperature range of interest to us (160 °C). Solid acids such as CsH_2PO_4 and RbH_2PO_4 exhibit high proton conductivity but in a temperature range that is not suitable for ABPBI-based HT-PEMFCs. $NH_4H_2PO_4$ solid acid exhibits good conductivity in the temperature range of interest but the phosphate anions would adsorb strongly onto the surface of the Pt electrocatalyst leading to catalyst deactivation [95]. Haile *et al.* [116] initially demonstrated its use as an electrolyte membrane in PEMFCs. Lavrova *et al.* [117] and Piao *et al.* [118] showed that $CsHSO_4$ composite electrolyte membranes can be produced with improved stability and conductivity. The effect of $CsHSO_4$, combinations of PTFE- $CsHSO_4$ and PVDF- $CsHSO_4$ on the performance of GDEs was evaluated in ABPBI-based HT-PEMFCs electrochemically by polarisation studies and EIS, and structurally by SEM and MIP.

4.2 Results and discussion

4.2.1 Structural analysis

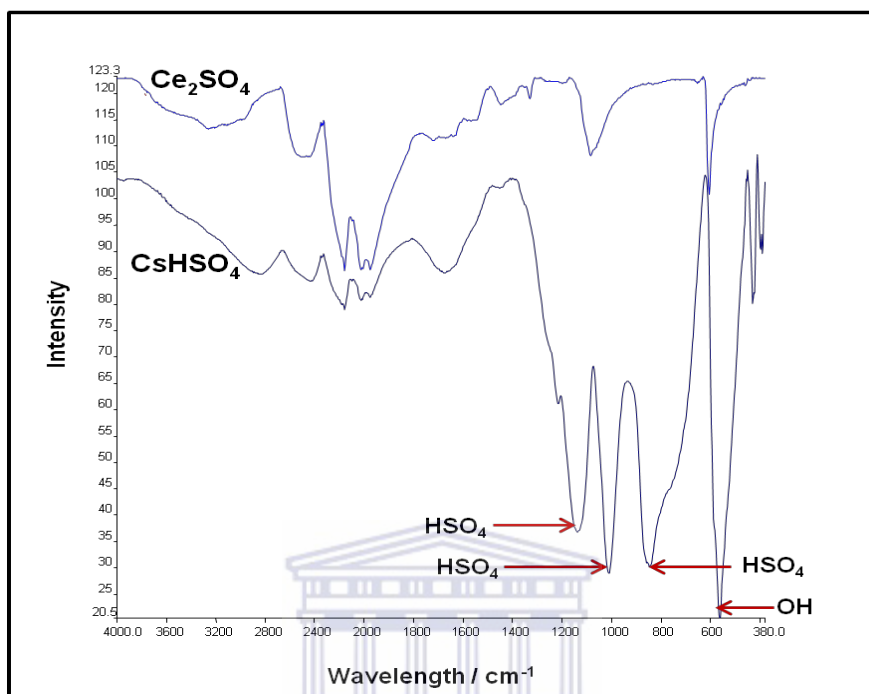


Fig. 4.1 FT-IR spectra of the Ce_2SO_4 starting material, and the $CsHSO_4$ synthesised product.

The FT-IR spectra of Ce_2SO_4 and the prepared $CsHSO_4$ are shown in Fig. 4.1, with the starting material Ce_2SO_4 included only as a frame of reference. The synthesised spectrum of $CsHSO_4$ shows bands at 848, 1012 and 1169 cm^{-1} indicating the presence of HSO_4^- , confirming the formation of the desired $CsHSO_4$ product. The $CsHSO_4$ spectrum also suggests the presence water, due to the absorption band at 560 cm^{-1} , most likely in the form of crystal water. Fig. 4.2(a)-(g) shows the HR-SEM micrographs of the GDEs fabricated with PTFE or PVDF binder and $CsHSO_4$. The images are taken at 5,000x magnification in Electron Backscatter Diffraction (EBSD) mode so that Pt distribution on the electrode surface can be observed, since high molecular weight elements such as Pt , appear much brighter than lower molecular weight elements e.g. carbon. The inserts are the 50,000x magnification HR-SEM

images taken in normal detector mode. The effect of using different binders and proton conductors in the CL can be observed from the structural morphology of the electrodes.

At 5,000x magnification morphology of the PVDF GDE (**Fig. 4.2(a)**) appears to be significantly different to that of the PTFE GDE (**Fig. 4.2(g)**). The PVDF GDE exhibits a smoother, more uniform distribution whereas the PTFE GDE, appears to have a rougher and more heterogeneous distribution. At 50,000x magnification the PVDF GDE particles appear to be more tightly packed with the consequence that the GDE appears to have less pores when compared to the PTFE GDE, in which the particles are more loosely associated and the GDE appears more porous in nature. The heterogeneous morphology observed in the PTFE GDE may be due to the colloidal nature that PTFE maintains in the catalyst ink which leads to the agglomeration of the catalyst nanoparticles (**Fig. 4.2(g)**). However, in the PVDF electrode (**Fig. 4.2(a)**) this effect is not observed as PVDF remains soluble in the catalyst ink and agglomeration of the catalyst particles is, hence, less likely to occur.

At 5,000x magnification the surface morphologies of PVDF- $CsHSO_4$ GDEs (**Fig. 4.2 (b, c)**) is almost indistinguishable from the PVDF GDE, but at 50,000x magnification it is possible to discern the effect of the addition of $CsHSO_4$ to the PVDF GDE. The PVDF- $CsHSO_4$ GDEs have particles that are more loosely packed than the PVDF GDE, with these PVDF- $CsHSO_4$ GDEs showing a more porous morphology than the

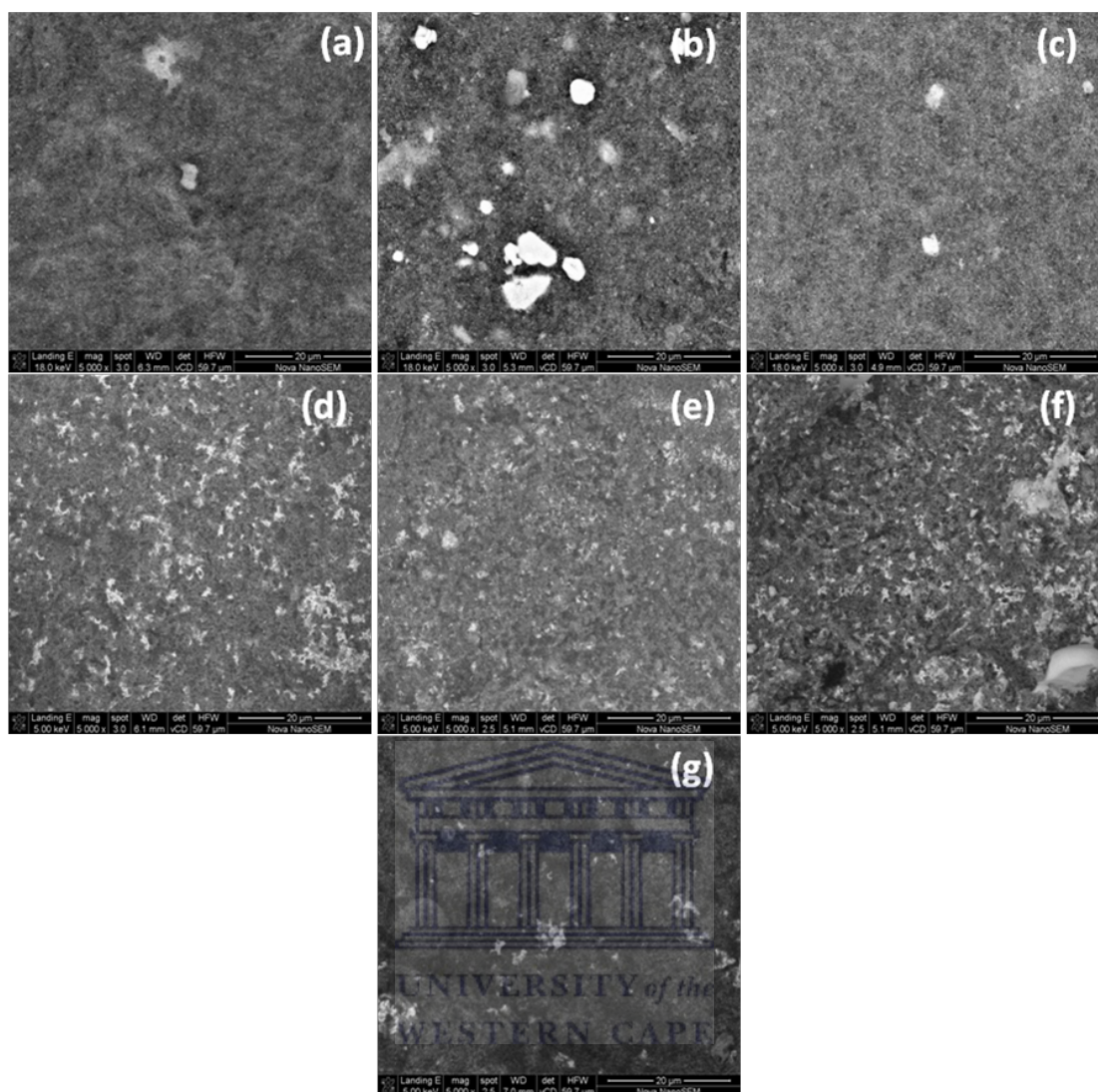


Fig. 4.2 SEM micrographs showing the surface morphology and porous structure of GDEs prepared with various polymer binders and $CsHSO_4$ proton conductor. (a) PVDF - 200 °C; (b) PVDF and 20% $CsHSO_4$ - 120 °C; (c) PVDF and 10% $CsHSO_4$ - 120 °C; (d) PTFE and 20% $CsHSO_4$ - 120 °C; (e) PTFE and 10% $CsHSO_4$ - 120 °C; (f) 10% $CsHSO_4$ - 120 °C; (g) PTFE - 200 °C.

PVDF GDE. In **Fig. 4.2(d, e)** the effect of the addition of $CsHSO_4$ to the PTFE GDE can be observed on the surface of the electrode, in that the *Pt* catalyst particles appear to form larger clusters than the GDEs prepared with the PVDF and PTFE binder (**Fig. 4.2(a, g)**), which may result from the impaired 'binding' effect of the polymer binders due to the existence of the inorganic particles. At 50,000x magnification (**Fig. 4.2(d)**-

(g) the morphologies of the GDEs are nearly indistinguishable from each other with the exception of the PTFE-20% $CsHSO_4$ GDE (**Fig. 4.2(d)**), in which we observe slightly larger pores.

The $CsHSO_4$ electrode (**Fig. 4.2(f)**) also shows a good Pt distribution but with less uniform surface than that of the PVDF electrode (**Fig. 4.2(a)**) which can be attributed to the 'binding' effect the PVDF polymer has on the CL, a property which $CsHSO_4$ lacks. For this reason the $CsHSO_4$ was used together with PVDF and PTFE binders, and the effect this addition had on the surface morphology of the GDEs can be observed in **Fig. 4.2(b)-(e)**, showing a smoother and more uniform layer than $CsHSO_4$ GDEs alone (**Fig. 4.2(f)**).

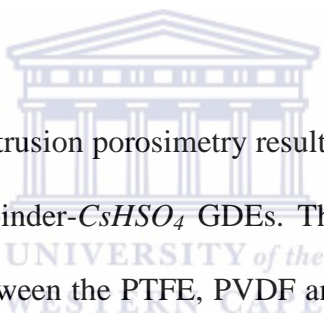


Fig. 4.3 shows the mercury intrusion porosimetry results obtained for the PTFE GDE, PVDF GDE as well as the binder- $CsHSO_4$ GDEs. The cumulative intrusion graph shows distinct differences between the PTFE, PVDF and binder- $CsHSO_4$ GDEs. The PVDF GDE has the fewest pores and is clearly the least porous of all the GDEs, these results confirm the porous microstructure observed in the SEM images (**Fig. 4.2(a)**).

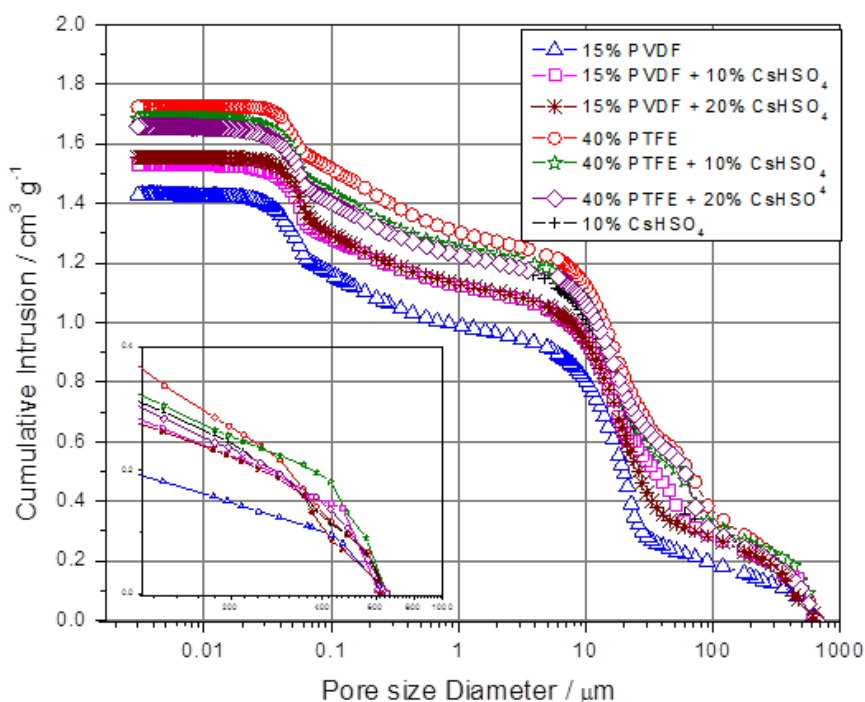


Fig. 4.3 Cumulative intrusion of the GDEs with various polymer binders and $CsHSO_4$ in the CL.

Addition of $CsHSO_4$ to the PVDF GDE effectively increased the number of pores and the pore size across all regions. The PVDF- $CsHSO_4$ GDEs exhibit similar porous structures except in the 20-70 μm macropore range, where the PVDF-10% $CsHSO_4$ GDE contains a larger number of pores in this region. The opposite effect is observed in the PTFE GDE, where the addition of $CsHSO_4$ has the effect of decreasing the pore volume of the GDE across almost the entire pore range except in the 300 – 600 μm range, with the PTFE- $CsHSO_4$ GDEs have a larger pore volume in this region which can be seen in the insert. Pore diameters $> 100 \mu m$ are more likely due to cracks on the GDE surface. These results are understandable considering that although $CsHSO_4$ is hygroscopic, the PTFE binder is hydrophobic and they may in essence cancel each other out. However, PTFE is insoluble in the catalyst ink, so large catalyst agglomerates are more likely to form, which would justify the larger macropore volume of the electrodes with CL containing PTFE and/or $CsHSO_4$ ingredients.

In the case of gas transport to the catalyst sites, the main contribution to gas transport will primarily be due to *Knudsen diffusion* in the micropores and a molecular diffusion mechanism in the macropores [119]. Better mass transport would be expected for the electrodes with larger volume of the macropores.

4.2.2 Electrochemical Analysis

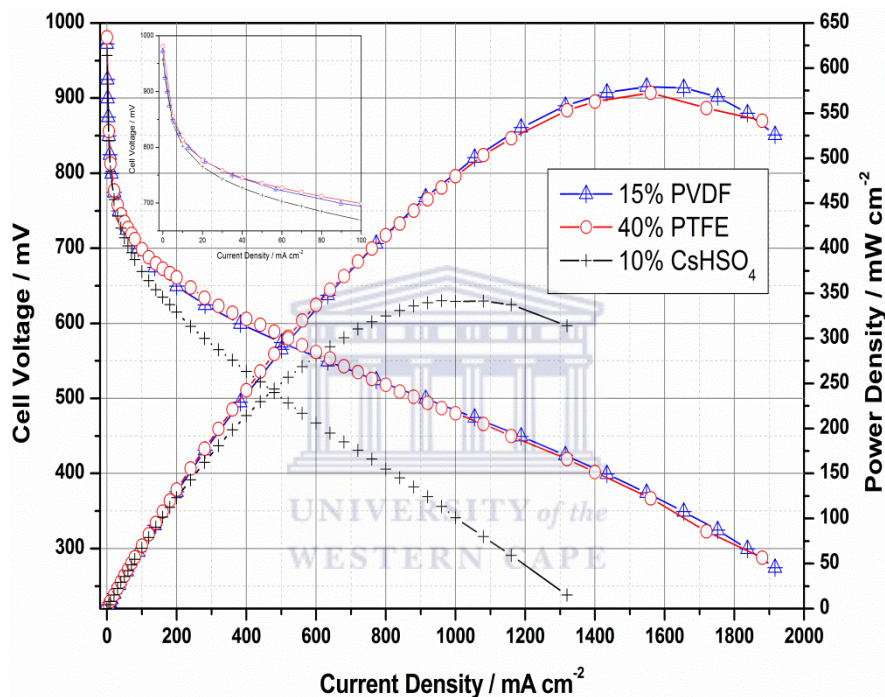


Fig. 4.4 Polarisation and power density curves for the MEAs with different polymer binders and *CsHSO₄* proton conductor.

The polarisation and power density curves for a single cell HT-PEMFC with PTFE, PVDF and *CsHSO₄* in the CL is depicted in **Fig. 4.4**. The results indicate that the MEAs with polymer binders show far greater performance than the MEA with the *CsHSO₄* proton conductor in the CL. At peak power, the MEA fabricated with the PVDF binder exhibits up to 69% higher power compared to the *CsHSO₄* MEA. This substantial difference can be attributed to the difference in the GDEs morphology,

with the $CsHSO_4$ lacking a 'binding' capability in the CL, with a consequential lack of structural stability in the $CsHSO_4$ GDE. The PTFE and PVDF MEAs exhibit nearly identical performance, with the PTFE MEA achieving maximum power density of $572.52 \text{ mW cm}^{-2}$ at 367 mV and the PVDF MEA reaching a maximum power density of $579.58 \text{ mW cm}^{-2}$ at 374 mV. At a cell voltage of +0.6 V the PTFE MEA reaches a higher current density of $\sim 440 \text{ mA cm}^{-2}$, which is almost 15% higher than the PVDF MEA which has a current density of $\sim 382 \text{ mA cm}^{-2}$ at the same cell voltage. Even though the PTFE and PVDF GDEs exhibit distinctly different porosity data, a larger number of macropores as exhibited by the PTFE GDEs should result in better mass transport than the PVDF GDE which has fewer macropores, but these two MEAs exhibit nearly identical performance. The EBSD HR-SEM images of the PVDF GDE shown in **Fig. 4.2(a)** reveals a better *Pt* catalyst distribution to the PTFE GDE (**Fig. 4.2(b)**), which could result in improved *Pt* utilisation and result in a performance comparable to a GDE with better porosity. The $CsHSO_4$ MEA has the lowest current density of 240 mA cm^{-2} at the same cell voltage, and is $\sim 45\%$ and 37% lower than the PTFE and PVDF MEAs respectively.

The insert in **Fig. 4.4** is the enlarged polarisation curve of the low current density region ($< 100 \text{ mA cm}^{-2}$). Closer examination of this region indicates that the initial voltage drop is smallest for the PTFE GDE and highest for the $CsHSO_4$ GDE (PTFE<PVDF< $CsHSO_4$). Since this region of the curve is determined by activation overpotential, which is largely controlled by the sluggish kinetics of the ORR, it can be assumed that the PTFE GDE has the faster reaction kinetics. The curves of the PTFE and PVDF MEAs are nearly identical in the linear region, indicating that these MEAs should exhibit similar ohmic resistances, whereas the $CsHSO_4$ MEA shows a

polarisation curve with a much steeper slope in the linear region, indicating that the ohmic resistance for this GDE is greater than that of the PVDF and PTFE GDEs. We postulate that the $CsHSO_4$ electrode lacks the structural integrity provided by the polymer network of the binders, leading to an increase in contact resistance. The high current density ($> 1000 \text{ mA cm}^{-2}$) region of the polarization curves displays no sharp drop from the ohmic region of the curves which would indicate that these MEAs are not significantly influenced by mass transport limitations. While relatively high flow rates were used to negate any mass transport limitations, based on the results obtained we do not expect mass transport limitations to affect the performance if stoichiometric flow rates are used.

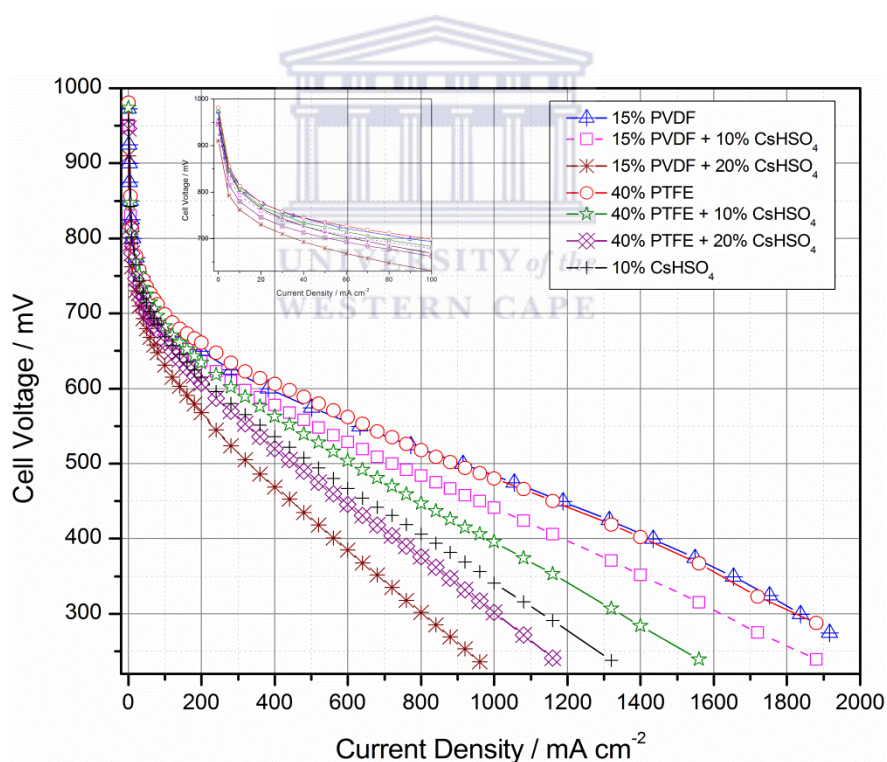


Fig. 4.5 Polarisation curves of the MEAs with different polymer binders and/or proton conductor in the CL of the GDEs.

A combination of the different binders and $CsHSO_4$ proton conductor in the CL was tested to evaluate whether the binder-proton conductor configuration improved the performance of the MEAs. **Fig. 4.5** depicts the polarisation curves for the MEAs with

different binders and $CsHSO_4$ proton conductor in the CL. At a working cell voltage of +0.6V the maximum current density is achieved by the PTFE MEA, with the PVDF-20% $CsHSO_4$ MEA exhibiting the lowest current density of 150 mA cm^{-2} at the same cell voltage. From the polarization curves we observe a decrease in current density at +0.6 V that follows the following trend: PTFE > PVDF > PVDF-10% $CsHSO_4$ > PTFE-10% $CsHSO_4$ > $CsHSO_4$ > PTFE-20% $CsHSO_4$ > PVDF-20% $CsHSO_4$. An enlarged image of the low current density region in **Fig. 4.5** is shown in the insert. The results show that the addition of the binders to the 10% $CsHSO_4$ GDE results in a smaller voltage drop when compared to the $CsHSO_4$ GDE, indicating that the addition of the binders improved the electrode kinetics of the $CsHSO_4$ GDE.

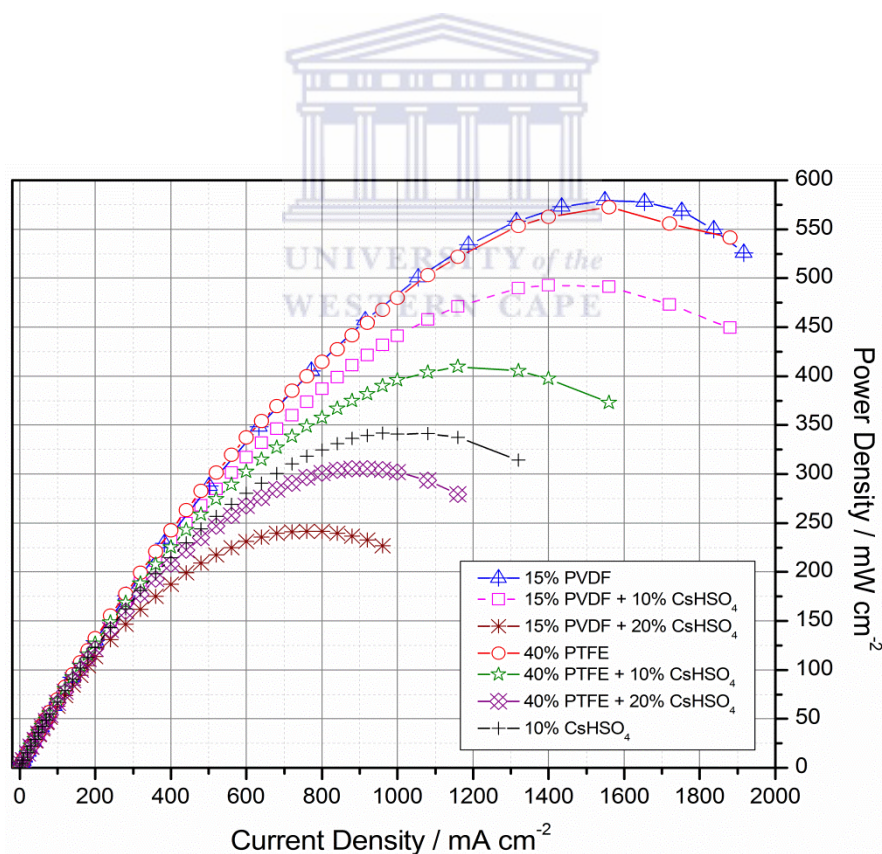


Fig. 4.6 Power Density curves of the MEAs with different polymer binders and/or proton conductor in the CL of the GDEs.

The binder-20 % $CsHSO_4$ MEAs exhibited the lowest performance of all the MEAs, indicating that high $CsHSO_4$ loadings in the CL is not beneficial for MEA performance. Clearly the lower amount (10%) $CsHSO_4$ combination with either polymer binder produces the better performance. The power density curves for the MEAs with different binders and $CsHSO_4$ proton conductor in the CL is illustrated in **Fig. 4.6**. It can be seen that the PVDF-10% $CsHSO_4$ MEA achieved the highest peak power density of the binder- $CsHSO_4$ MEAs reaching a maximum power density of 492.8 mW cm^{-2} at a cell voltage of +352 mV, which is nearly twice the value of 250 mW cm^{-2} at 350 mV achieved by Wannek *et al.* with Pt loadings of $\sim 1 \text{ mg cm}^{-2}$ Pt and 40% PTFE in the catalyst layer [5]. Although the results between Wannek *et al.* and this work are compared, a true comparison cannot be made since they used stoichiometric flow rates and the cells tested in this work utilised much higher flow rates so that mass transport limitations would not influence the performance of the GDEs. However, Wannek *et al.* used MEAs with an active area nearly three times larger than our active area.

Although the PTFE MEA exhibits nearly identical performance to the PVDF MEA when only the binders are used in the CL, the PVDF binder used in conjunction with 10% $CsHSO_4$ exhibits a peak power that is $\sim 20\%$ higher than when PTFE binder is used in conjunction with 10% $CsHSO_4$, the PVDF binder clearly poses the best choice for use with the $CsHSO_4$ in the CL. In order to obtain more information about the electrochemical characteristics of the GDEs prepared with the PTFE, PVDF binders and the $CsHSO_4$ inorganic solid acid, AC impedance was performed *in-situ* under the same operating conditions at a cell voltage of +0.6V. **Fig. 4.7** shows the measured impedance spectra of the MEAs with the various binders and proton conductor in the

CL of the GDEs. The total ohmic resistance, R_{Ω} , of the cell can be obtained from the high frequency intercept of the real axis and the R_{CT} can be estimated from the diameter of the low frequency and high frequency intercept.

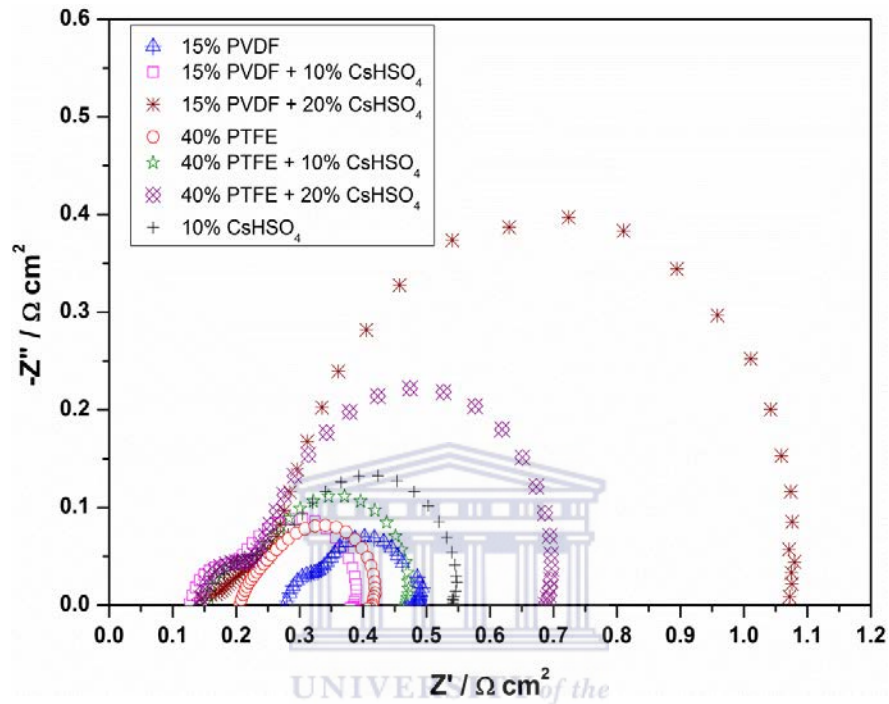


Fig. 4.7 *In situ* impedance spectra of the MEAs with different polymer binders and $CsHSO_4$ at a cell voltage of 0.6V.

Table 2 shows the results from measured impedance spectra as well as the *Tafel slopes* for the various MEAs. From the impedance spectra in **Fig. 4.7** it can be seen that there is no significant difference in R_{Ω} , with the exception of the PTFE and PVDF MEAs, since the R_{Ω} represents the total ohmic resistance of the cell which is made up of the contact resistance between the cell components and the ohmic resistance of the membrane, catalyst layer, gas diffusion layer, and bipolar plates [86]. The only differences in the MEAs is the composition of the catalyst layers, one may therefore conclude that the catalyst layer of the PTFE GDE has a much lower ohmic resistance, which if we refer to **Fig. 4.2(g)** can be attributed to the lower interfacial contact

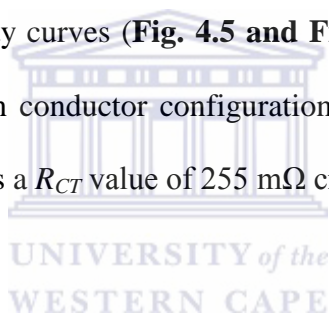
resistance provided by the PTFE GDE which has a more irregular surface with catalyst agglomerates which can lead to improved interfacial contact resistance due to the flexibility of the membrane and the cell assembly pressure exerted on the MEA [111]. This morphology is not observed in the PVDF GDE (**Fig. 4.2(a)**) and could be the reason for the higher ohmic resistance seen here.

Table 2 - Impedance and Tafel slope characteristics of the MEAs

GDE	% binder and/or proton conductor	Tafel slope (mV dec ⁻¹) ¹⁾	R_{Ω} (m Ω cm ⁻²) ²⁾	R_{CT} (m Ω cm ⁻²) ²⁾
PTFE	40%	91	208	208
PTFE- $CsHSO_4$	40% PTFE-10% $CsHSO_4$	92	152	316
	40% PTFE-20% $CsHSO_4$	92	145	546
PVDF	15%	105	280	208
PVDF- $CsHSO_4$	15% PVDF-10% $CsHSO_4$	92	131	255
	15% PVDF-20% $CsHSO_4$	87	146	926
$CsHSO_4$	10%	98	168	374

Nevertheless, it is clear that the MEAs containing $CsHSO_4$ as proton conductor in the CLs have lower R_{Ω} values than those for the MEAs with the polymer binder (i.e., PVDF GDE and PTFE GDE), this lower R_{Ω} in the $CsHSO_4$ MEAs can be attributed to the increased proton transfer in the CLs resulting from the use of proton conductor. It has been reported that the proton transport resistance in the CL causes a 45° (degree)-

straight line at the high-frequency region of the first arc [120], which can also be observed in the current study (**Fig. 4.7**), proving that the addition of $CsHSO_4$ proton conductor in the CL lowers the proton transport resistance. Another possible reason for the higher R_Q values for the PTFE and PVDF MEAs could be due to the membrane conductivity; although it is assumed that the membrane should have the same PA doping if the same membrane doping procedure is followed, subtle differences in the same membrane can result in different membrane conductivity. The lowest R_{CT} of $208 \text{ m}\Omega \text{ cm}^{-2}$ was achieved by the MEAs with the PVDF GDE as well as the PTFE GDE which indicates that these GDEs have the more efficient electrochemical active layer. These R_{CT} values confirm the results seen in the polarisation and power density curves (**Fig. 4.5 and Fig 4.6**). The lowest R_{CT} of the MEAs with the binder-proton conductor configuration was achieved by the PVDF-10% $CsHSO_4$ MEA which has a R_{CT} value of $255 \text{ m}\Omega \text{ cm}^{-2}$.



The PVDF-10% $CsHSO_4$ MEA exhibits a much lower charge transfer resistance than the 10% $CsHSO_4$ only MEA, suggesting that the addition of the polymer binder to the CL of the $CsHSO_4$ GDE improves the kinetics of the ORR in the catalyst layer of the GDE, this finding corresponds to the increased performance observed in **Fig. 4.5** and **Fig. 4.6**. The *Tafel plots* depicted in **Fig. 4.8** and the *Tafel slopes* summarised in **Table 2** were estimated from fitting the experimental data to:

$$E_{iR-Free} = a + b \log(i) \quad (4.1)$$

where $E_{iR\text{-Free}}$ is the iR free voltage of the low current density region of the polarization curve, a is a constant which depends on the electrodes and cell operating conditions, b is the *Tafel slope* and i is the current density. The *Tafel slopes* for the

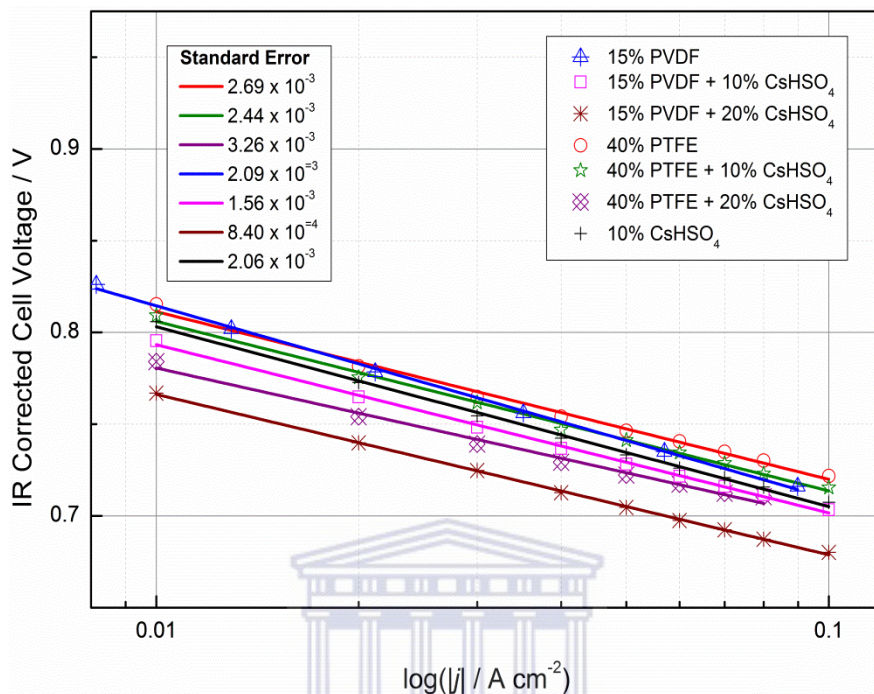


Fig. 4.8 *Tafel plots* for the ORR of the GDEs with different catalyst layer compositions.

MEAs with the combination of the polymer binders and proton conductor were all in the range of 87-105 mV dec⁻¹ which is well below the value of 120 mV dec⁻¹ obtained for PAFCs, and since the *Tafel slope* provides information on the kinetics of the ORR, it can be stated that in the case of the PVDF GDE the addition of *CsHSO₄* proton conductor improves the ORR kinetics in these electrodes as the PVDF GDE without any *CsHSO₄* previously exhibited the highest *Tafel slope* value of 105 mV dec⁻¹ indicating that this GDE has the slowest reaction kinetics. The addition of *CsHSO₄* to the PVDF MEAs improved the *Tafel slope* values and lowered ohmic resistance of these MEAs, whereas in the case of the PTFE MEAs the addition of *CsHSO₄* did not improve the *Tafel slope* values but also lowered the ohmic resistance of these MEAs. The binder-*CsHSO₄* MEAs exhibit higher charge transfer resistance values to the

binder GDEs as well as exhibiting lower performance. The advantages of the improved *Tafel slope* values in the PVDF- $CsHSO_4$ MEAs as well as the lower ohmic resistance values for both binder- $CsHSO_4$ MEAs are clearly negated by the higher charge transfer resistance of these MEAs. The lower performance exhibited by the binder- $CsHSO_4$ MEAs indicates that although the polymer binders improved the stability of the $CsHSO_4$ proton conductor in the CL, the resistance of $CsHSO_4$ to fuel cell environment still needs further improvement.

4.3 Conclusions

Composite GDEs were constructed using $CsHSO_4$ as the proton conductor and PVDF/PTFE as the polymer binder in the CL. The electrochemical analysis indicated that MEAs prepared with $CsHSO_4$ in the CL can efficiently lower the proton transfer resistance. However, the MEAs prepared solely using $CsHSO_4$ in the CL exhibited lower performance ($341.76 \text{ mW cm}^{-2}$ at 356 mV) than the MEAs prepared from GDEs using the polymer binders, possibly due to the hygroscopic nature of $CsHSO_4$ which absorbed moisture from the atmosphere during the air-spraying procedure and caused incomplete formation of the pore structure in the CL. The performance and R_{CT} of the $CsHSO_4$ GDEs was improved by addition of a polymer binder to the CL. The $CsHSO_4$ MEA provided the best performance when used in conjunction with a 15% PVDF binder, enabling the 15% PVDF-10% $CsHSO_4$ MEA to achieve a maximum power density of 492.8 mW cm^{-2} at 352 mV , further improvement in the single cell performance can be expected by further optimization of the binder and $CsHSO_4$ contents in the CL. Since $CsHSO_4$ inorganic solid acid is conductive in the $140^\circ\text{C} - 200^\circ\text{C}$ range, an operating temperature higher than 160°C may prove to be

beneficial in improving the performance of the MEAs based on these binder- $CsHSO_4$ GDEs, but this temperature is higher than 160 °C operating temperature which we've found to optimum for the ABPBI membrane.



Chapter 5: Evaluation of ZHP for improved proton conductivity in the catalyst layer

5.1 Introduction

Zirconium hydrogen phosphate, $Zr(HPO_4)_2$ (ZHP) is an insoluble solid that has been intensively studied as a proton conducting solid electrolyte. ZHP exhibits a layered structure (which allows for intercalation of “guest” molecules) as well as cation exchange properties [121]. In addition to these cation exchange properties, it also displays good proton conductivity as a result of high proton mobility on the surface of ZHP [122], and high hygroscopicity at elevated temperatures which make it extremely attractive for use as polymer electrolyte [123, 124]. At 80 °C, amorphous ZHP in water exhibits a proton conductivity of $\sim 0.01 \text{ S cm}^{-1}$, which has led to several studies in which ZHP is incorporated into non-conducting polymers such as PTFE [125, 126] as well as conducting polymers such as Nafion[®] [64]. These electrolytes are modified with ZHP to improve the moisture content and thermal stability of these membranes [63, 64, 127]. Since the incorporation of ZHP into electrolyte membranes has proven to be beneficial for moisture content and improved performance at temperatures above 100 °C, its presence in the CL should be beneficial for similar reasons. Xie *et al.* investigated the influence of ZHP in the CL of GDEs for MEAs based on Nafion[®] membrane and found that below 100 °C, the performance remained similar to GDEs containing Nafion[®] only, however, above 100 °C the ZHP/Nafion GDEs showed improved performance over the conventional Nafion GDEs [128]. For the same reasons, introducing ZHP into HT-PEMFC systems should also prove beneficial as there is a need for stable proton conductivity at elevated temperatures.

In this study, ZHP was incorporated into the CLs of ABPBI-based HT-PEMFC along with a non-conducting polymer (PTFE), without additional H_3PO_4 doping, to evaluate the effects of ZHP on (i) the fuel cell performance and (ii) the stability of the resulted GDEs. In summary, this work expands on the work carried out by Xie *et al.* [128], by incorporating ZHP into the CLs of ABPBI-based HT-PEMFC. Similar techniques and methodologies are applied in this work, which at the same time, is considered to be a new step in the optimisation challenge of the HT-PEMFC systems.

5.2 Results and Discussion

5.2.1 Influence of ZHP on the catalyst layer structure

Table 3: Specifications of the GDEs.

GDE	Catalyst type (% Pt/C)	Pt loading	wt.% ZHP in CL (re. dry PTFE)	wt.% PTFE (re. Pt/C)
GDE-1	40	1 mg cm ⁻²	0	40
GDE-2	40	1 mg cm ⁻²	20	40
GDE-3	40	1 mg cm ⁻²	30	40
GDE-4	40	1 mg cm ⁻²	40	40
GDE-5	40	1 mg cm ⁻²	50	40

The specifications of all the GDEs prepared in this study are shown in **Table 3**. The SEM micrographs of the GDEs prepared with 40% PTFE and 40% PTFE-30% ZHP combinations are depicted in **Fig. 5.1(a, b)**. In order to perform a systematic comparison between the GDEs, the images were taken in secondary electron detector

mode (EBSD) at 1,000x magnification. The hand spraying method for deposition of the catalyst ink results in an uneven deposition of the catalyst, and as a result large lumps can be observed on the surface of both GDEs. The Zr particles are observed as white clusters in **Fig. 5.1(b)**. Looking at the 50,000x magnification inserts in **Fig. 5.1**, one may observe that both GDEs exhibit a porous microstructure necessary for transport of reactant gases to the catalyst sites, with no distinguishable differences observed in the GDEs. Elemental analysis data shown in **Table 4** revealed a nearly uniform distribution of zirconium in the CL of GDE-3, with a 1:3 ratio for *Zr:Pt* which meets the design requirements.

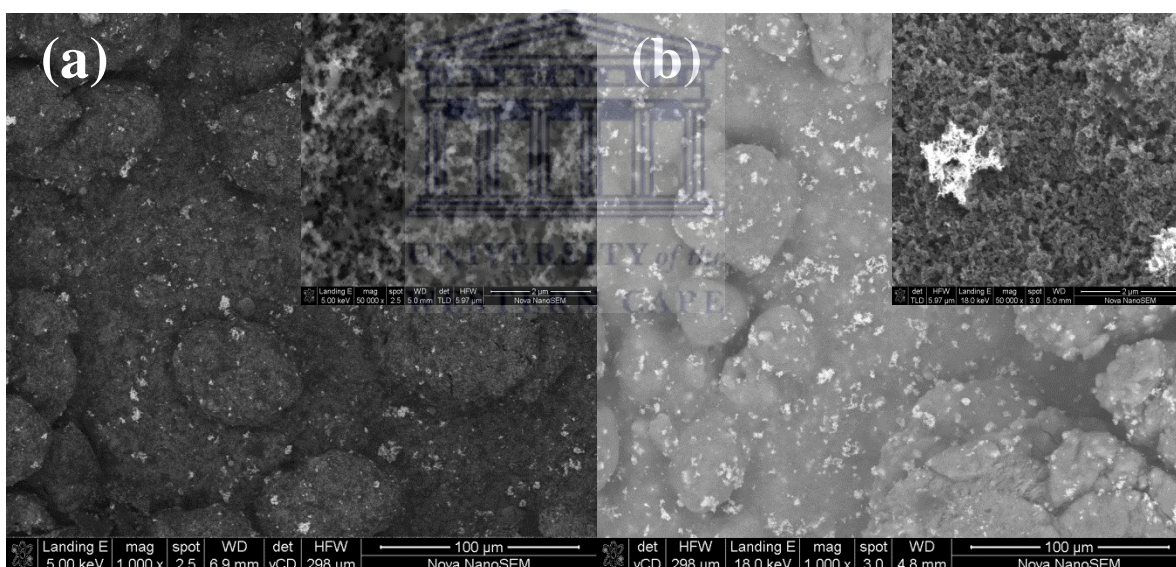


Fig. 5.1 Surface morphologies with inserts of CL pore structure of (a) PTFE-GDE (GDE-1) and (b) 30% ZHP/PTFE-GDE (GDE-3).

Table 4: Elemental Analysis (all results in wt.%)

Spectrum	In stats.	C	F	Zr	Pt	Total
Spectrum 1	Yes	50.75	22.85	6.6	19.8	100
Spectrum 2	Yes	52.58	23.45	5.83	18.15	100

The effect of various ZHP loadings on the GDE surface morphology and CL microstructure is illustrated in **Fig. 5.2**. Increasing the ZHP loading effectively causes a corresponding increase in the uneven nature of the surface of the GDEs, with more lumps and agglomerates observed for the higher ZHP loadings (**Fig. 5.2(b,c)**). Little difference in the porous microstructure of the GDEs is observed in the high magnification inserts of **Fig. 5.2**.

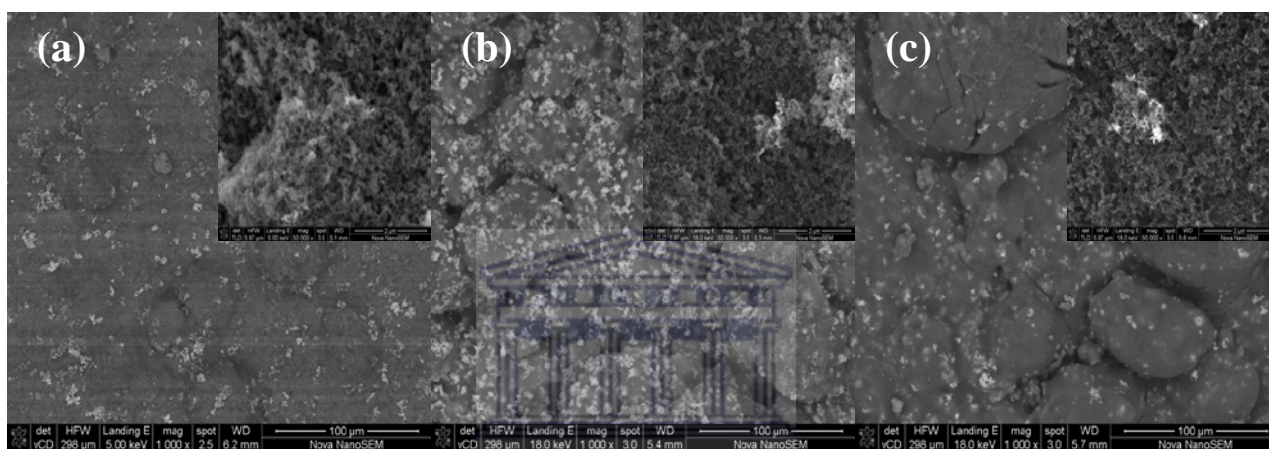


Fig. 5.2 Surface morphologies with inserts of CL pore structure of (a) 20% ZHP/PTFE-GDE (GDE-2), (b) 40% ZHP/PTFE-GDE (GDE-4) and 50% ZHP/PTFE-GDE (GDE-5).

A more detailed analysis of the microstructure of the GDEs can be obtained from the porosimetry data. **Fig. 5.3** shows a comparison of intrusion data for the 30% ZHP/PTFE-GDE (GDE-3) and PTFE-GDE (GDE-1). It can be seen that the addition of ZHP to the CL causes a slight decrease in the number of pores in the $< 0.03 \mu\text{m}$ region, indicating a slight reduction in the number of micropores upon addition of ZHP, indicating that the ZHP could be filling the smaller diameter pores during the formation of the CL, which corresponds to the findings of Xie *et al* [128]. However, introducing ZHP in the CL results in an increased pore volume for the macropores (60-100 μm region), which may have originated from the increase in the number of catalyst agglomerates in the CL due to the increased ZHP content.

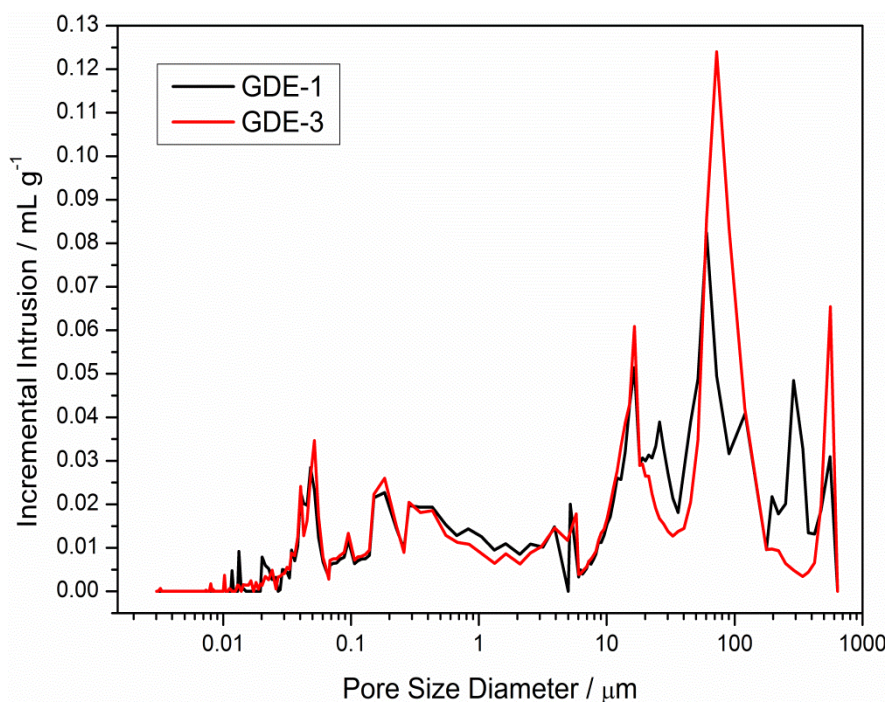


Fig. 5.3 Mercury intrusion porosimetry curves showing the incremental intrusion of the PTFE-GDE (GDE-1) and the 30% ZHP/PTFE-GDE (GDE-3).

Fig. 5.4 shows the intrusion data for the GDEs with varying ZHP loadings, GDEs (2-5). The porosimetry data shows that the ZHP/PTFE-GDEs have similar intrusion volumes across all pore sizes with the exception of the macropore region (30-100 μm), where the 30% ZHP/PTFE GDE (GDE-3) shows a higher pore volume than the other ZHP/PTFE GDEs. A higher pore volume in this region is beneficial for the molecular diffusion mechanism of gas to the catalyst sites [119]. GDEs with higher pore volumes in this region are expected to have better mass transport properties in high current density regions.

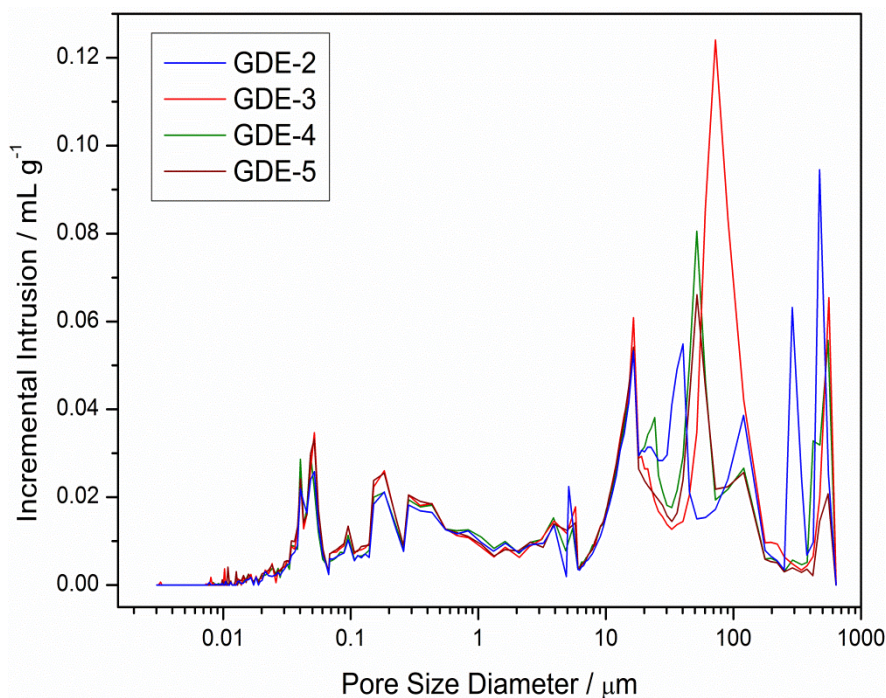


Fig. 5.4 Mercury intrusion porosimetry curves showing the incremental intrusion for the GDEs with varying ZHP concentrations in the CL; GDE-2 (20% ZHP/PTFE), GDE-3 (30% ZHP/PTFE), GDE-4 (40% ZHP/PTFE) and GDE-5 (50% ZHP/PTFE).

5.2.2 Single cell performance

Fig. 5.5 shows the performance curves for two MEAs with differing CL compositions in the GDEs. The performance of the MEA based on the PTFE-GDE (GDE-1) shows a lower performance than that achieved by the ZHP/PTFE-GDE (GDE-3), indicating that the addition of ZHP to the CL enhances the performance of the MEA, particularly in the medium and high current density regions of the polarisation curve. The maximum power density of the two MEAs is achieved by GDE-3, with 592 mW cm^{-2} at a cell voltage of +380 mV, which is an improvement of approximately 14% over GDE-1 which only achieved a maximum power density of 518 mW cm^{-2} at a cell voltage of +331 mV. The polarisation curves also show that at a working cell voltage of +600 mV GDE-3 reaches a current density of 399 mA cm^{-2} , which is approximately 25% higher than that achieved by GDE-1 (320 mA cm^{-2}) at the same cell voltage. Detailed analysis of the polarisation curves shows that the GDEs have a

similar voltage drop in the low current density region ($< 100 \text{ mA cm}^{-2}$) of the curve, indicating the electrodes have similar reaction kinetics. Since the voltage drop in this region is predominantly determined by sluggish ORR kinetics, it can be stated that introducing $\text{Zr}(\text{HPO}_4)_2$ in the CLs does not affect ORR kinetics.

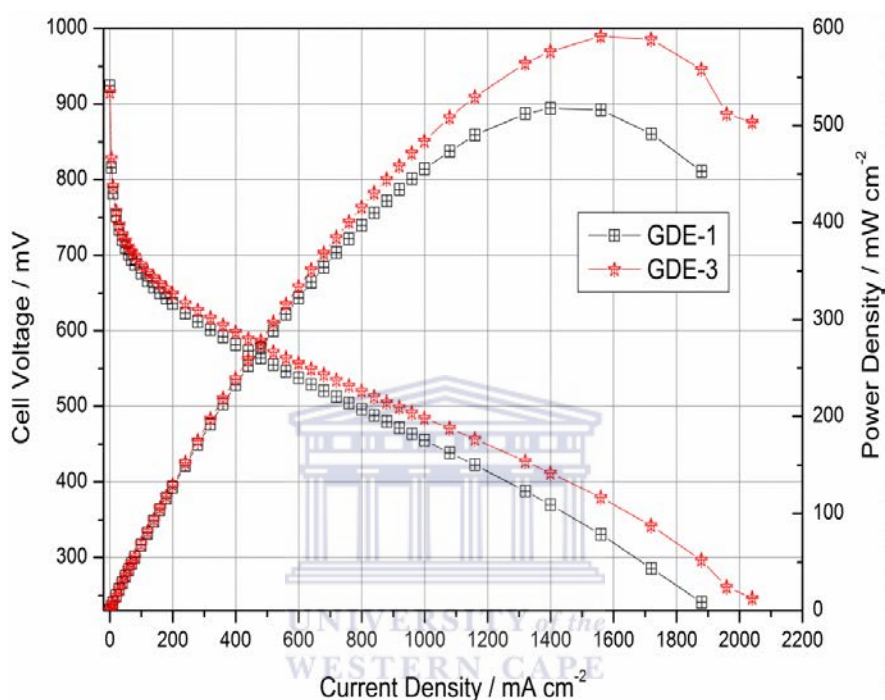


Fig. 5.5 Performance curves for the MEAs prepared with 40% PTFE in the CL (GDE-1) and 40% PTFE and 30% ZHP in the CL (GDE-3).

Analysis of the linear region of the polarisation curve shows that MEAs exhibit similar decreasing slopes, while GDE-1 exhibits slightly lower performance than GDE-3 in this region. This observation indicates that the MEAs have similar ohmic resistances, as this region of the polarisation curve is influenced by ohmic resistance. The high current density region ($> 1,000 \text{ mA cm}^{-2}$) of the curve which is influenced by mass transport limitations, shows that both GDEs are not significantly influenced by mass transport limitations as no sharp drop from the linear region of the curve is observed for either MEA. GDE-3 exhibits a better performance than GDE-1 in the

high current density region, it can thus be stated that GDE-3 has better mass transport properties, which corresponds to the larger number of macropores exhibited in **Fig. 5.3**. This apparent lack of mass transport limitations for the GDEs may be attributed to: (i) the increase in temperature leading to not only in an increase in the reaction rate but also an increase in the gas diffusion rate through the electrolyte membrane as well as the GDE and, (ii) a single phase of gaseous water leading to an increased surface area of the catalyst and improving the ability of reactant gases to diffuse into the reactant layer, as gaseous water does not block the active sites as liquid water does in LT-PEMFCs, as the phenomenon of catalyst flooding does not occur in HT-PEMFCs [6, 59, 129].

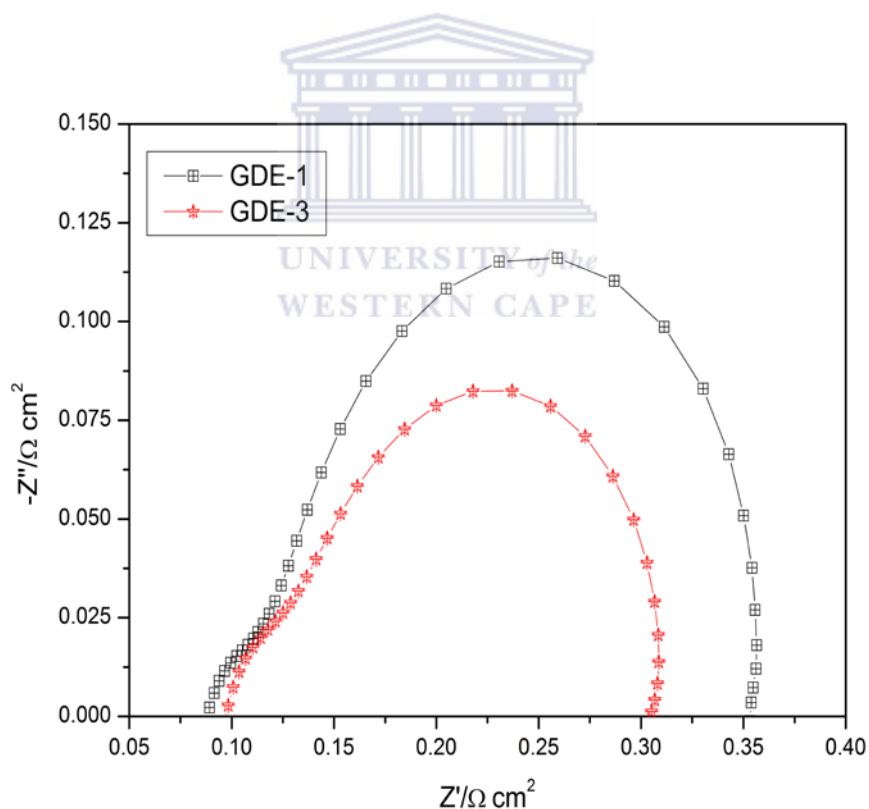


Fig. 5.6 *In-situ* impedance curves of the MEAs for GDE-1 and GDE-3, at a cell voltage of +0.6 V

Fig. 5.6 shows the *in-situ* impedance curves of the single cells with the two different GDEs obtained at +0.6 V. The high frequency intercept with the x -axis shows that the MEAs have similar ohmic resistances, whereas the charge transfer resistances show a

significant difference for these two MEAs. Since the charge transfer resistance can be calculated from the diameter of the arc, it is clear that the MEA of GDE-3 has the lowest charge transfer resistance, implying that this GDE has the more efficient electrochemical active layer, which can be attributed the increased proton conductivity of the CL due to the incorporation of ZHP.

5.2.3 Influence of ZHP content on MEA performance

Fig. 5.5 clearly shows that the addition of ZHP to the catalyst layer of the GDE increased the MEAs performance, however, an investigation into the effect of different ZHP concentrations shows that an optimum value for ZHP in the catalyst layers exists. In this study 20-50 wt.% ZHP in relation to dry PTFE was evaluated in the CL. Fig. 5.7 shows the performance curves of the MEAs with different ZHP contents in the CL.

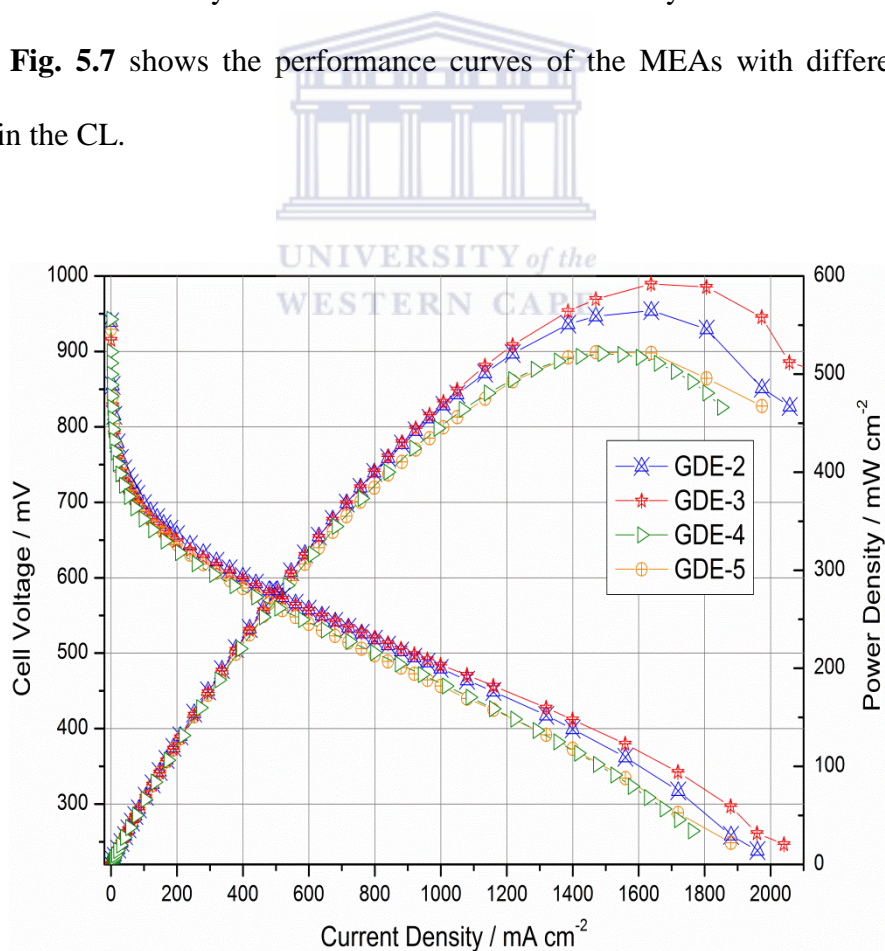


Fig. 5.7 Performance curves for the MEAs with different ZHP content in the CLs.

For comparison purposes, plots of current density at +600 mV *versus* ZHP content in CL and power density *versus* ZHP content in CL are shown in **Fig. 5.8** and **Fig. 5.9** respectively. In **Fig. 5.8** it can be observed that the cell performance is slightly improved by increasing ZHP content from 20 wt% to 30 wt% in the CLs, however further increase of ZHP content to 40 wt% and 50 wt% leads to a dramatic drop at the same cell voltage, which could be attributed to the increased ohmic resistance due to higher ZHP content in these CLs.

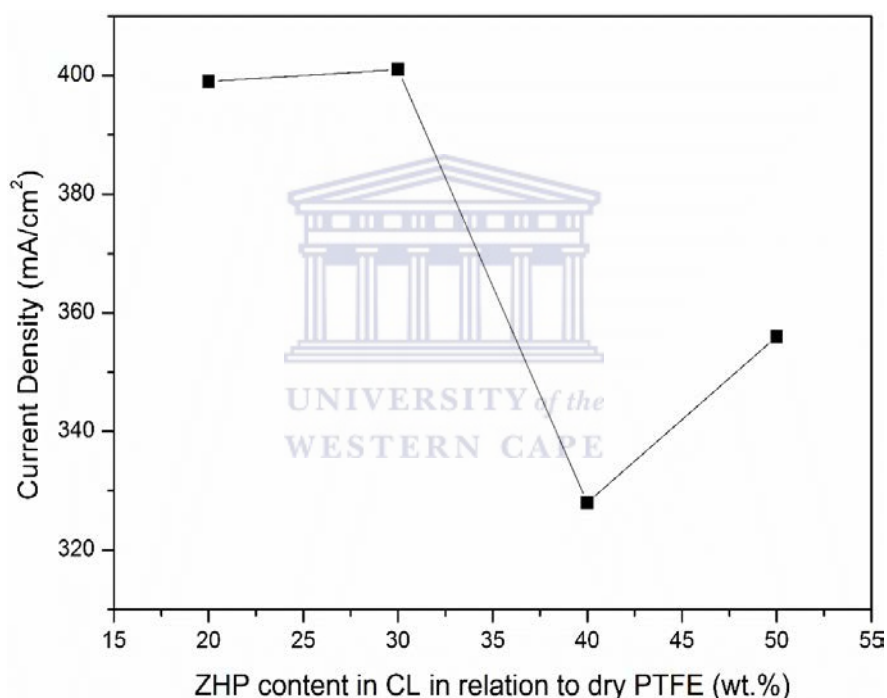


Fig. 5.8 Current density at 600 mV versus the ZHP content in CL.

The increased ohmic resistance values for the MEAs containing the higher ZHP content can be explained by the decrease in micropores observed upon the addition of ZHP to the CL, while small amounts of ZHP improves the electrochemical active layer and fills only a smaller number of micropores, higher amounts of ZHP in the CL results in too much ZHP filling the smaller diameter pores which leads to a less efficient electrochemical active layer and an increase the ohmic resistance of the CL.

The same trend is observed in **Fig. 5.9** where the maximum power density is achieved by GDE-3, with 592 mW cm^{-2} achieved at $+380 \text{ mV}$. It is clear from these graphs that high ZHP contents (40 wt.% and 50 wt.%) in the CL are not favourable to higher fuel cell performance.

Although MEAs with GDE-2 and GDE-3 reach similar current densities at $+600 \text{ mV}$ (**Fig. 5.8**), the peak power densities reached by these MEAs show a distinct difference (**Fig. 5.9**). In the medium current density region these MEAs exhibit similar performance, but GDE-3 clearly outperforms GDE-2 in the high current density region. Normally, the fuel cell performance in the high current density region is related to mass transport limitations, therefore it is clear from **Fig. 5.5(a)-(c)** that GDE-3 has the superior CL composition in terms of mass transport properties and MEA performance due to the optimized ZHP content.

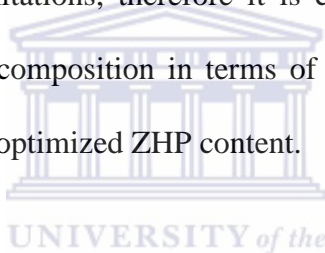


Table 5. Impedance and Tafel slope characteristics of the various GDEs.

GDE -#	GDE-1	GDE-2	GDE-3	GDE-4	GDE-5
$R_{\Omega} (\Omega \text{ cm}^2)$	0.087	0.104	0.096	0.114	0.105
$R_{ct} (\Omega \text{ cm}^2)$	0.344	0.210	0.207	0.224	0.241
<i>Tafel slope</i> (mV dec^{-1})	87	98	84	87	96

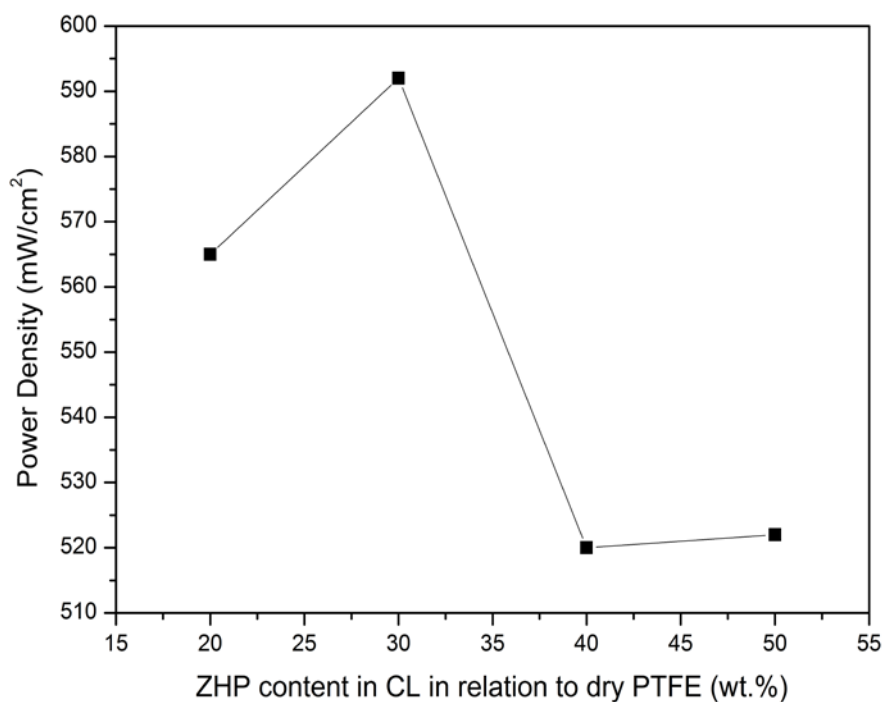


Fig. 5.9 Maximum Power density versus ZHP content in CL.

The *in-situ* impedance curves of the four MEAs at a cell voltage of +0.6 V are shown in **Fig. 5.10**. The high-frequency intercept on the real axis represents the total ohmic resistance of the single cell, while the diameter of the arc is a measure of the charge transfer resistance of the ORR. Through simulation with Autolab software, the cell resistances (R_{Ω}) and charge transfer resistances (R_{ct}) of the single cell with the different GDEs can be calculated, and summarised in **Table 5** along with the calculated *Tafel slopes* for the *Tafel* plots shown in **Fig. 5.11**. It can be seen that GDE-3 possesses the lowest ohmic resistance and charge transfer resistance, indicating a more efficient electrochemical active layer due to the optimum ZHP content in the CL. High resistances are observed with GDEs containing high ZHP contents (40 wt.% and 50 wt.%), these results are certainly consistent with their performances showed in fuel cell operation (**Fig. 5.7**). The values for the *Tafel slopes* range between 84-98 mV dec⁻¹, with the GDE-3 exhibiting the lowest *Tafel slope*

value of 84 mV dec^{-1} indicating that the addition of ZHP to the slightly improves the ORR kinetics.

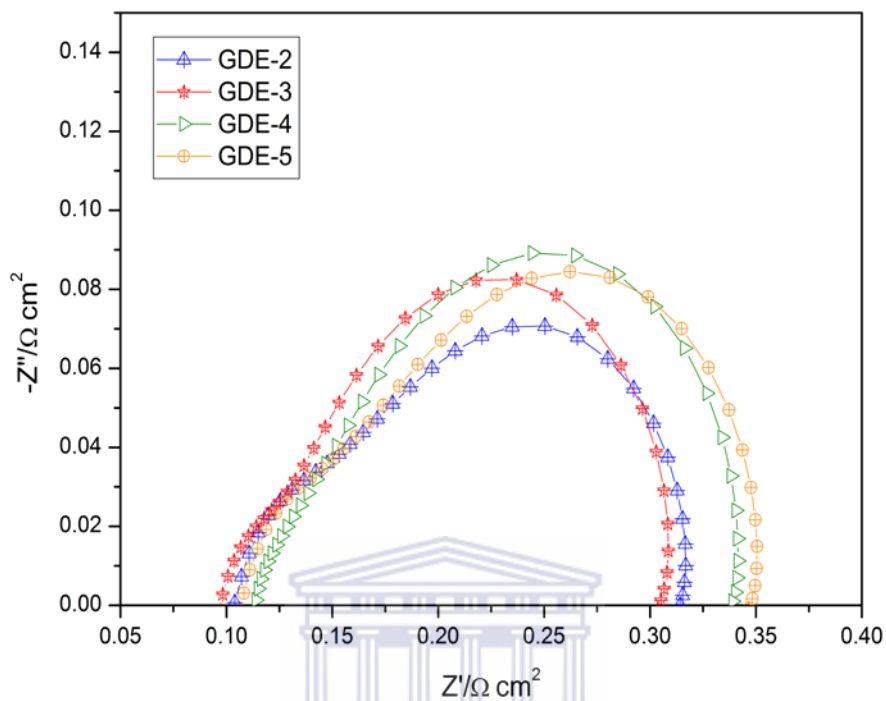


Fig. 5.10 *In-situ* impedance curves for MEAs with differing ZHP contents in CL, at a cell voltage of +0.6 V.

UNIVERSITY of the
WESTERN CAPE

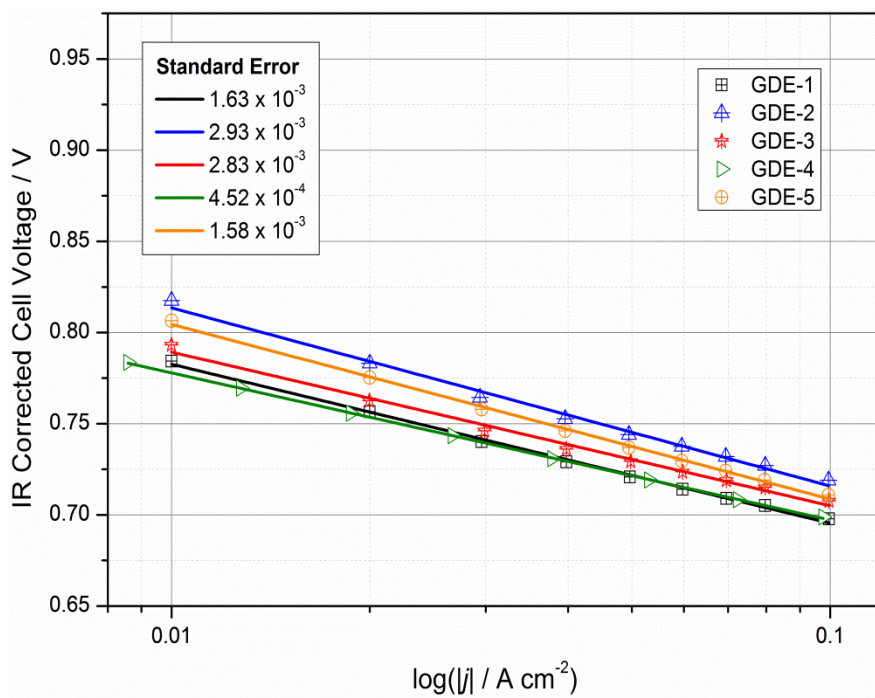


Fig. 5.11 Tafel plots for the ORR of the GDEs with different catalyst layer compositions.



5.2.4 Stability

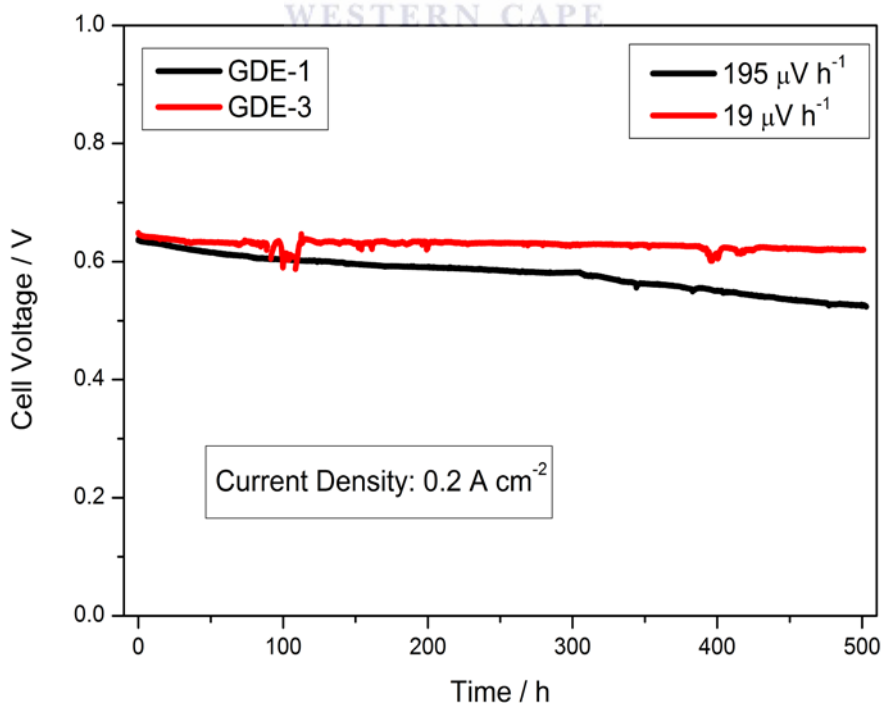


Fig. 5.12 Stability of GDE-1 and GDE-2 MEAs performance, operating for 500 h at 0.2 A cm^{-2}

Since stability and durability characteristics are one of the main challenges associated with HT-PEMFCs [59], a short term stability analysis study was performed for 500 h at $j = 0.2 \text{ A cm}^{-2}$, as shown in **Fig. 5.12**. The experiment was started after performing two polarisation tests which took place on two successive days, the cell voltage at 0.2 A cm^{-2} was at its maximum directly after the second polarisation test was performed. As can be seen in **Fig. 5.12**, the MEA of GDE-3 maintains a stable performance for the duration of the study, with the exception of the occurrence of minor fluctuations due to a disruption in H_2 gas supply to the cell, the cell voltage shows no major decrease at 0.2 A cm^{-2} . When the stability of GDE-1 is compared with that of GDE-3, it can be observed that GDE-1 has a much steeper slope than that of GDE-3. Linear regression of the cell voltage data obtained for the MEAs reveals that the degradation rate of GDE-3 is as low as $\sim 19 \mu\text{V h}^{-1}$, while GDE-1 shows a much higher degradation rate of $\sim 195 \mu\text{V h}^{-1}$. The high degradation rate exhibited by the MEA of GDE-1 is most likely due to the catalyst ink deposition method used to prepare the GDEs. Since the only difference between these two MEAs are the different compositions of the CLs, it can be stated that the addition of the 30 wt.% $\text{Zr}(\text{HPO}_4)_2$ (re. dry PTFE) to the CL can greatly increase the stability of the cell performance. The degradation rate of $\sim 19 \mu\text{V h}^{-1}$ obtained by GDE-3 is well within the range for those reported by other researchers' ($4.9 - 25 \mu\text{V h}^{-1}$) [130-134]. The good stability displayed by GDE-3 can be explained by; the good thermal stability provided by ZHP combined with the improved proton conductivity at higher temperatures. Therefore, incorporating the hygroscopic ZHP particles in the CL, which aids the proton conductivity and stability of the GDE at higher operating temperature, is believed to be the main reason for the GDE-3 showing high performance and good durability.

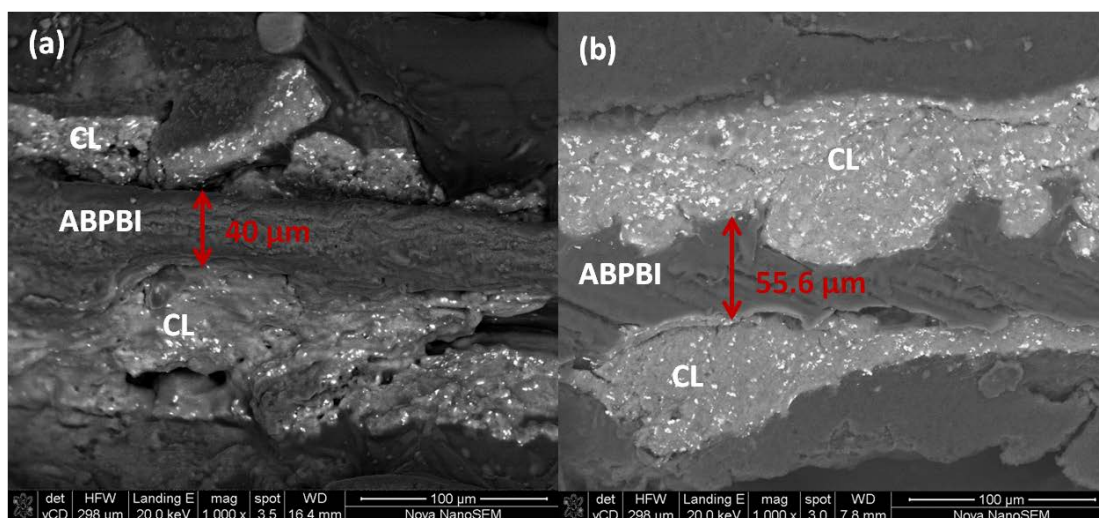


Fig. 5.13 SEM images of the cross-sections of the MEAs after the durability test: (a) GDE-1 MEA and (b) GDE-3 MEA.

Fig. 5.13 shows the SEM images of the MEA cross-sections that were taken after the completion of the stability test. The MEAs were set in resin and polished in order to obtain accurate cross-sections. Analyses of the post-test images shows that the MEA of GDE-1 (**Fig. 5.13(a)**) has a significantly thinner average membrane thickness when compared to the MEA of GDE-3 (**Fig. 5.13(b)**), exhibiting a thickness of 40 μm and 55.6 μm respectively. Whereas a freshly doped, untested membrane has a thickness of approximately 80 μm, which through cell compression of the MEA can be noticeably reduced. If we consider that the MEAs differ only in CL composition, yet they still exhibit different membrane thickness. This would suggest that the MEA of GDE-3 retains a higher PA doping in the membrane than the MEA of GDE-1 after the stability test, hence the ZHP in the CL of GDE-3 exerts a positive influence on PA hydration due to its hygroscopic properties. **Fig. 5.13(a)** also clearly shows a greater degree of CL separation from the membrane in comparison to **Fig. 5.13(b)**, indicating

that the unique CL of GDE-3 has a positive influence on the acid retaining ability of the membrane which improves the MEAs stability.

5.3 Conclusions

Incorporating ZHP into the CL of GDEs yielded high performances of ABPBI-based MEAs. A 30 wt.% ZHP (re. dry PTFE) content in the CL yielded the best performing MEA, which achieved peak power of 592 mW cm^{-2} at a cell voltage of 380 mV cm^{-2} . An increase in ZHP content in the CL led to lower performances, indicating that lower ZHP contents in the CL are more beneficial for achieving high power densities. A reduction in charge transfer resistance was observed for the ZHP GDE when compared to the GDE containing PTFE-only, indicating that the addition of ZHP can increase the proton conduction of the CL. The MEA showed good stability in a short term operation: the cell voltage remained at $\sim +0.65 \text{ V}$ without obvious drop after the 500 h operation at 0.2 A cm^{-2} . It may be stated that an optimum content of ZHP in the CL benefits the performance and stability of ABPBI-based HT-PEMFC.

Chapter 6: Development of ceramic carbide acid-controlling region

6.1 Introduction

HT-PEMFCs are in many respects very similar to PAFCs, with differences in operating temperatures and in electrolyte configuration. PAFCs typically operate at temperatures of $\sim 200\text{ }^{\circ}\text{C}$, whereas HT-PEMFCs generally operate well below $200\text{ }^{\circ}\text{C}$. Although both these fuel cells rely on phosphoric acid as the proton conducting electrolyte; PAFCs use 100% phosphoric acid immobilised in a matrix, whereas HT-PEMFCs typically use a PBI/ABPBI-based membrane that is doped with phosphoric acid [48].

Phosphoric acid has many attractive features for use as an electrolyte at high temperature operation; stability ($200\text{ }^{\circ}\text{C}$), low vapour pressure, ability to use air as the oxidant and tolerance to CO ($200\text{ }^{\circ}\text{C}$). These features are mostly applicable to operation at $200\text{ }^{\circ}\text{C}$, so when lower temperatures are used certain drawbacks such as slower ORR rate due to the stronger adsorption of the phosphate anions onto the Pt surface and its low acidity at lower temperatures come into play. In PAFCs operating at $200\text{ }^{\circ}\text{C}$, the phosphoric acid is polymerised to pyrophosphoric acid, and these pyrophosphoric acid anions adsorb onto the Pt catalyst to a lesser degree than phosphoric anions resulting in higher ORR rates [135]. This strong adsorption of phosphoric anions onto Pt proves to be particularly problematic as HT-PEMFCs require high concentrations of phosphoric acid for sufficient membrane proton conductivity, yet at the same time the phosphoric acid makes gas transport difficult within the electrodes and hinders the electrode reactions due the strong phosphate anion adsorption [136]. The phosphoric acid dopant in the membranes is not 'fixed', so

HT-PEMFCs face yet another issue of phosphoric acid leaching from the membrane. Excess phosphoric acid could flood the electrodes and block the gas transport channels leading to a decrease in performance as well as reducing the membrane conductivity [133, 137, 138]. Long-term durability would hence need to reduce the phosphoric acid leaching and prevent the phosphoric acid electrolyte from flooding the electrodes. There is therefore a need for a novel MEA architecture which could act as a barrier to prevent excessive phosphoric acid from flooding the electrode as well as preventing the loss of phosphoric acid from the MEA. This study serves to develop such a novel architecture by incorporation of an acid-controlling region into the MEA structure. The acid-controlling region is illustrated in the MEA schematic in **Fig. 6.1(a)** and on the surface of the GDE (**Fig. 6.1(b)**).

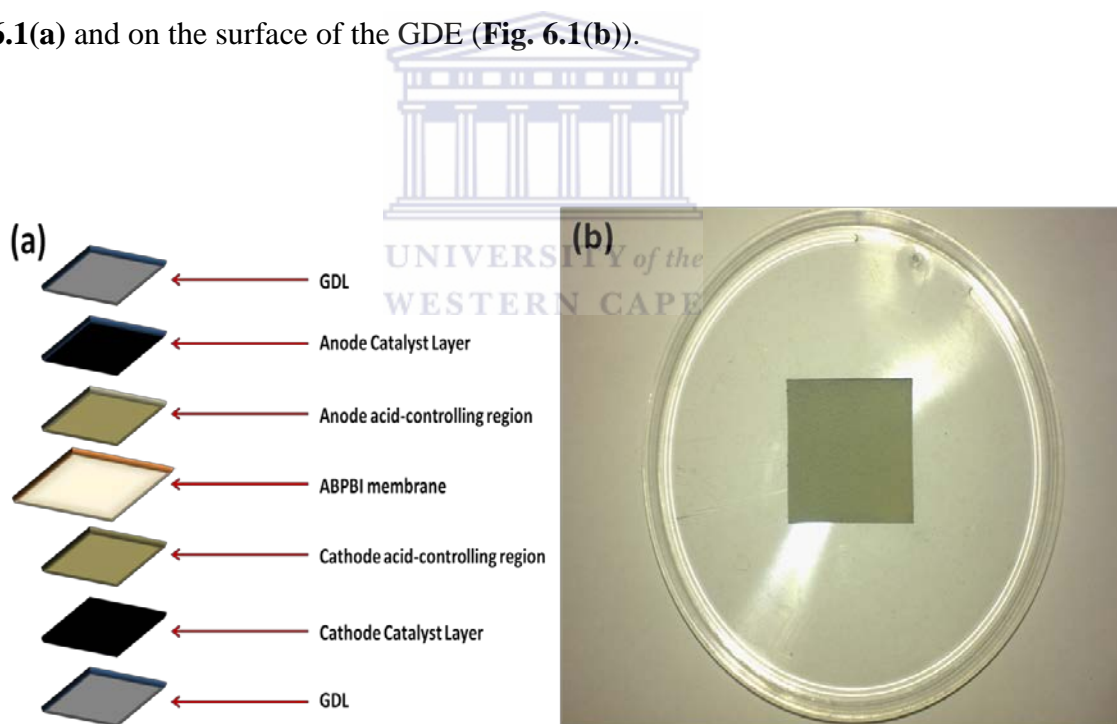


Fig. 6.1(a) Schematic diagram showing an expanded view of a MEA with acid-controlling regions and **(b)** GDE with *SiC* layer.

6.2. Results and discussion

6.2.1. Structural Evaluation of GDEs

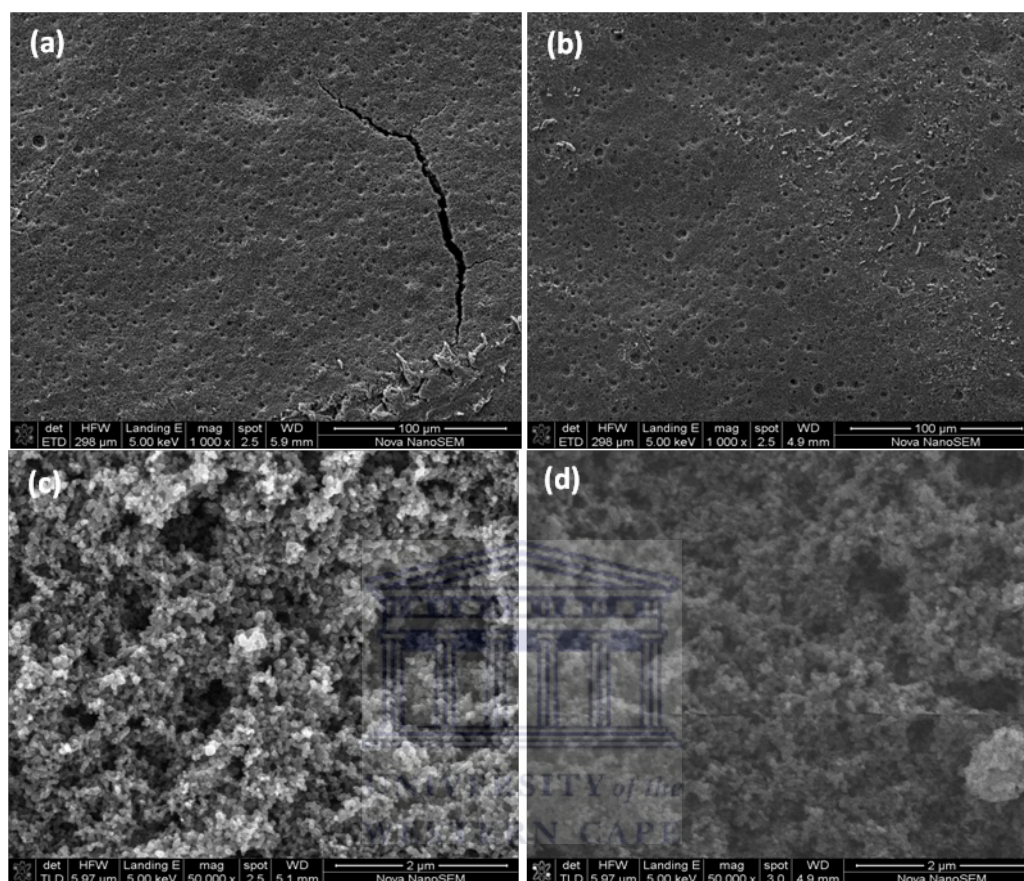


Fig. 6.2 HR-SEM surface images of (a, c) Freudenberg CX 196 GDL and (b, d) Freudenberg C4 GDL at 1,000x magnification and 50,000x magnification.

As two different commercial GDLs were used in this study, a structural evaluation of the GDLs is necessary to explain any difference in performance achieved by these GDEs. The different microstructures for the two GDLs are shown in **Fig. 6.2**. The surface micrographs taken at 1,000x magnification reveals that the GDLs are remarkably similar, with the exception that the Freudenberg CX 196 GDL (**Fig. 6.2(a)**) shows a crack of approximately 200 μm in length visible on the MPL, whereas the Freudenberg C4 GDL (**Fig. 6.2(c)**) has no cracks evident on the MPL. High magnification micrographs taken at 50,000x magnification indicates that Freudenberg

C4 GDL depicted in **Fig. 6.2(d)** appears to have a denser microstructure than the Freudenberg CX 196 GDL depicted in **Fig. 6.2(c)**, which appears to have a more porous microstructure.

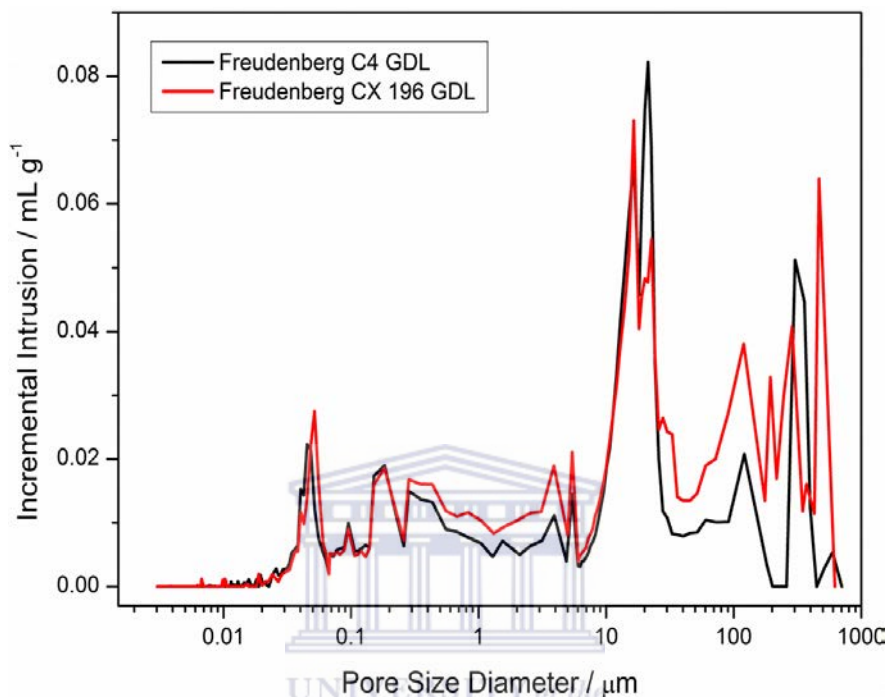


Fig. 6.3 Incremental intrusion pore-size distribution measurements of the GDLs.

Fig. 6.3 illustrates the pore-size distribution obtained for the two GDLs. It is evident that the GDLs have distinctly different pore-size distributions, with the Freudenberg CX 196 GDL exhibiting a slightly larger intrusion volume in the micropore region (0.05-0.06 μm). The mesopore (0.3-5 μm) and macropore (30-100 μm) regions show significantly larger intrusion volumes, indicating a larger number of meso- and macropores. It can also be seen that the Freudenberg CX 196 GDL has a larger intrusion volume in the >100 μm region, which can be attributed to the cracks on the GDLs surface [139]. The more porous microstructure of the Freudenberg CX 196 GDL seen in **Fig. 6.2(c)** is confirmed by the results obtained in **Fig. 6.3**. The addition of the same catalyst layer to the GDLs and its effects on the pore-size distribution is

shown in **Fig. 6.4**. A clear increase in the number of micropores in the 0.01-0.03 μm region can be observed for both GDEs, this effect is to be expected as the GDLs are largely influence the meso- and macropore region, whereas the catalyst layer largely influences the micropore region of GDEs. It is once again evident that the GDE based on the Freudenberg CX 196 GDL exhibits the better pore-size distribution across all pore regions.

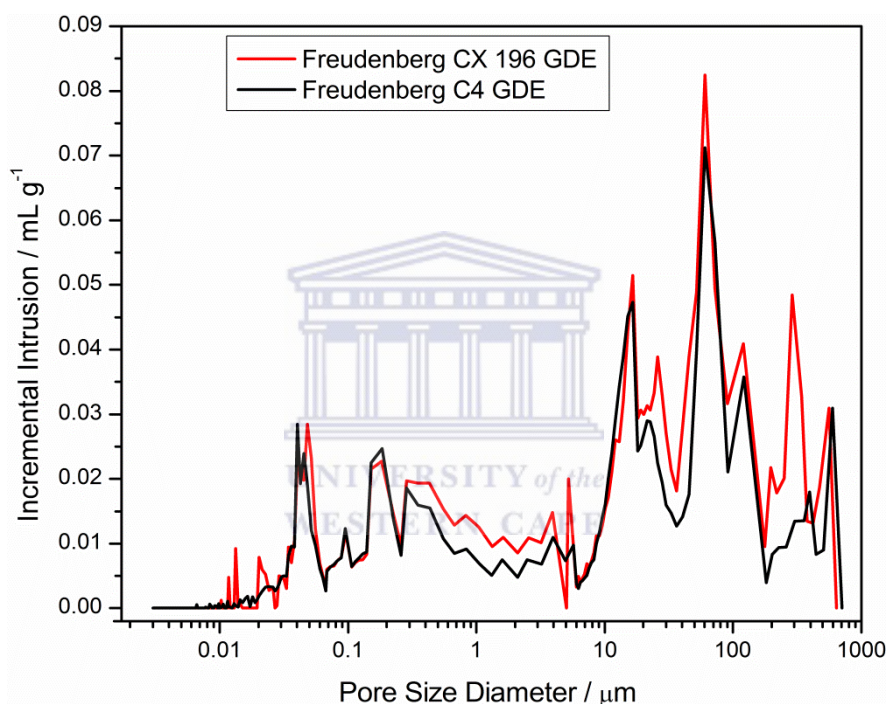


Fig. 6.4 Incremental intrusion pore-size distribution measurements of the Freudenberg GDEs.

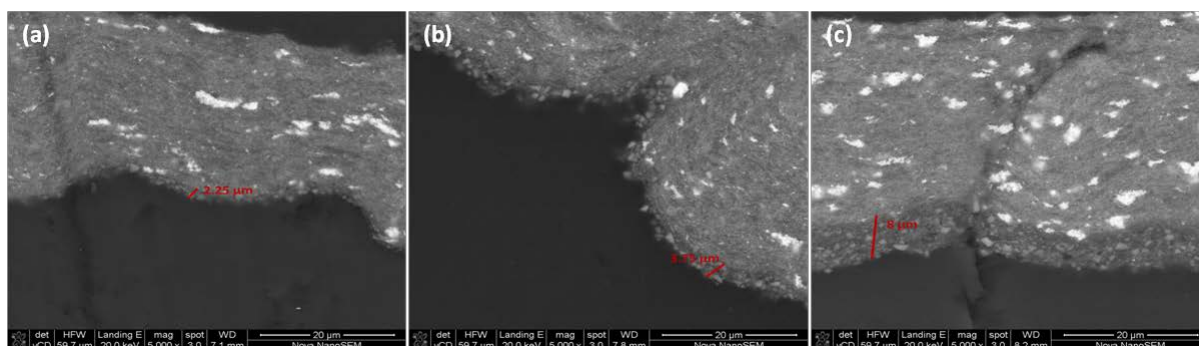


Fig. 6.5 Cross-sections of Freudenberg C4 GDEs with (a) $0.2 \text{ mg cm}^{-2} \text{ SiC}$, (b) $0.5 \text{ mg cm}^{-2} \text{ SiC}$ and (c) $1 \text{ mg cm}^{-2} \text{ SiC}$ loading.

Freudenberg C4 GDEs were sprayed with varying *SiC* loadings to determine the influence the various *SiC* loadings had on electrochemical and physical characteristics of the GDEs. Cross-sections of these GDEs are shown in **Fig. 6.5**, with the GDE orientation in the cross-section as follows; GDE situated at the top and resin at the bottom of the image. As can be seen from the images, an expected increase in the thickness of the *SiC* layer is observed as the *SiC* loading is increased, with the 0.2 mg cm⁻² *SiC* GDE (**Fig. 6.5(a)**) showing the thinnest layer of ~2.25 μm and the 1 mg cm⁻² *SiC* GDE (**Fig. 6.5(c)**) showing the thickest layer of ~8 μm. Although the 1 mg cm⁻² *SiC* GDE has a loading five times greater than the 0.2 mg cm⁻² GDE, the *SiC* layer in the 1 mg cm⁻² *SiC* GDE does not have five times the thickness, this is an expected characteristic as the manual spray technique does not produce completely uniform layers. As a result certain areas of the *SiC* layer may be thicker or thinner than others.

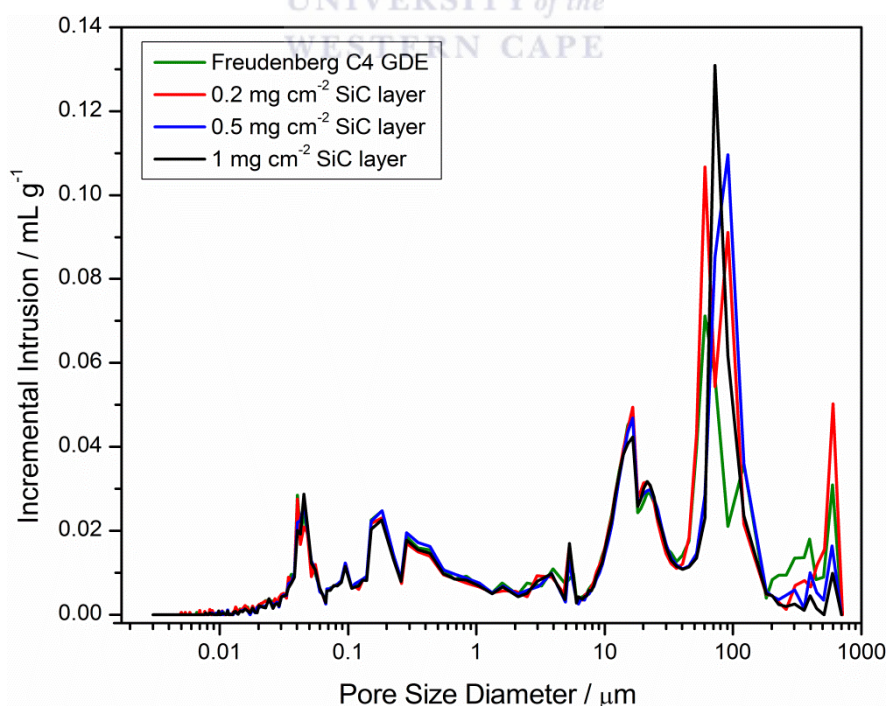


Fig. 6.6 Incremental intrusion pore-size distribution measurements of the Freudenberg C4 GDE and the Freudenberg C4 GDEs with varying *SiC* layer loadings.

The differences in pore-size distribution obtained for the various *SiC* layer loadings is depicted in **Fig. 6.6**. The observed similarity between the incremental intrusion curves in the micro- and mesopore regions indicates that the GDEs have similar porous microstructures in these regions, whereas the macropore region (50-100 μm) of the intrusion curves show more distinct differences. In this region the *SiC* GDEs exhibit a larger number of macropores than the pristine GDE, with the number of macropores generated on the surface of the *SiC* GDEs increasing as the *SiC* layer loading increases.

SEM micrographs of the surface of Freudenberg CX 196 GDEs with *SiC*-PTFE, *NbC*-PTFE, *SiC*-PBI and combination of *SiC-NbC* GDEs are shown in **Fig. 6.7**. Longer cracks are clearly visible on the surface of the 1,000x magnification image of the *SiC*-PTFE GDE (**Fig. 6.7(a)**), compared to the *NbC*-PTFE GDE (**Fig. 6.7(d)**) which shows smaller cracks on the surface. Both GDEs shows a lumpy irregular surface, with the *NbC*-PTFE GDE (**Fig. 6.7(d)**) appearing to have a more irregular surface than the *SiC*-PTFE GDE (**Fig. 6.7(a)**). It is also clear from **Fig. 6.7(b, c)** that the *SiC* particles have an altogether different shape and size to the *NbC* particles shown in **Fig. 6.7(e, f)**. The *SiC* particles appear to be larger in size, ranging from 0.8-2.25 μm with sharper edges, whereas the *NbC* particles appear to be much smaller in size, ranging from 0.4-2 μm in size with rounder edges. The *SiC* particle size exhibited here is smaller than the ~ 5 μm *SiC* particle size other researchers found in their studies [50, 140], this is likely due to the crushing of the *SiC* particles before preparing the *SiC* ink formulation so that the larger *SiC* particles would not block the nozzle of the airbrush spray gun. The *NbC* particles, however, were much finer and there was hence no need

to crush the particles and so the *NbC* particle size exhibited here is similar to that attained by Caires *et al* [140]. The larger *SiC* particles in **Fig. 6.7(c)** appear to be more loosely packed with more void spaces between crystalline particles, exhibiting a less compact network to that of the smaller *NbC* particles in **Fig. 6.7(f)**.

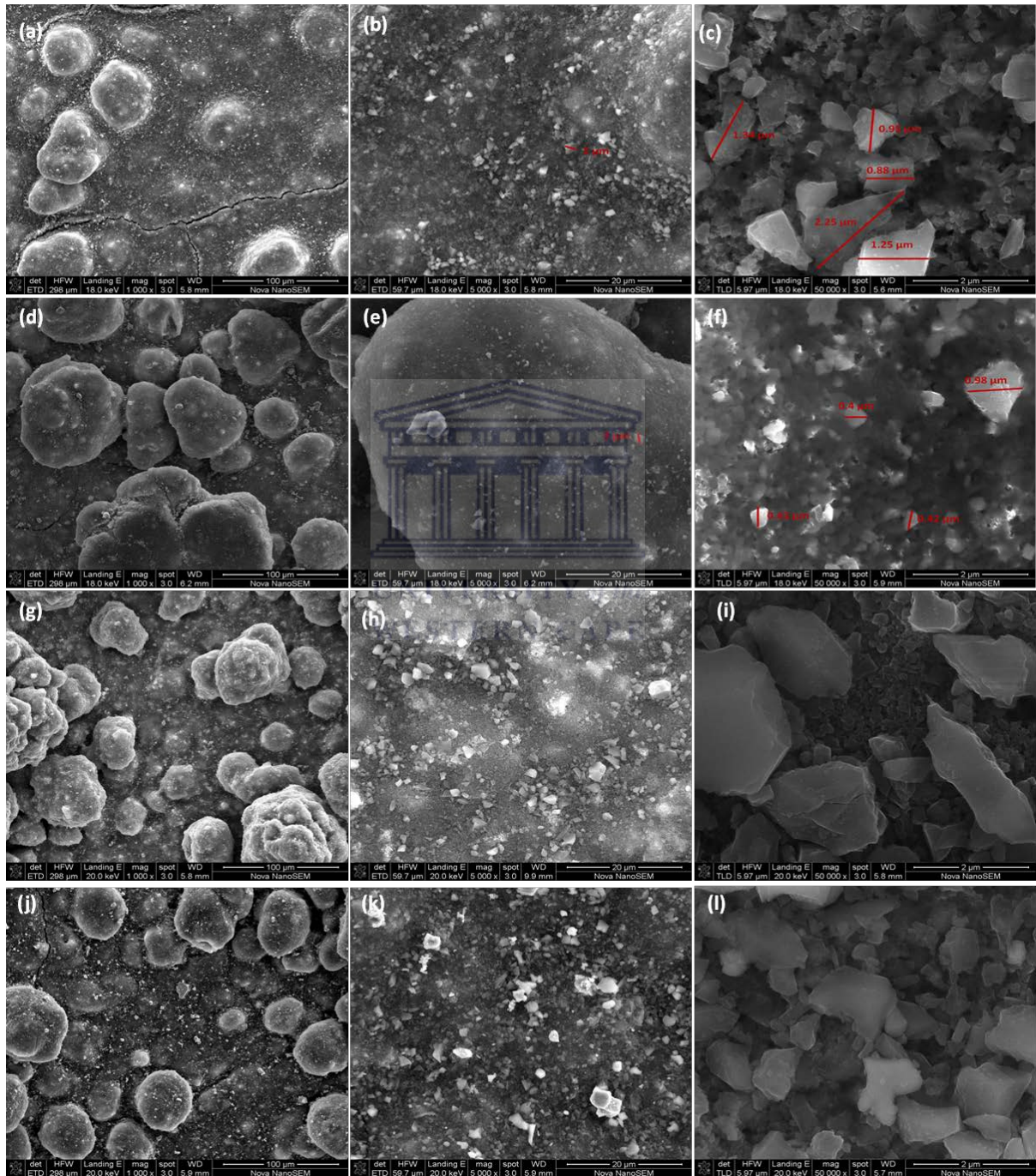


Fig. 6.7 Surface micrographs of Freudenberg CX 196 GDEs with: (a-c) 0.2 mg cm^{-2} *SiC*-PTFE layer, (d-f) 0.2 mg cm^{-2} *NbC*-PTFE layer, (g-i) 0.2 mg cm^{-2} *SiC*-PBI layer and (j-l) *SiC*-30% *NbC* layer.

A different binder to PTFE was used in the *SiC* layer to determine what, if any effect the PBI binder would have on the structural morphology of the *SiC* layer. The SEM micrographs of the *SiC*-PBI GDE are shown in **Fig. 6.7(g)-(i)**. When PBI is used as the binder in the *SiC* layer instead of PTFE, no cracks are observed on the surface of the *SiC* layer. This is most likely due to the DMAc solvent used for the *SiC*-PBI ink formulation which in the drying steps requires a longer amount of time to dry as the DMAc solvent is not as volatile as the IPA solvent. Slower DMAc solvent evaporation would lead to less cracks being formed as the *SiC* layer would require a longer drying time. The IPA solvent used in the *SiC*-PTFE ink formulation is, however, more volatile and therefore the *SiC* layer on this GDE dries faster and has more cracks.

Upon comparing the images of **Fig. 6.7(b, c)** with that of **Fig. 6.7(h, i)** it can be seen that the surface of the *SiC*-PBI GDE appears similar to the *SiC*-PTFE GDE in all other aspects. **Fig. 6.7(j)-(l)** shows the SEM images of a combination *SiC/NbC* GDE. It is hard to distinguish the *NbC* particles on the surface due to the low concentration of *NbC* in the *SiC/NbC* layer, but since *NbC* particles have round edges, we can assume that the particles with rounder edges are in fact *NbC* particles. The composite ceramic carbide layer shown in **Fig. 6.7(l)** there are less void spaces visible in the crystalline structure, due to the smaller *NbC* particles filling the voids, resulting in reduced pore sizes for the composite *SiC/NbC* GDEs.

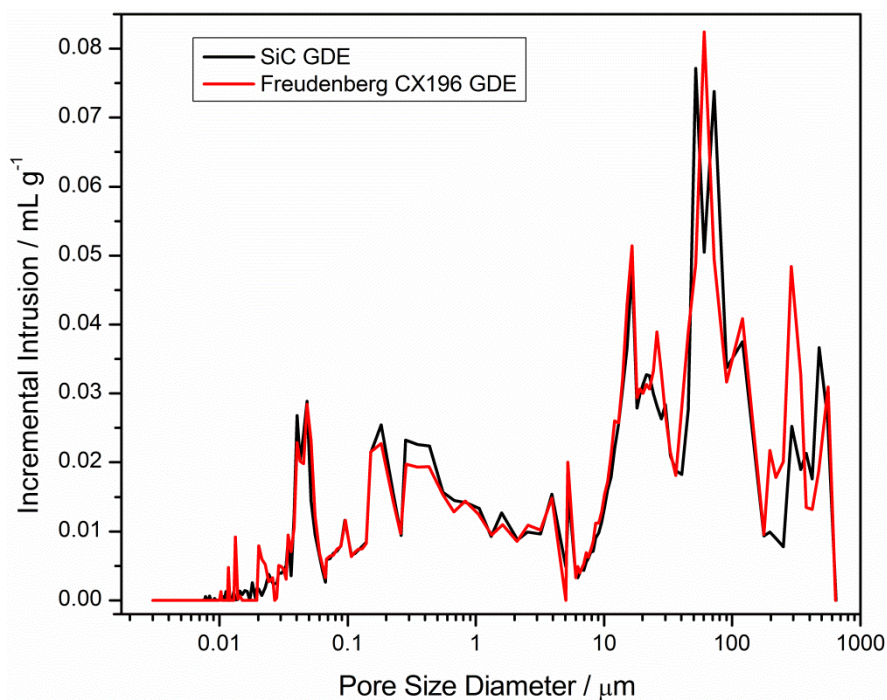


Fig. 6.8 Incremental intrusion pore-size distribution measurements comparing the unmodified Freudenberg CX 196 GDE and the *SiC*-GDE.

An illustration of the incremental intrusion pore-size distribution data for the unmodified Freudenberg CX 196 GDE and the 0.2 mg cm^{-2} *SiC* GDE is depicted in **Fig. 6.8**. The intrusion curves for the *SiC*-GDE and unmodified GDE in **Fig. 6.8** show similar intrusion volumes across the different pore regions. In order to clarify the porosimetry data obtained, the cumulative intrusion pore-size distribution measurements were examined in **Fig. 6.9**, here it can clearly be seen that although the GDEs show similar distributions across the different pore regions, the *SiC*-GDE shows reduced pores in the micro- and mesopore regions, with similar pore-size distribution occurring from the $20 \text{ }\mu\text{m}$ range. Although the quantity of smaller pores are slightly reduced, the quantity of macropores are almost the same, indicating that the addition of the *SiC* layer to the GDE is not too detrimental to the microstructure of the GDE. The porosimetry data indicated that the *SiC*-GDE had a total pore area of $29.42 \text{ m}^2 \text{ g}^{-1}$ compared to the total pore area of $32.03 \text{ m}^2 \text{ g}^{-1}$ of the Freudenberg CX

196 GDE, which confirms the slightly reduced porosity observed for the *SiC*-GDE in the intrusion curves.

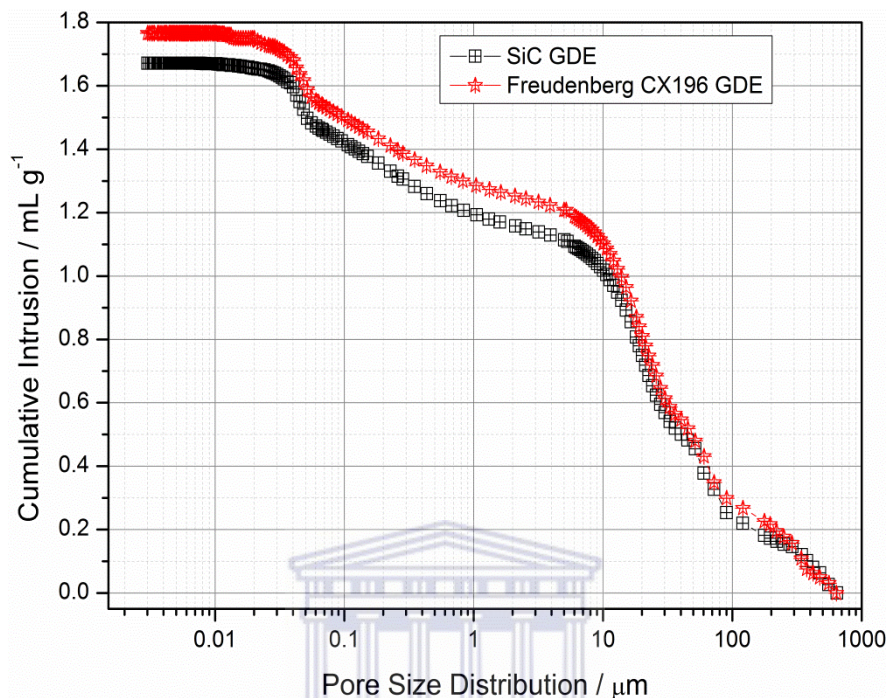


Fig. 6.9 Cumulative intrusion pore-size distribution measurements comparing the unmodified Freudenberg CX 196 GDE and the *SiC*-GDE.

The influence of different binders in the *SiC* layer on microstructure can be seen in **Fig. 6.10**. Here we clearly see that the GDEs have show some differences in porosity between 0.3-2 μm (mesopores) and between 50-70 μm (macropores), with the *SiC*-PTFE GDE showing more pores in mesopore region and less pores in the macropore region. The GDEs had a total pore area of 29.42 $\text{m}^2 \text{g}^{-1}$ and 28.49 $\text{m}^2 \text{g}^{-1}$ for the *SiC*-PTFE and the *SiC*-PBI GDEs respectively, indicating a slightly improved porous microstructure for the *SiC*-PTFE GDE when compared to the *SiC*-PBI GDE. In order to determine what effect a different ceramic carbide had on the microstructure of the GDE, the *SiC* layer was replaced with a *NbC* layer of the same loading. The incremental intrusion porosimetry data comparing the different ceramic carbide GDEs

and the unmodified Freudenberg CX 196 GDE are shown in **Fig. 6.11**. Although the addition of a *SiC* layer to the GDE had some minor influences on the porosimetry data, this was not the case for the *NbC* layer, here we see that the *NbC*-GDE has reduced pore sizes across all the pore regions. These results indicate that *NbC* greatly reduces the porous microstructure of the GDE, with a reduced total pore area of only $26.30 \text{ m}^2 \text{ g}^{-1}$.

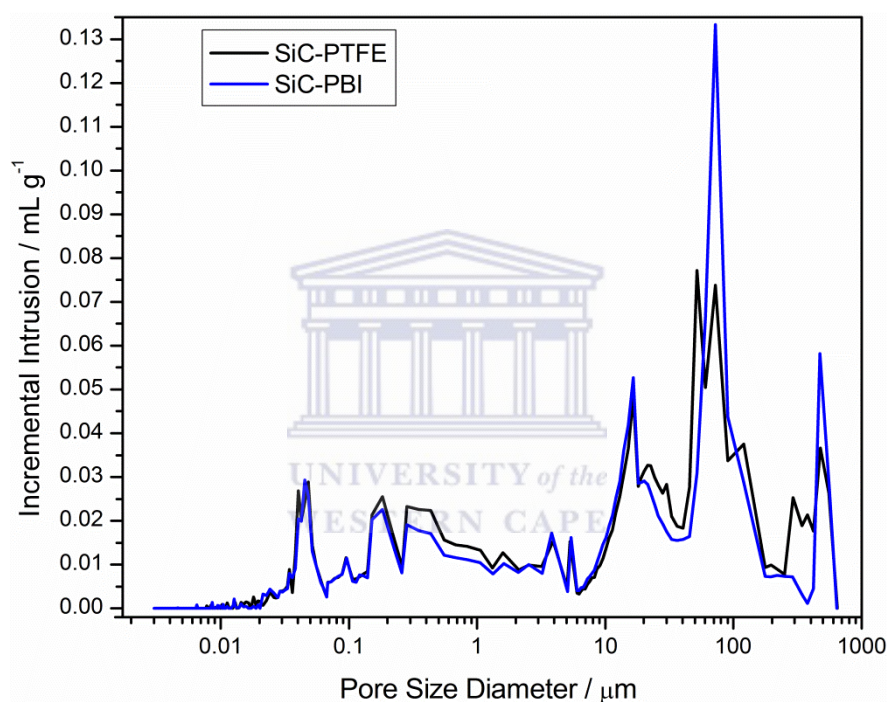


Fig. 6.10 Incremental intrusion pore-size distribution measurements for the *SiC* layers with different binders.

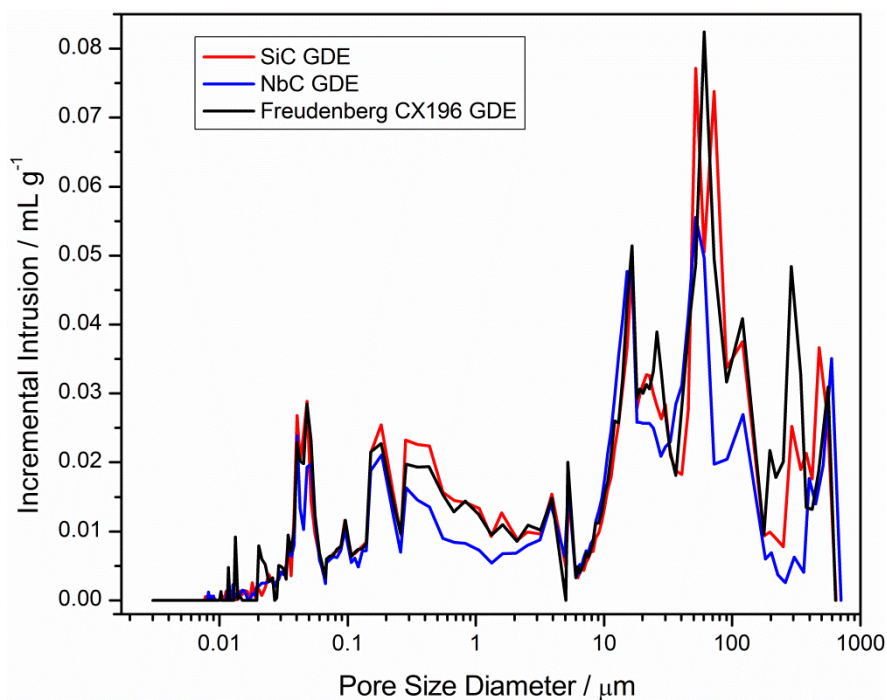


Fig. 6.11 Incremental intrusion pore-size distribution measurements comparing the unmodified Freudenberg CX 196 GDE, *SiC*-GDE and *NbC*-GDE.

Micrographs of SEM cross-section of the *NbC* GDE, *SiC*-PBI GDE and the various *SiC/NbC* GDEs are shown in Fig. 6.12. As is seen in **Fig. 6.12(a)** the *NbC* layer formed a very thin layer on the surface of the GDE, with the 0.2 mg cm^{-2} *NbC* layer having a thickness of only $1.05 \text{ }\mu\text{m}$, which is approximately half the thickness observed for the 0.2 mg cm^{-2} *SiC* layer. This observation is expected as the *NbC* particles are much smaller and denser than the *SiC* particles. The *SiC*-PBI layer shown in **Fig. 6.12(b)** demonstrates a similar thickness to that obtained for the *SiC*-PTFE layer, which is expected as the only difference in these layer are the binders used in the *SiC* layer. Although the *SiC*-PBI layer is slightly thicker at $2.38 \text{ }\mu\text{m}$, than the $2.25 \text{ }\mu\text{m}$ thickness of the *SiC*-PTFE layer, this could be due to the longer drying time needed for the DMAc solvent in the *SiC*-PBI ink formulation which could plausibly result in a more accurate thickness, as the loading is determined by weighing the sample. Composite *SiC/NbC* layers with fixed *SiC* loading of 0.2 mg cm^{-2} *SiC* and

varying concentrations of *NbC* are shown in **Fig. 6.12(c)-(g)**, the thickness of the *SiC/NbC* layers vary ranging from 2.05-2.28 μm . It is apparent that the addition of such small amounts of *NbC* to the *SiC* layer does not exert a significant influence on the thickness of these composite layers.

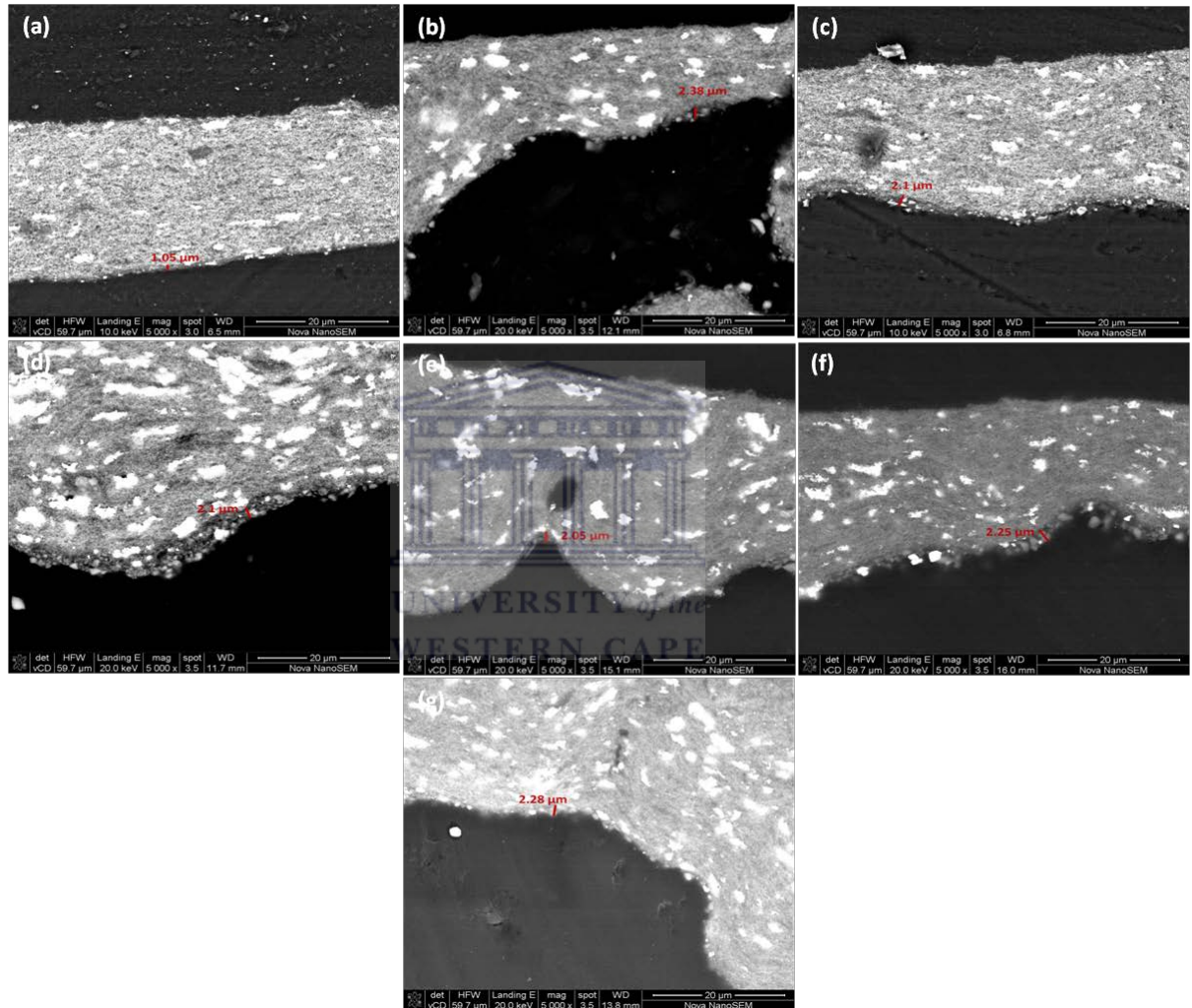


Fig. 6.12 SEM cross-sectional images of (a) 0.2 mg cm^{-2} *NbC* GDE, (b) *SiC*-PBI GDE, (c) *SiC*/10 wt.% *NbC* GDE, (d) *SiC*/30 wt.% *NbC* GDE, (e) *SiC*/50 wt.% *NbC* GDE, (f) *SiC*/70 wt.% *NbC* GDE, (g) *SiC*/90 wt.% *NbC* GDE.

Pore-size distribution measurements for the Freudenberg CX 196 GDEs with *SiC*, *NbC* and *SiC/NbC* layers are shown in **Fig. 6.13**. It is evident from the intrusion volume measurements that the *SiC*-GDE has the larger number of pores in the micro-

and mesopore region, whereas the *NbC*-GDE has the lowest quantity of pores in these regions. It is interesting to note that the all the combination *SiC/NbC* GDEs have higher intrusion volumes than the *NbC*-GDEs, hence the addition of *SiC* to the *NbC*-GDE effectively improved the porous microstructure in certain regions. Of the combination *SiC/NbC* GDEs, the *SiC/30 wt.% NbC* GDE has increased pore numbers in the micro- and mesopore region, with reduced pore numbers in the macropore region, the reduced number of macropores is beneficial as the ceramic carbide layer is better able to retain the PA electrolyte if the number of larger pores are reduced.

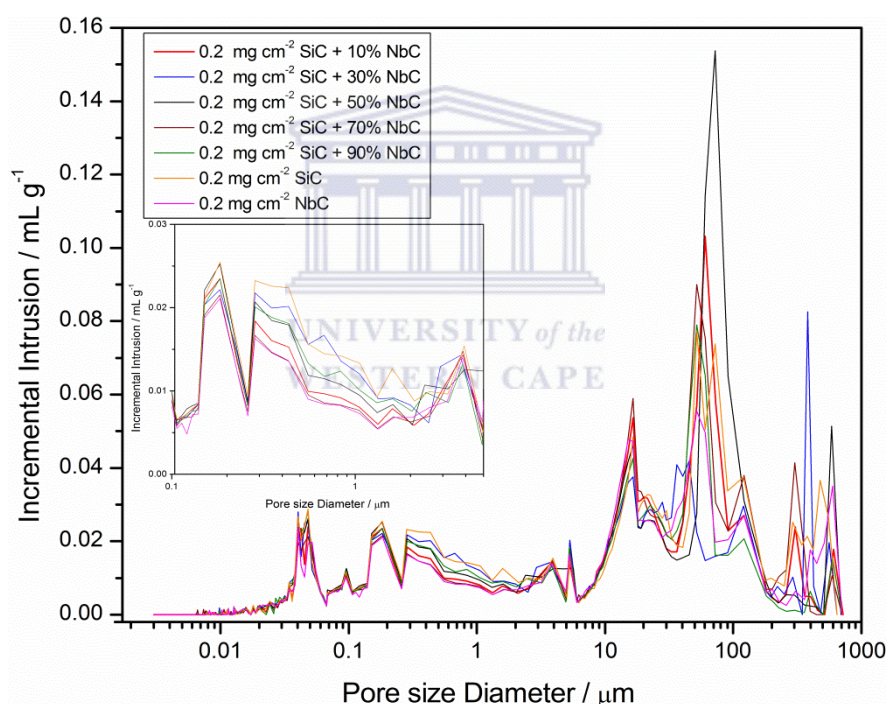


Fig. 6.13 Incremental intrusion pore-size distribution measurements comparing *SiC*-GDE, *NbC*-GDE and *SiC/NbC*-GDEs.

6.2.2 Electrochemical evaluation of MEAs

6.2.2.1 Effect of GDL on performance

Fig. 6.14 depicts the performance curves for MEAs based on Freudenberg C4 GDLs comparing a standard GDE to one which contains a *SiC* layer. A decrease in performance is observed upon addition of a *SiC* layer to the standard GDE, with the MEA of the standard GDE showing a peak power 9.6% higher compared to the *SiC* MEA. Since the GDL and catalyst layers were the same, the performance difference can be attributed from the addition of the *SiC* layer. The addition of an extra layer on top of the CL influences the ohmic resistance of the MEA, resulting in an increase in the ohmic resistance as the modified GDE now has two phosphoric acid regions through which protons have to be transported through, effectively increasing the amount of electrolyte. Analyses of the polarisation curves in **Fig. 6.14** show that the GDEs have similar electrode kinetics and similar values for the decreasing slopes in the linear region, with a small deviation occurring in the high current density region ($>1000 \text{ mA cm}^{-2}$) where the *SiC* MEA shows a sharper drop in cell voltage than the standard GDE MEA.

Table 6 - Impedance and Tafel slope characteristics of the various Freudenberg C4 *SiC* MEAs

<i>SiC</i> loading (mg cm^{-2})	Acid-doping (mg cm^{-2})	R_{Ω} ($\text{m}\Omega \text{ cm}^{-2}$)	R_{CT} ($\text{m}\Omega \text{ cm}^{-2}$)	Tafel slope (mV dec^{-1})
0	Free-acid	101.78	271.25	94
0.2	2.0	163.49	470.17	90
0.2	4.0	147.97	326.76	95
0.2	6.0	167.54	1762.64	136
0.5	4.0	156.67	387.03	101
1.0	4.0	158.52	882.64	106

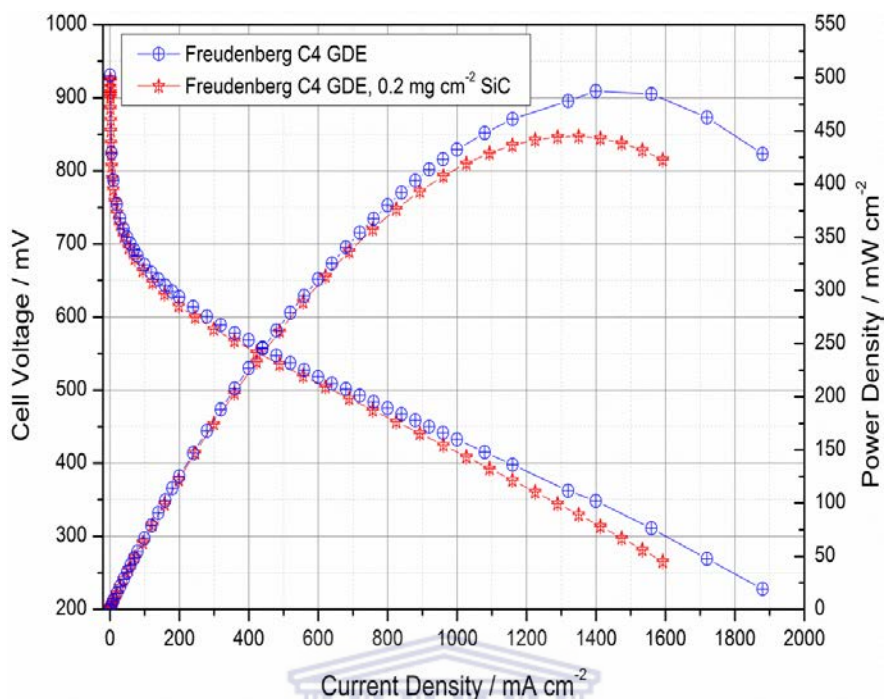


Fig. 6.14 Performance curves comparing MEAs of standard Freudenberg C4 GDE and Freudenberg C4 GDE modified with 0.2 mg cm^{-2} SiC layer doped with 4 mg cm^{-2} PA (anode and cathode).

The *in-situ* impedance curves illustrating the effect of the SiC layer on cell resistances is depicted in **Fig. 6.15**. The MEAs show significant differences in their R_{Ω} , with the MEA of the SiC GDE exhibiting a higher R_{Ω} than that of the standard GDE, this difference can be attributed to the SiC layer adding a greater contribution to the electrolyte resistance of the cell. Addition of the SiC layer also increased the R_{CT} , which is to be expected as the MEA now has an extra layer through which the protons have to diffuse through. The data represented in **Table 6** shows the electrochemical resistances and *Tafel slopes* values obtained for the MEAs. Although the MEAs show distinct differences in their ohmic and charge transfer resistances, the *Tafel slopes* values obtained from the *Tafel* plot shown in **Fig. 6.16** are remarkably similar, with the standard MEA having a *Tafel slope* value of 94 mV dec^{-1} compared to 95 mV dec^{-1}

¹ for the *SiC* MEA. These *Tafel slope* values indicate that although the two GDEs have different structures, they share the same electro-oxidation mechanism.

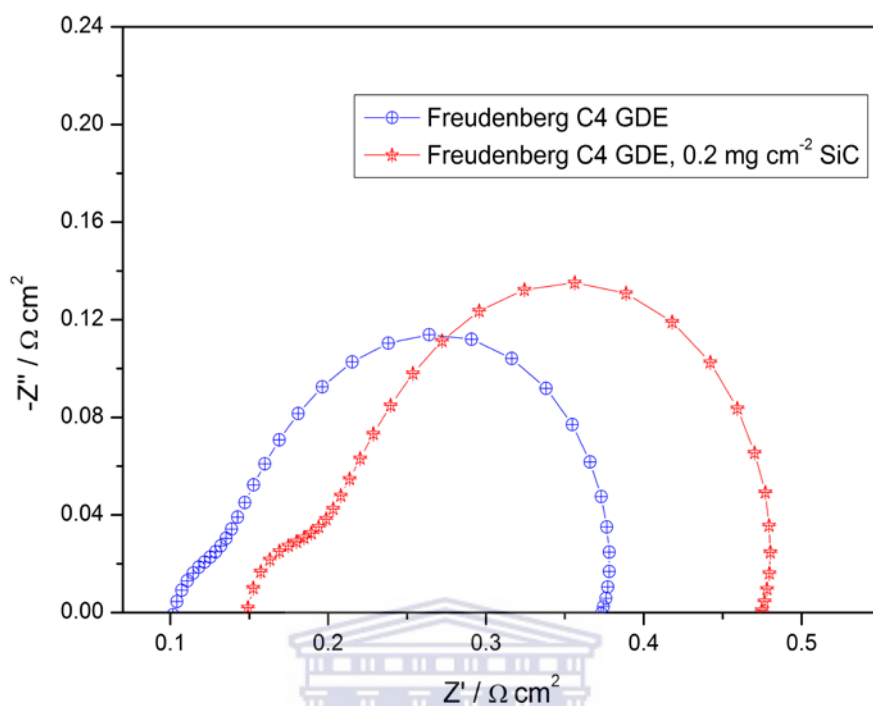


Fig. 6.15 *In-situ* impedance curves illustrating the effect of *SiC* layer on cell resistances, at a cell voltage of +0.6 V.

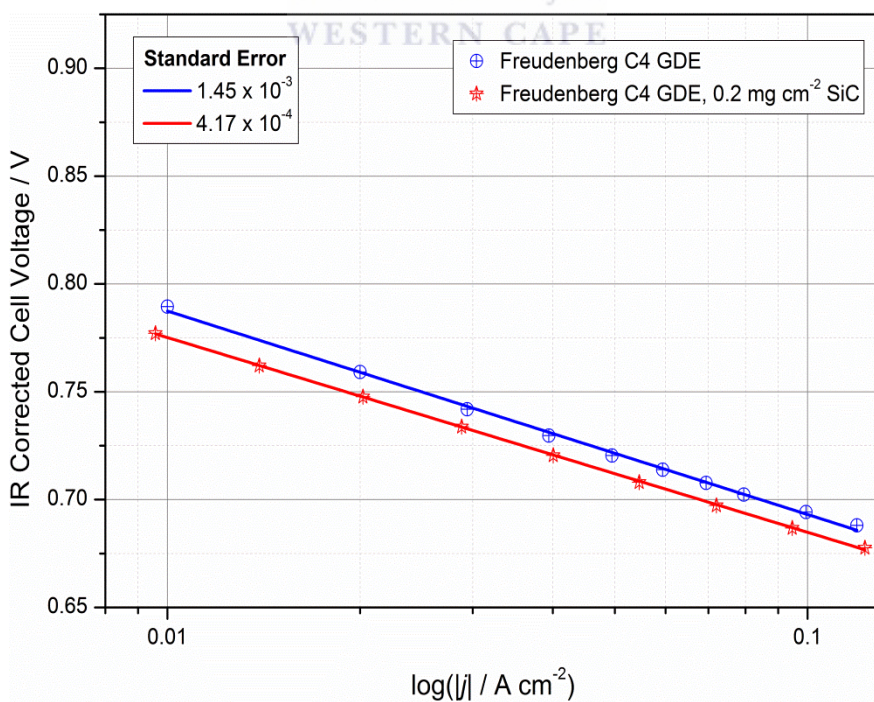


Fig. 6.16 *Tafel* plots for the ORR of the GDEs with differing structures.

6.2.2.2 Influence of SiC loading on performance of Freudenberg C4 GDEs

Fig. 6.17 shows the polarisation and power density curves for the Freudenberg C4 MEAs with various SiC layer contents. At low current densities the polarisation curves show similar cell voltages, indicating that the electrode kinetics is not influenced by the loading of the SiC layer. The medium current density regions of the polarisation curves, however, do not share similar characteristics, with pronounced variations of the slopes of the curves with the SiC loading, indicating that the ohmic kinetics of these GDEs are significantly influenced by SiC loading. The high current density regions of the polarisation curves show no sharp drops indicating that the GDEs possess no significant mass transport limitations. It is evident from the performance curves that the MEA performance increases as SiC layer loading decreases, with the MEA of the 0.2 mg cm^{-2} SiC GDE showing the highest performance when compared to the 0.5 mg cm^{-2} and 1 mg cm^{-2} SiC GDE MEAs. The 0.2 mg cm^{-2} SiC MEA achieved a peak power of 445 mW cm^{-2} at a cell voltage of $+330 \text{ mV}$, which is an increase of approximately 18.3% over the 0.5 mg cm^{-2} SiC MEA and an increase of 131% over the 1 mg cm^{-2} SiC MEA.

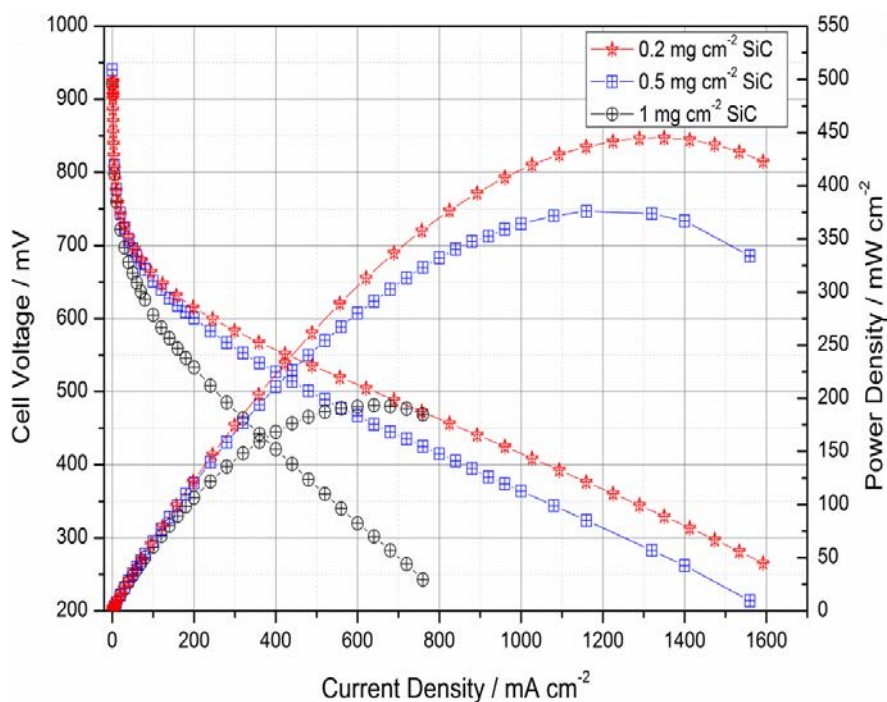


Fig. 6.17 Performance curves comparing Freudenberg C4 GDEs with various SiC layer contents and 4 mg cm^{-2} PA loading (anode and cathode).

The *in-situ* impedance curves for the GDEs with various SiC loadings are shown in **Fig. 6.18**. The MEAs all have similar high frequency x -axis intercepts indicating that the MEAs have similar R_{Ω} values, with significant variations occurring with the R_{CT} , as can be seen from the diameter of the arc. These curves show that the charge transfer resistance increases as the SiC loading increases, indicating that the resistance to proton conductivity increases as the thickness of the SiC layer increases. The *Tafel* plots for these GDEs are depicted in **Fig. 6.19**, with the values of 95-106 mV dec^{-1} obtained for *Tafel slopes*. Whereas the higher loading SiC GDEs (0.5 and 1 mg cm^{-2}) exhibit similar high values for their *Tafel slopes*, the 0.2 mg cm^{-2} SiC loading GDEs shows the lowest value for the *Tafel slope* (95 mV dec^{-1}), indicating that this GDE has the fastest reaction kinetics.

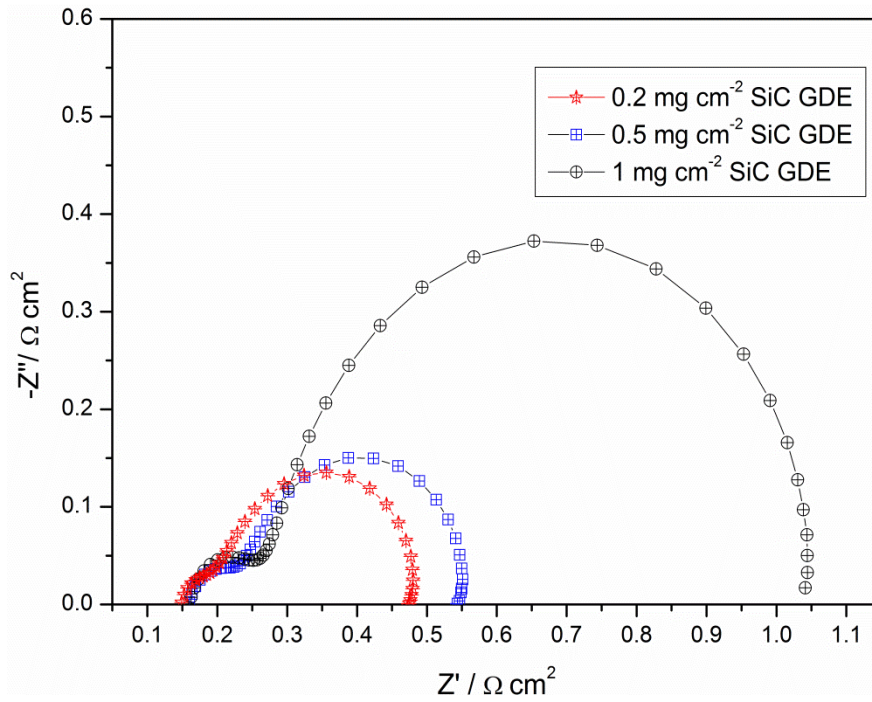


Fig. 6.18 *In-situ* impedance curves comparing Freudenberg C4 GDEs with various SiC layer loadings, doped with 4 mg cm⁻² PA, at a cell voltage of +0.6V.

Based on the results obtained in Fig. 6.17 and Fig. 6.18, the 0.2 mg cm⁻² SiC loading GDE was chosen for optimisation of the H₃PO₄ loading in the SiC layer. The performance curves for the 0.2 mg cm⁻² SiC MEAs with various acid doping levels are shown in Fig. 6.20.

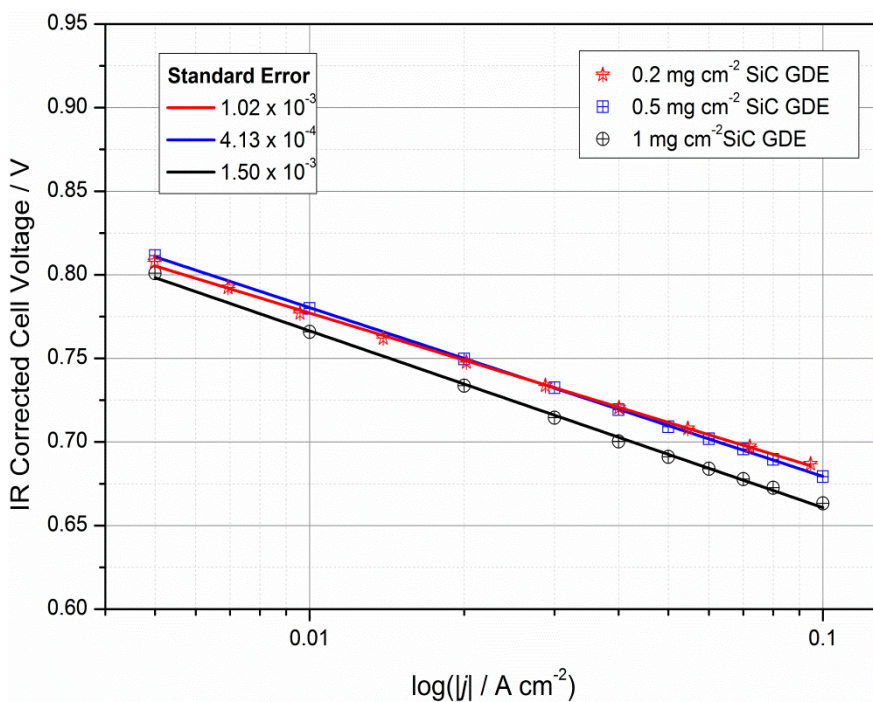


Fig. 6.19 Tafel plots for the ORR of the GDEs with different SiC layer loadings.

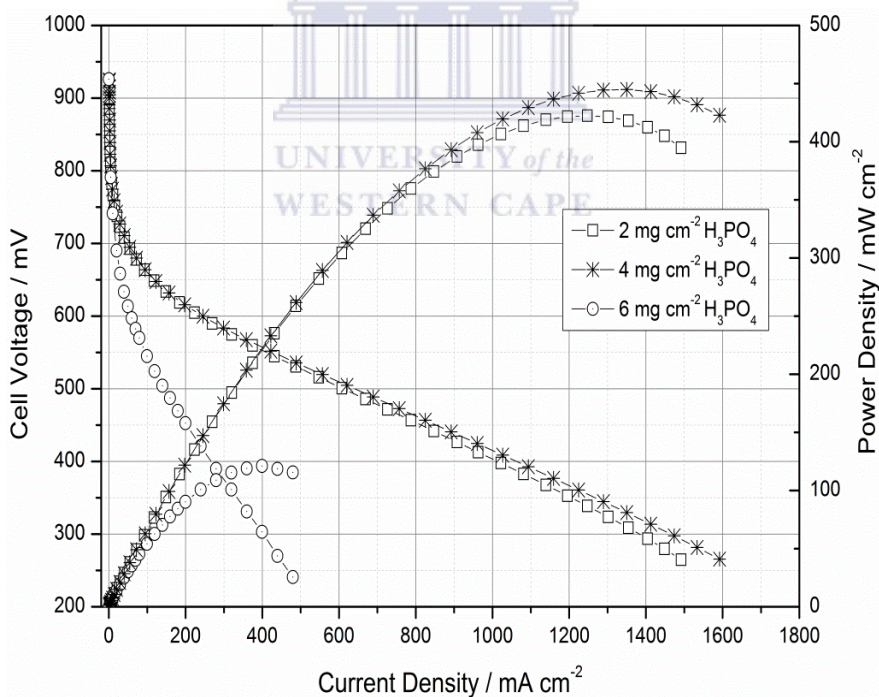


Fig. 6.20 Performance curves comparing MEAs of Freudenberg C4 GDEs with 0.2 mg cm^{-2} SiC layer content and various PA doping levels (anode and cathode).

As seen in Fig. 6.20, the GDEs doped with 2 and 4 mg cm^{-2} PA result in higher performance than that achieved by the GDE doped with 6 mg cm^{-2} PA, with the 4 mg

cm⁻² PA doped GDE achieving the maximum power density of 444 mW cm⁻² at a cell voltage of +345 mV, and the 2 mg cm⁻² PA doped GDE showing only a minor difference with a peak power of 422 mW cm⁻² achieved at a cell voltage of +339 mV. The 6 mg cm⁻² PA doped GDE, however, showed extremely poor performance when compared to the 2 and 4 mg cm⁻² PA doped GDEs, achieving a peak power of only 121 mW cm⁻² at a cell voltage of +303 mV. Since the GDEs all have identical SiC layers, the poor performance exhibited by the 6 mg cm⁻² PA doped GDE is likely due to excessive phosphoric acid forced into the electrodes pores, thereby blocking the pores in the GDE resulting in a decrease in the TPB area at the electrode causing a severe decrease in cell performance. **Fig. 6.21** shows the *in-situ* impedance spectra obtained at + 0.6V for the 0.2 mg cm⁻² SiC loading Freudenberg4 GDEs with various PA doping levels. The curves all show similar ohmic resistances, with the 2 mg cm⁻² and 4 mg cm⁻² PA doped GDEs showing similar charge transfer resistances, the 6 mg cm⁻² PA doped GDE, however, shows a large difference in charge transfer resistance compared to the 2 and 4 mg cm⁻² PA doped GDEs. These results correspond to the cell performances observed in **Fig. 6.20**. The values for the *Tafel slopes* of the different PA loading MEAs are indicated in **Table 6**, with the *Tafel* plots depicted in **Fig. 6.22**. The values obtained for the *Tafel slopes* of these MEAs indicate that the SiC GDEs doped with 2 and 4 mg cm⁻² PA (90 and 95 mV dec⁻¹ respectively) have similar reaction kinetics, whereas the SiC GDE doped with 6 mg cm⁻² PA has the slowest reaction kinetics with a *Tafel slope* of 136 mV dec⁻¹. This high *Tafel slope* value obtained for the SiC GDE doped with 6 mg cm⁻² can be attributed to the high acid loading which blocks the GDEs pores effectively decreasing the TPB area.

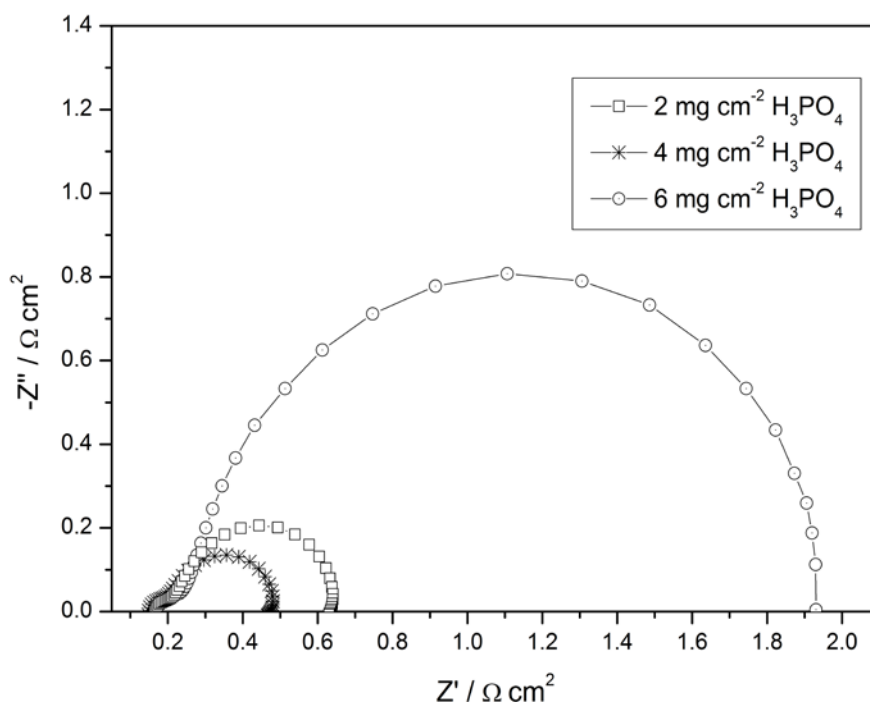


Fig. 6.21 In-situ impedance curves illustrating the effect of PA doping content on Freudenberg C4 GDEs with 0.2 mg cm^{-2} SiC layer, at a cell voltage of +0.6V.

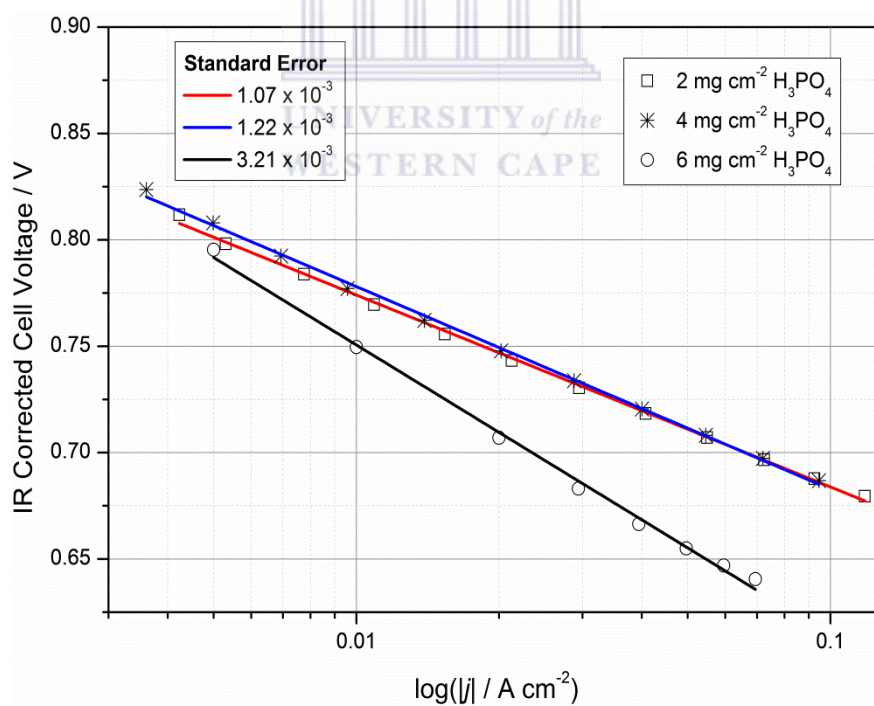


Fig. 6.22 Tafel plots for the ORR of the Freudenberg C4 0.2 mg cm^{-2} GDEs with varying acid doping levels.

6.2.2.3 Single cell performance of Freudenberg CX 196 based MEAs

The performance curves of the standard Freudenberg CX 196 GDE vs 0.2 mg cm^{-2} SiC Freudenberg CX 196 GDE doped with 2 mg cm^{-2} PA is shown in **Fig. 6.23**. Looking at the performance curves in **Fig. 6.23**, the MEA of the unmodified GDE achieves a higher performance than the MEA of the 0.2 mg cm^{-2} SiC GDE, with the unmodified GDE reaching peak power at 518 mW cm^{-2} at a cell voltage of +370 mV, whereas the MEA of the SiC GDE only reaches a peak power of 475 mW cm^{-2} at a cell voltage of +340 mV. The MEA of the SiC GDE suffers a performance loss of ~9% when compared to the MEA of the unmodified GDE. The GDEs show similar electrode kinetics in the low current density region, with only slight differences occurring in the medium and high current density region of the polarisation curve.

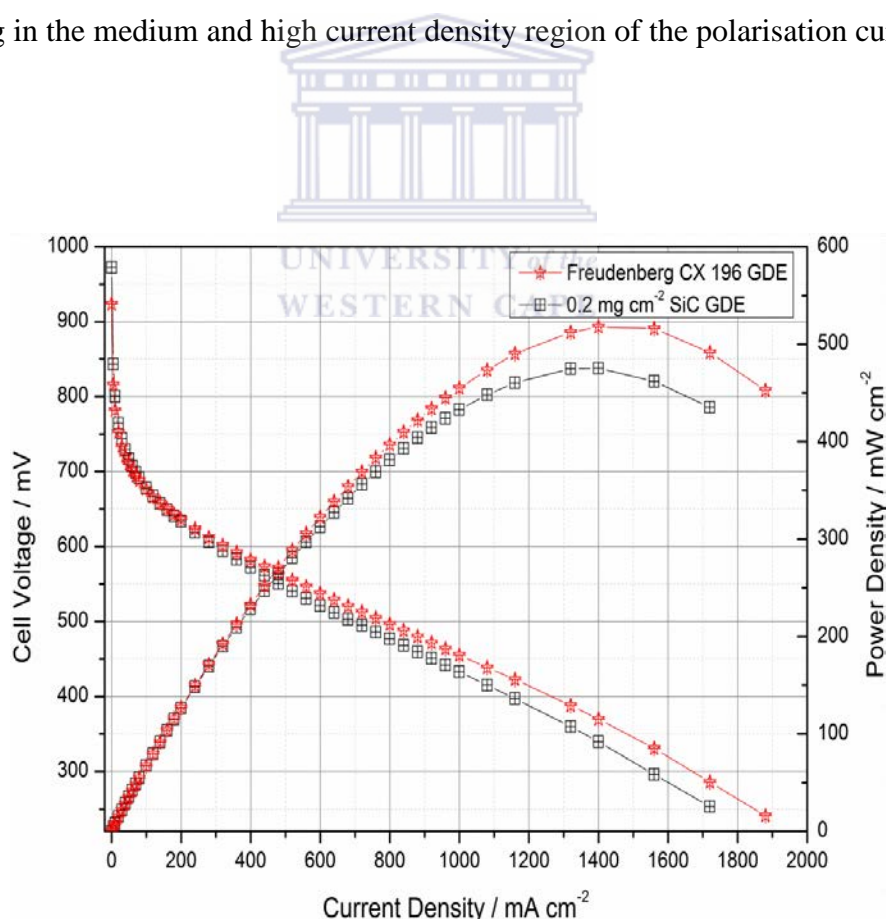


Fig. 6.23 Performance curves comparing MEAs of Freudenberg CX 196 GDE with Freudenberg CX 196 GDE with 0.2 mg cm^{-2} SiC layer doped with 2 mg cm^{-2} PA (anode and cathode).

Table 7 - Impedance and Tafel slope characteristics of the standard MEA vs the SiC

MEA			
GDE	R_{Ω} (m Ω cm $^{-2}$)	R_{CT} (m Ω cm $^{-2}$)	Tafel slope (mV dec $^{-1}$)
Freudenberg CX 196	87.25	265.75	87
0.2 mg cm $^{-2}$ SiC	146.35	280.90	101

Fig. 6.24 shows the *in-situ* impedance curves for the standard MEA and the 0.2 mg cm $^{-2}$ SiC MEA, at a cell voltage of +0.6V. The results from the impedance spectra as well as the *Tafel slopes* for the MEAs in **Fig. 6.23** are shown in **Table 7**.

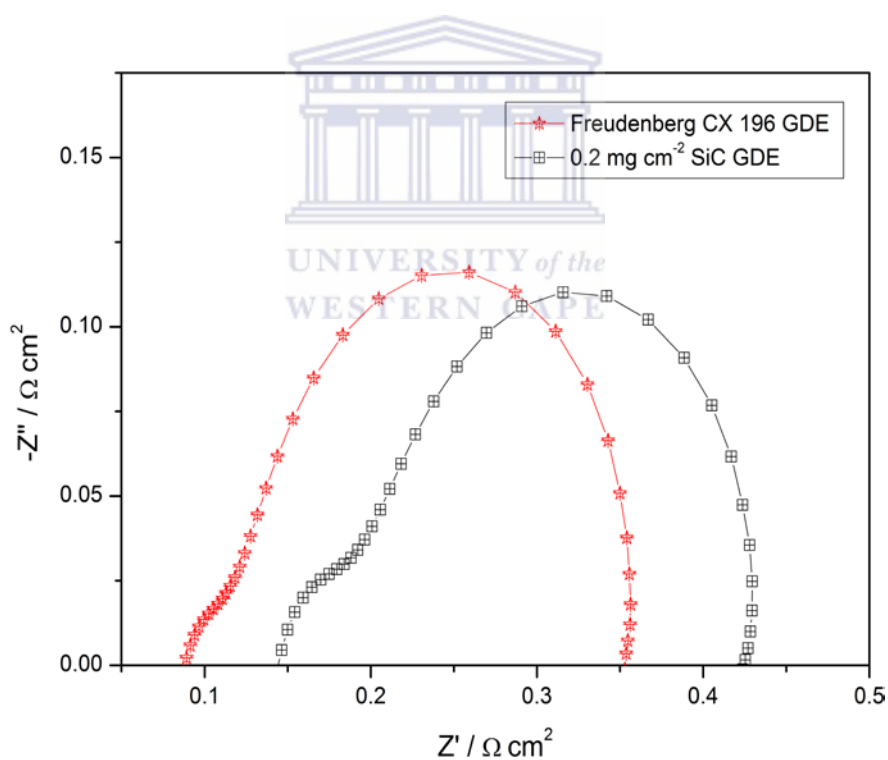


Fig. 6.24 In-situ impedance curves comparing MEA of a standard Freudenberg CX 196 GDE versus MEA of Freudenberg CX 196 GDE with 0.2 mg cm $^{-2}$ SiC and 40% PTFE layer, doped with 2 mg cm $^{-2}$ PA (anode and cathode), at a cell voltage of +0.6 V.

These MEAs show significantly different ohmic resistances, with the standard MEA showing a R_{Ω} of only 87.25 m Ω cm $^{-2}$ when compared to the 0.2 mg cm $^{-2}$ SiC MEA

which showed a R_{Ω} of $146.35 \text{ m}\Omega \text{ cm}^{-2}$. The ohmic resistance represents the total ohmic resistance of the cell, which is composed of the contact resistance between the cell components, ohmic resistance of the membrane, catalyst layer, gas diffusion layer and bipolar plates [86]. Since the only difference between these MEAs is the *SiC* layer, we can conclude that the addition of the *SiC* layer contributes to the contact resistance of the cell which in turn causes an increase in the total ohmic resistance. In addition to the different ohmic resistances observed, a difference in the charge transfer resistance can also be seen. In this case the standard MEA shows the lower R_{CT} of only $265.75 \text{ m}\Omega \text{ cm}^2$ when compared to the slightly higher R_{CT} of $280.90 \text{ m}\Omega \text{ cm}^2$ for the *SiC* MEA. This higher charge transfer resistance for the *SiC* MEA results in the lower performance observed in **Fig. 6.23**. The *Tafel slope* values shown in **Table 7** were obtained by linear fitting of the experimental data depicted in **Fig. 6.25**, the values of 90 mV dec^{-1} obtained for the standard MEA and 97 mV dec^{-1} for the *SiC* MEA gives us an indication of the ORR kinetics, since the kinetic overpotential of the cathode provides the larger contribution to the overpotential, due to the low solubility of oxygen in PA, the data shows that the standard MEA has a significantly lower *Tafel slope* when compared to the *SiC* MEA indicating that the standard MEA has better ORR kinetics than the *SiC* MEA.

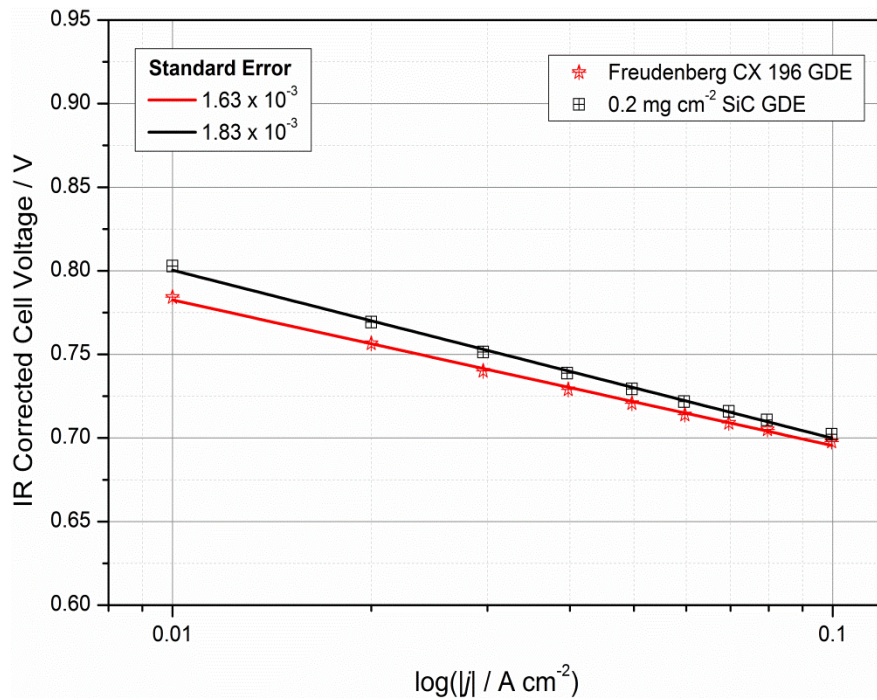


Fig. 6.25 Tafel plots for the ORR of the Freudenberg CX 196 GDEs with different GDE structures.

The influence of varying acid doping levels on the performance of the Freudenberg CX 196 GDE with 0.2 mg cm² SiC layer is depicted in **Fig. 6.26**. The performance curves indicate that the performance of the MEAs increases inversely with acid doping concentration, with the MEA doped with 2 mg cm⁻² PA achieving peak power density of 475 mW cm⁻² at a cell voltage of +340 mV. This MEA shows the lowest voltage drop across all current density regions, indicating that this GDE has the better electrode kinetics and lower ohmic and mass transport losses. These curves also illustrate that too much acid in the SiC layer is clearly detrimental to high cell performance, with the lowest peak power of 261 mW cm⁻² achieved by the MEA doped with 4 mg cm⁻² PA at a cell voltage of +344 mV. The 2 mg cm⁻² PA doped MEA shows a ~82% improvement in performance when compared to the 4 mg cm⁻² PA doped MEA. Acid doping of the 0.2 mg cm⁻² SiC GDE clearly has an optimum value of 2 mg cm⁻² PA in the SiC layer.

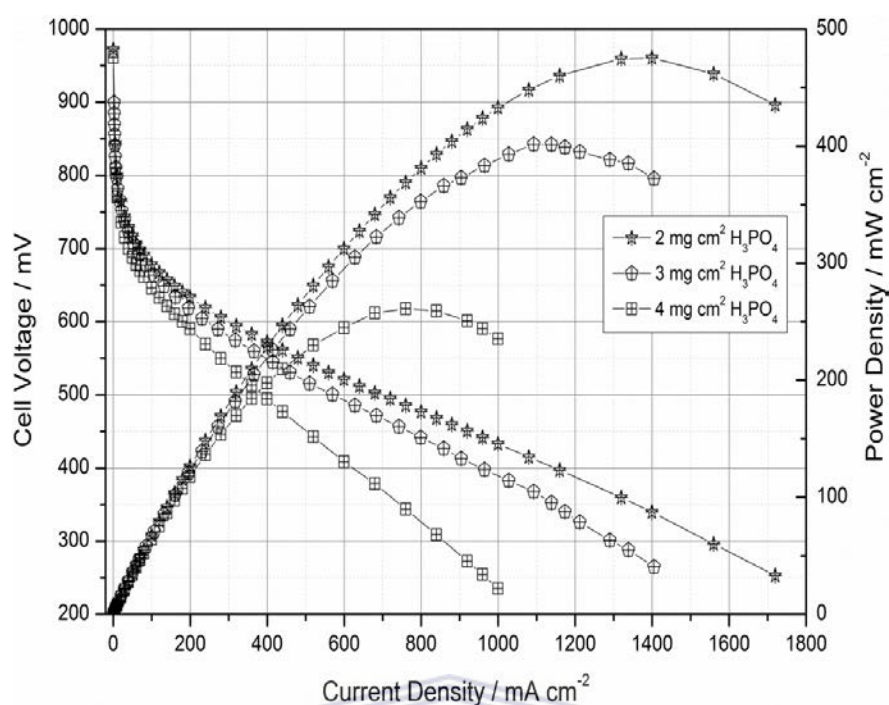


Fig. 6.26 Performance curves for MEAs comparing Freudenberg CX 196 GDEs with 0.2 mg cm^{-2} SiC layer content and various PA doping levels (anode and cathode).

Fig. 6.27 depicts the *in-situ* impedance spectra obtained for the Freudenberg CX 196 MEA with 0.2 mg cm^{-2} SiC layer and various PA doping concentrations. Analysis of the impedance spectra shows that the R_{CT} values for the different MEAs increases as the PA electrolyte concentration increases, confirming the results obtained in **Fig. 6.26** that too much PA causes electrolyte flooding into the GDE, causing a decrease in the TPB area, thereby resulting in an increased resistance to proton transport [141]. Although the 3 mg cm^{-2} and 4 mg cm^{-2} PA doped MEAs show similar R_Q values, this characteristic is not observed for the 2 mg cm^{-2} PA doped MEA. Since the only difference in the MEAs are the variations in PA doping, an obvious conclusion would be that the 2 mg cm^{-2} PA concentration in the SiC layer causes an increase in the R_Q of the MEA, however, this trend does not extend to the other MEAs, hence, an alternative more plausible cause for the increase in the R_Q exists. Although we assume

that ABPBI membrane should achieve similar doping levels if the exact same electrolyte doping level is followed, this is not always the case as minor differences in homogeneity can cause differences in electrolyte doping levels which in turn would influence the R_{Ω} . The electrochemical resistances and *Tafel slope* data are shown in **Table 8**, with the Tafel plots illustrated in **Fig. 6.28**. Comparing the *Tafel slope* values obtained from linear fitting of the experimental data, the similar values obtained indicate that these electrodes are dominated by the same kinetic processes and that the MEA composed of the *SiC* GDE doped with 2 mg cm^{-2} PA has better ORR kinetics when compared to the other MEAs with the differing PA doping concentrations.

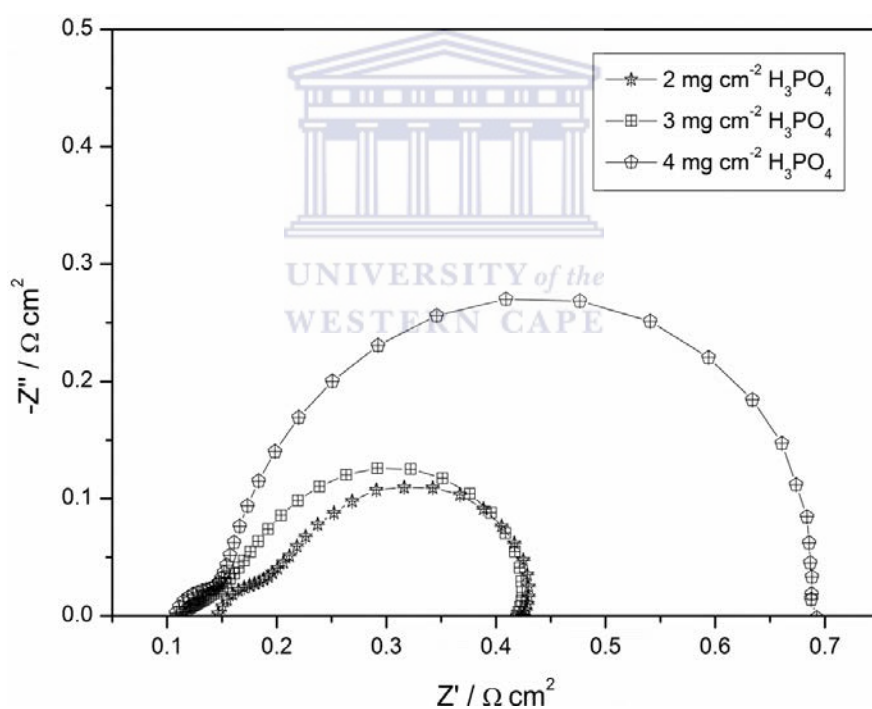


Fig. 6.27 *In-situ* impedance curves for MEAs comprised of Freudenberg CX 196 GDEs with 0.2 mg cm^{-2} *SiC* and 40% PTFE layer, with various PA doping levels (anode and cathode), at a cell voltage of + 0.6 V.

Table 8 - Impedance and *Tafel slope* characteristics of the Freudenberg CX 196 MEAs with various PA doping levels.

<i>SiC</i> layer PA doping concentration	R_{Ω} (m Ω cm $^{-2}$)	R_{CT} (m Ω cm $^{-2}$)	Tafel slope (mV dec $^{-1}$)
2 mg cm $^{-2}$	142.86	280.80	97
3 mg cm $^{-2}$	105.58	306.41	99
4 mg cm $^{-2}$	114.07	586.92	101

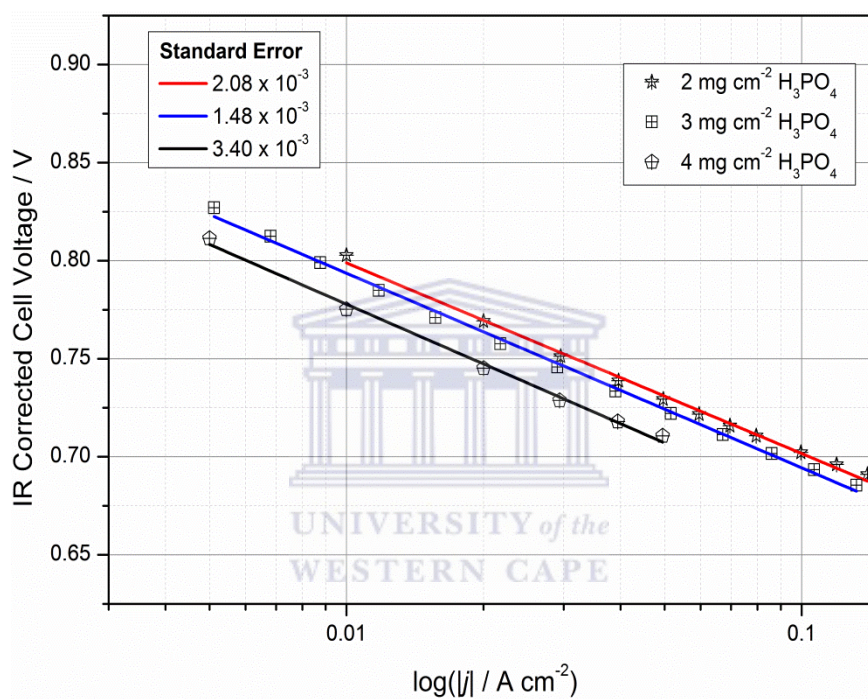


Fig. 6.28 *Tafel* plots for the ORR of the Freudenberg CX 196 0.2 mg cm $^{-2}$ SiC GDEs with different H $_3$ PO $_4$ loadings.

6.2.2.3 Influence of PBI in SiC layer

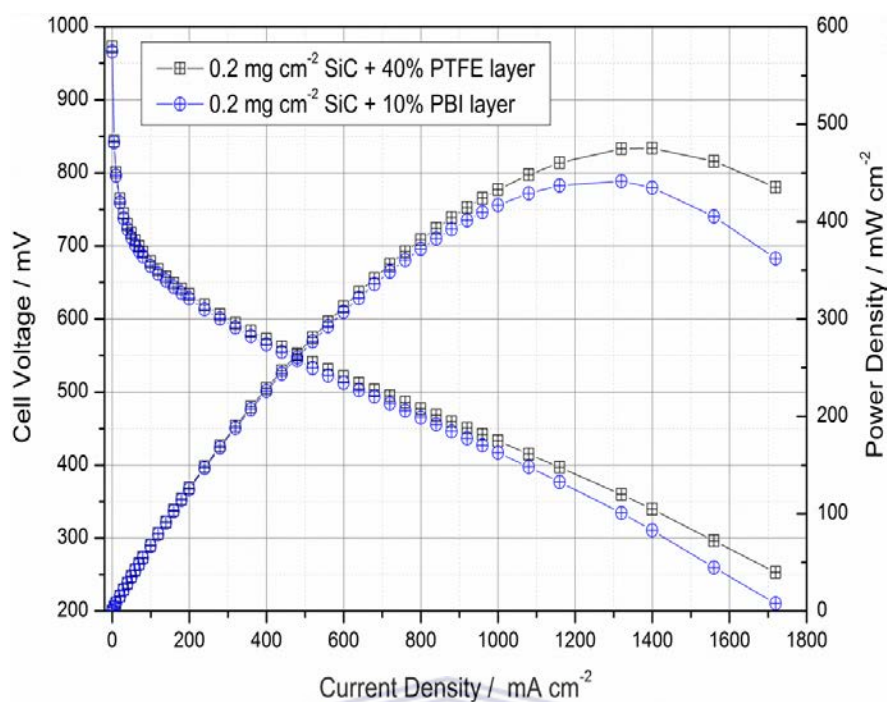


Fig. 6.29 Performance curves for MEAs comparing Freudenberg CX 196 GDEs with 0.2 mg cm^{-2} SiC layer content and various binders in the SiC layer and 2 mg cm^{-2} PA doping (anode and cathode).

The performance plot depicted in **Fig. 6.29** illustrates the influence of different polymers in the SiC layer. The polarisation curves for both the SiC-PTFE and SiC-PBI layer MEAs show distinct similarities in the low and medium current density regions, with the MEA of the SiC-PTFE GDE showing a slightly lower decreasing slope than the MEA of the SiC-PBI MEA, indicating that this MEA has slightly better ohmic resistance properties. Both MEAs exhibit no significant drop in cell voltage in the high current density region indicating that these MEAs are not hindered by mass transport limitations. The *in-situ* impedance spectra for these MEAs are shown in **Fig. 6.30**, with the electrochemical characteristics including *Tafel slope* values are shown in **Table 9**. Analysis of the *in-situ* impedance curves shows that the MEA of the SiC-PTFE GDE has a significantly lower R_{CT} when compared to the MEA of the SiC-PBI GDE, indicating that although PBI is a conductive polymer, it does not prove

beneficial in the *SiC* layer. *Tafel slope* values obtained from the *Tafel* plots in **Fig. 6.31** indicate that the *SiC*-PTFE MEA possesses slightly better ORR kinetics than the *SiC*-PBI MEA. Replacing PTFE with PBI in the *SiC* layer, hence, does not have the intended effect of improving the performance and conductivity of the *SiC* layer but in fact negatively impacts the cell performance and the conductivity.

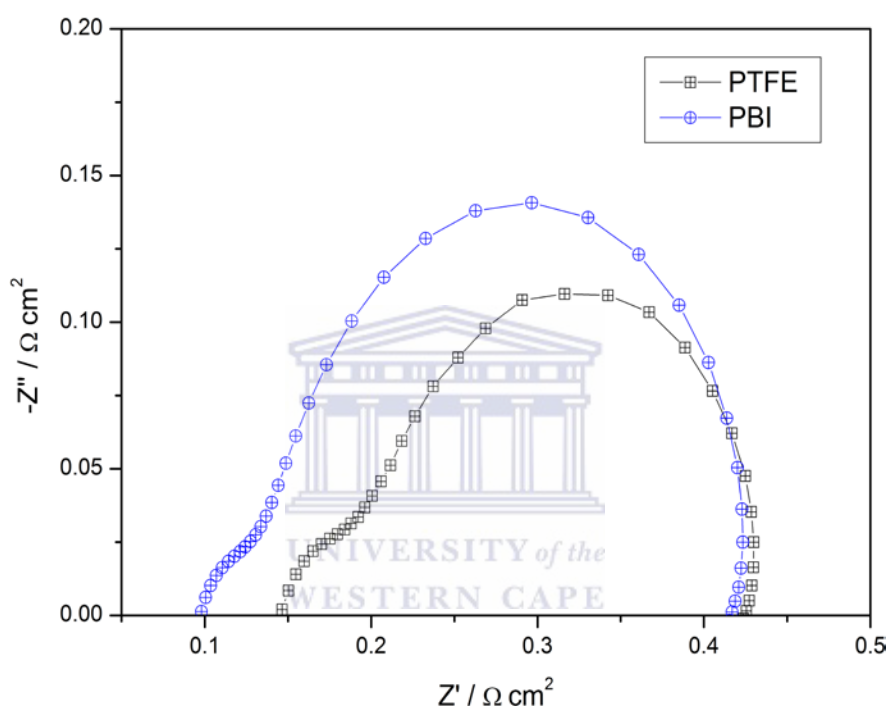


Fig. 6.30 *In-situ* impedance curves for MEAs comprised of Freudenberg CX 196 GDEs with 0.2 mg cm⁻² *SiC* and various polymers, with 2 mg cm⁻² PA doping (anode and cathode), at a cell voltage of + 0.6 V.

Table 9 - Impedance and *Tafel slope* characteristics of the MEAs with different binders in *SiC* layer.

Polymer	R_{Ω} (mΩ cm ⁻²)	R_{CT} (mΩ cm ⁻²)	<i>Tafel slope</i> (mV dec ⁻¹)
PTFE	142.86	280.80	97
PBI	95.65	319.79	100

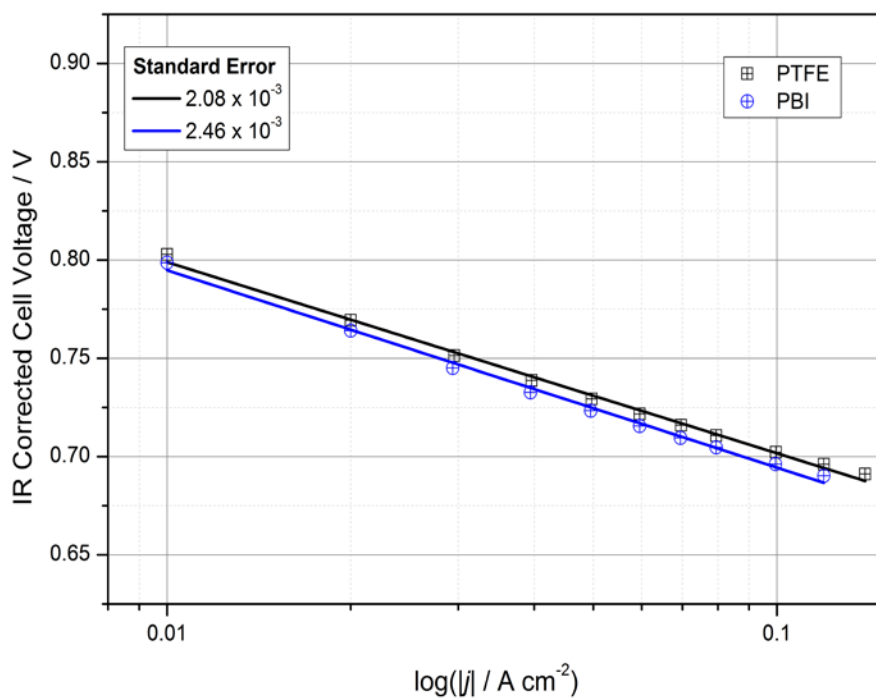


Fig. 6.31 Tafel plots for the ORR of the Freudenberg CX 196 GDEs with different polymers in the SiC layer.

6.2.2.4 Influence of NbC layer

In the following section *NbC* is used to form the acid-controlling region. The performance curves for MEAs of the *NbC* GDE versus the Freudenberg CX 196 GDE is illustrated in **Fig. 6.32**. The MEAs exhibit similar electrode kinetics but differ in their ohmic and mass transport characteristics, with the MEA of the *NbC* GDE exhibiting a higher decreasing slope as well as exhibiting a steeper decline in the mass transport region, indicating that the standard GDE has better mass transport characteristics than the *NbC* GDE.

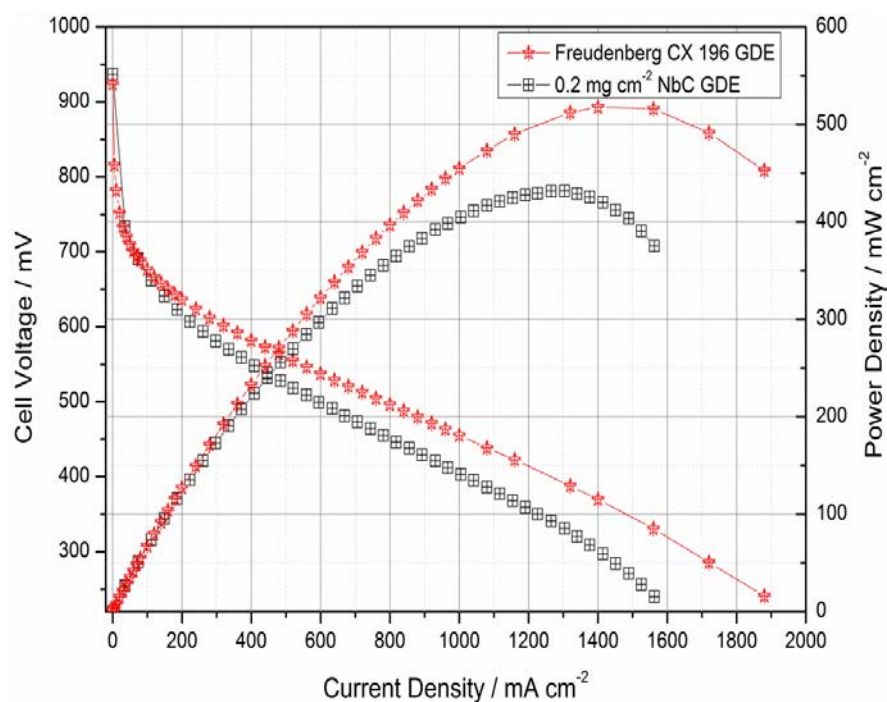


Fig. 6.32 Performance curves comparing MEAs of Freudenberg CX 196 GDE with Freudenberg CX 196 GDE with 0.2 mg cm^{-2} NbC layer doped with 2 mg cm^{-2} PA (anode and cathode).

In addition to these characteristics, the MEA of the NbC GDE achieves the lower peak power of 431 mW cm^{-2} at a cell voltage of $+331 \text{ mV}$, which is a performance decrease of $\sim 20\%$ when compared to the standard MEA. **Fig. 6.33** depicts the *in-situ* impedance curves for the MEAs of the NbC GDE and the Freudenberg CX 196 GDE. We can see that the R_Q for the MEA of the standard Freudenberg CX 196 GDE is lower than the MEA of the NbC GDE. This increase in R_Q was also observed for the MEA of the 0.2 mg cm^{-2} SiC GDE doped with 2 mg cm^{-2} PA, with the same cause as stated in that case. The impedance and *Tafel slope* values for the MEAs are shown in **Table 10**, with the *Tafel plots* shown in **Fig. 6.34**. Addition of the NbC layer to the standard Freudenberg CX 196 GDE has a significant effect on the *Tafel slope* values obtained, effectively increasing the *Tafel slope* indicating that the NbC GDE has poorer ORR kinetics.

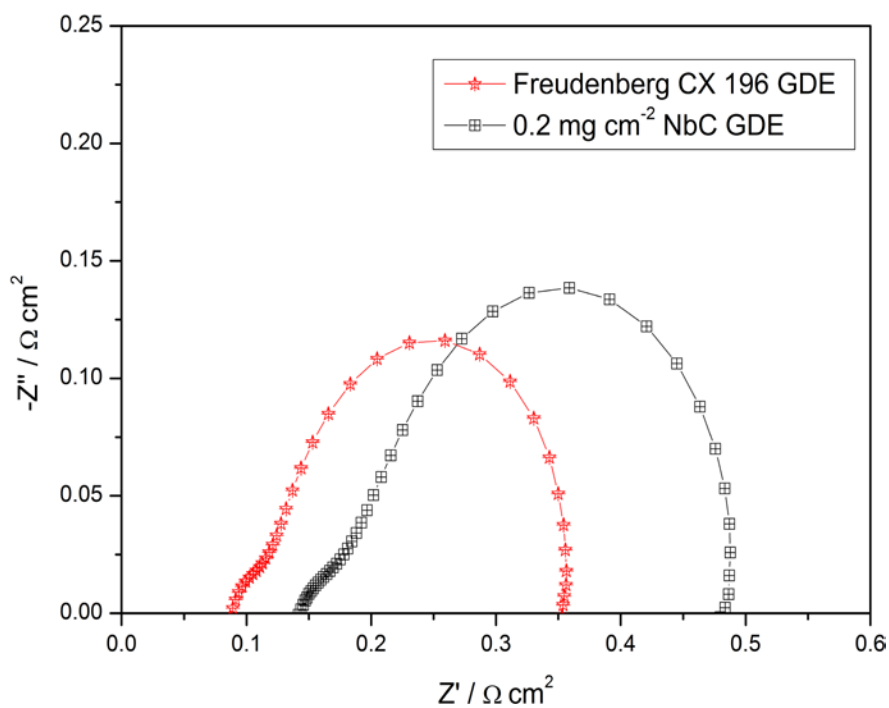


Fig. 6.33 *In-situ* impedance curves comparing MEAs of Freudenberg CX 196 GDE and Freudenberg CX 196 GDE with 0.2 mg cm^{-2} NbC and 40% PTFE layer, doped with 2 mg cm^{-2} PA (anode and cathode), at a cell voltage of +0.6 V.

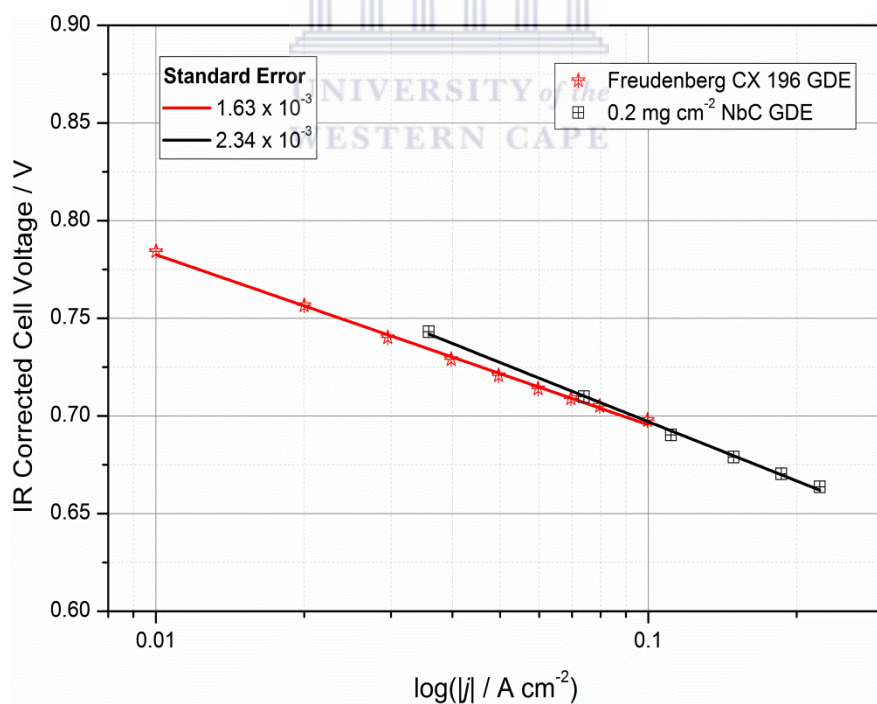


Fig. 6.34 Tafel plots for the ORR of the Freudenberg CX 196 GDEs with different structures.

6.2.2.5 Effect of NbC addition to SiC layer

Fig. 6.35 illustrates the effect of NbC addition to the SiC layer on the MEA performance. The experiments were conducted to determine whether addition of NbC to the SiC layer could improve the performance of the SiC MEA. Addition of NbC to the SiC layer, had no effect on improving the SiC MEA performance, regardless of the concentration of NbC added to the SiC layer. The NbC MEAs performance was however, improved when SiC was used as the primary metal carbide in the acid-controlling region.

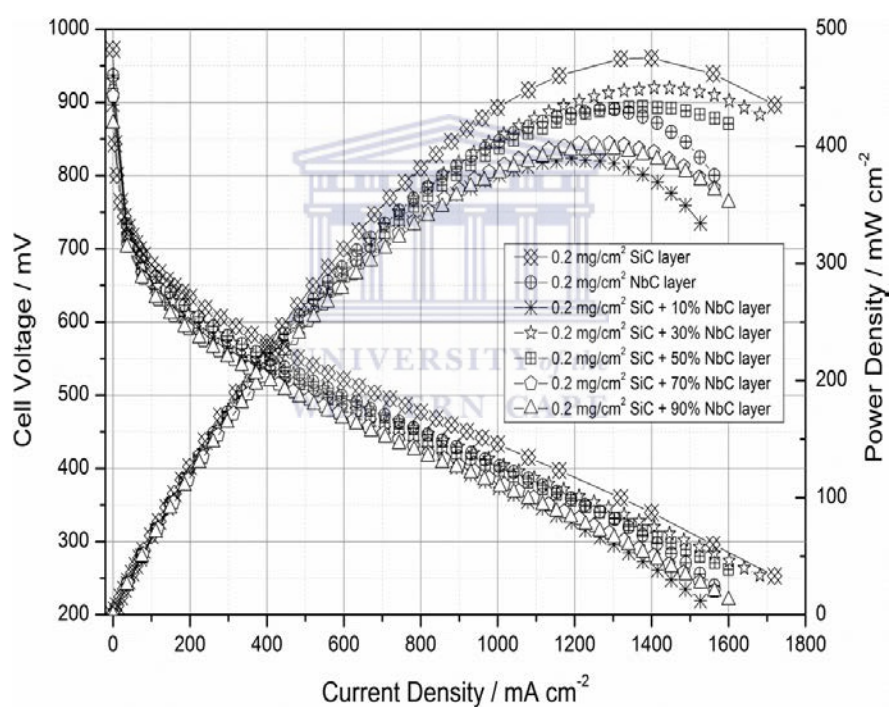


Fig. 6.35 Performance curves comparing MEAs of Freudenberg CX 196 GDE with various SiC, NbC and combinations of SiC/NbC layers doped with 2 mg cm⁻² PA (anode and cathode).

This improved performance was, however, only observed for the SiC/30 wt.% NbC and the SiC/50 wt.% NbC MEAs, with the SiC/30 wt.% NbC MEA providing the best improvement in performance of ~4% when compared to the solely NbC MEA. Although the SiC/30 wt.% NbC MEA provides an improvement in cell performance

when compared to the solely *NbC* MEA, the *SiC* MEA, however, exhibits the lowest voltage drop over all current density regions.

Table 10 - Impedance and Tafel slope characteristics of the Freudenberg CX 196 MEAs with *SiC* and/or *NbC* layers.

GDE	R_{Ω} (m Ω cm ⁻²)	R_{CT} (m Ω cm ⁻²)	Tafel slope (mV dec ⁻¹)
Freudenberg CX 196	87.25	265.75	90
0.2 mg cm ⁻² <i>SiC</i>	142.86	280.80	97
0.2 mg cm ⁻² <i>NbC</i>	141.82	338.03	101
<i>SiC</i> /10 % <i>NbC</i>	167.33	353.12	98
<i>SiC</i> /30% <i>NbC</i>	130.90	313.76	100
<i>SiC</i> /50% <i>NbC</i>	151.12	351.71	99
<i>SiC</i> /70% <i>NbC</i>	177.67	418.48	103
<i>SiC</i> /90% <i>NbC</i>	161.50	429.31	98

The *NbC* in conjunction with *SiC* in this case clearly had no effect in improving the cell performance, unlike the results obtained by Caires *et al.*[140] where a *SiC*/50 wt.% *NbC* combination improved the performance of a PAFC prepared with the conventional screen printed *SiC* matrix. It should, however, be noted that the matrix in this case was self-supported and the thickness of the prepared matrix also varied. Upon analysis of the linear region of the polarisation curve it can be seen that there is a pronounced variation with the slopes of the curves with the metal carbide layer composition, indicating that *NbC* exerts a significant influence on the electrolyte retaining capability of the acid-controlling region.

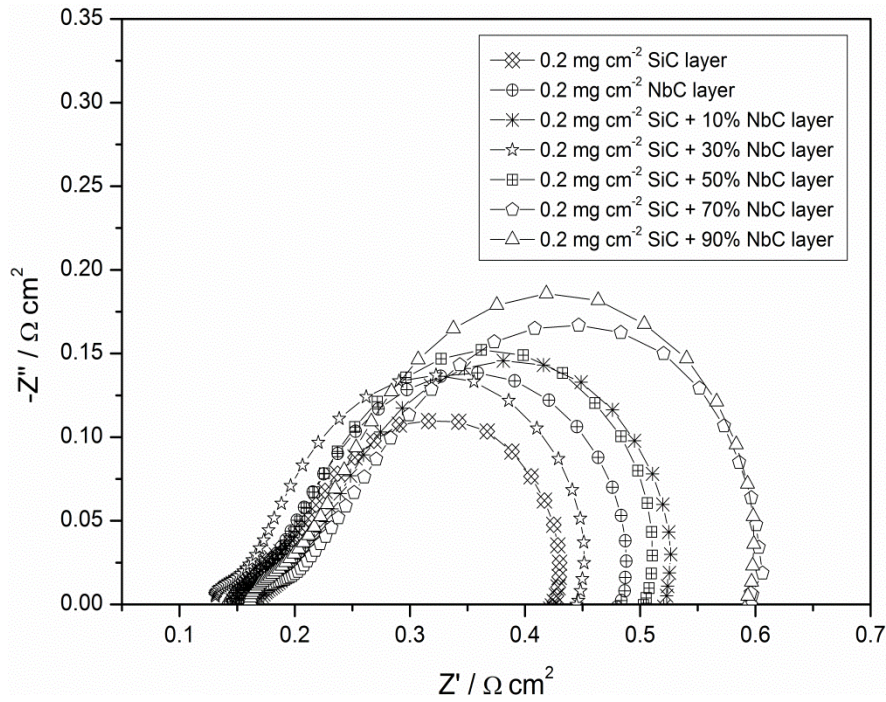


Fig. 6.36 *In-situ* impedance curves for the various ceramic carbide layers, at a cell voltage of +0.6V.

The *in-situ* impedance curves for the various ceramic carbide layers are depicted in **Fig. 6.36** and the electrochemical resistances and *Tafel slope* values for these MEAs and the standard MEA are shown in **Table 10**. It is evident from the high frequency intercepts on the x -axis that the MEAs all exhibit different ohmic resistances. Since the ohmic resistance is greatly influenced by the resistance of the electrolyte, and since the *SiC/30 wt.% NbC* MEA shows the lowest R_{Ω} value of $130.90 \text{ m}\Omega \text{ cm}^{-2}$, we can assume that the porous microstructure of this GDE is better able to retain the PA electrolyte. The pore-size intrusion data obtained for this GDE shown in **Fig. 6.13** shows a reduced number of macropores which would be beneficial for the electrolyte retaining capability of the ceramic carbide layer. This can be attributed to the reduced number of macropores which leads to a decrease in hydrostatic pressure the capillaries [140]. Since all of the composite *SiC/NbC* MEAs don't exhibit this low R_{Ω} value, an optimum value of *NbC* in the *SiC/NbC* GDE exists. The higher R_{Ω} values exhibited by

the other *SiC/NbC* MEAs correspond to the higher quantity of macropores exhibited by these *SiC/NbC* GDEs in **Fig. 6.13**, therefore the pore structure of the ceramic carbide layer significantly influences the ohmic resistance of the MEAs [49].

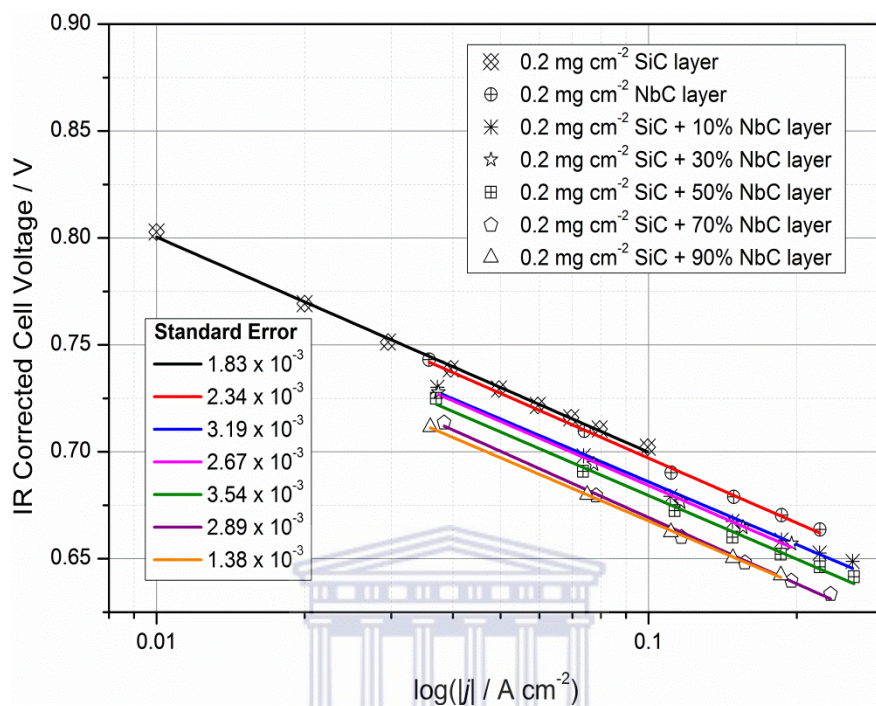


Fig. 6.37 Tafel plots for the ORR of the Freudenberg CX 196 GDEs with varying carbide layers.

Although the *SiC/30 wt.% NbC* MEA exhibited the lowest R_Q value, this was however, not the case for the R_{CT} value, the lowest charge transfer resistance was exhibited by the *SiC* MEA, which had a R_{CT} value of $280.80 \text{ m}\Omega \text{ cm}^{-2}$. Concerning the different R_{CT} values obtained it is obvious that the pore structure of the ceramic carbide layers affects not only the ohmic resistance of the MEAs but the charge transfer resistance as well. If we consider that all the ceramic carbide GDEs, excluding the *SiC*-GDE and the *SiC/30 wt.% NbC*-GDE, had higher intrusion volumes in the macropore region, it becomes clear that these ceramic carbide layers do not have suitable pore structures capable of retaining the PA electrolyte. This results in electrolyte flooding the catalyst layers, causing a decrease in the triple phase boundary area and increasing the resistance to proton transport, hence increasing the

charge transfer resistance for these MEAs. **Fig. 6.37** shows that the *Tafel slopes* values obtained are all close to 100 mV dec^{-1} for all the ceramic carbide GDEs, indicating that the ORR mechanism is the same in the presence of the different ceramic carbide layers.

6.2.2.6 Stability

Fig. 6.38 shows the short term stability analyses performed for 500 h at $j = 0.2 \text{ A cm}^{-2}$ on the standard Freudenberg CX 196 GDE and the ceramic carbide GDE which gave the best performance; the $0.2 \text{ mg cm}^{-2} \text{ SiC}$ layer GDE doped with $2 \text{ mg cm}^{-2} \text{ PA}$. The experiments were started after performing two polarisation analyses which took place on two consecutive days. The cell voltage at 0.2 A cm^{-2} was at a maximum after the second polarisation test was performed. It is evident that the *SiC* MEA shows a relatively stable voltage profile throughout the duration of the study, whereas the standard Freudenberg MEA exhibits a voltage profile with two distinct periods: during the first 300 h the voltage profile is relatively stable, while for the remaining 200 h of the test a sharper decrease in voltage is observed.

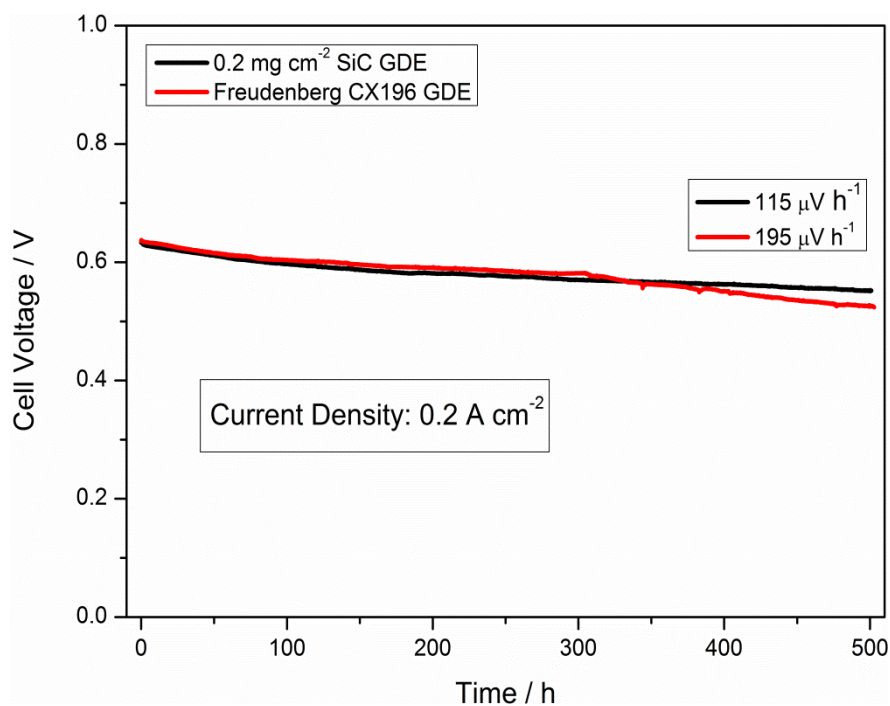


Fig. 6.38 Stability of the standard MEA and the *SiC* MEA, operating for 500 h at 0.2 A cm⁻².

This sharper decrease in voltage after 300 h for the standard Freudenberg CX 196 MEA could be attributed to electrolyte loss. The voltage decay rates obtained by linear regression of the cell voltage data reveals that the *SiC* MEA has a voltage decay rate of 115 μV h⁻¹, which is approximately 41% lower than the voltage decay rate of 195 μV h⁻¹ obtained by the standard Freudenberg CX 196 MEA. Although the voltage decay rates exhibited here are higher than those reported (4.9-25 μV h⁻¹) by other researchers [130-134], it is most likely due to the airbrush spray method used to prepare the GDEs. The addition of the *SiC* acid-controlling layer serves to improve the durability of the fuel cell by (i) acting as a barrier to control the amount of electrolyte that enters the catalyst layer and, (ii) minimising the loss of electrolyte.

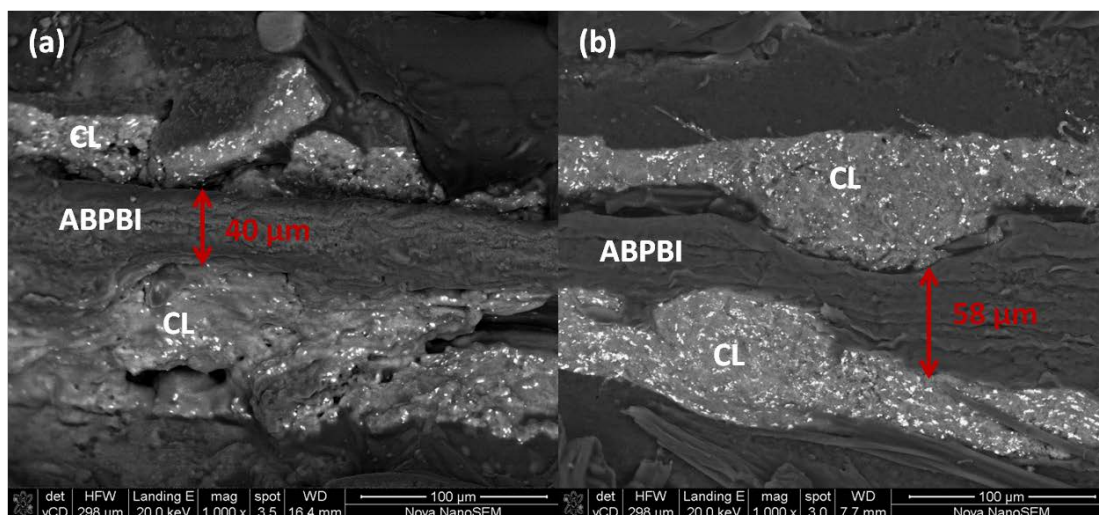


Fig. 6.39 SEM images of the cross-sections of the MEAs after the durability test: (a) Freudenberg CX 196 MEA and (b) *SiC* MEA

SEM was performed on the cross-sections of the MEAs after the stability tests, the post-test analyses images are shown in **Fig. 6.39**. The MEAs were set in resin and polished in order to obtain accurate cross-sections. Comparison of the two MEAs shows that the Freudenberg CX 196 MEA (**Fig. 6.39(a)**) has a membrane thickness of approximately 40 μm, while the untested doped membrane has a thickness of ~80 μm, which can be significantly reduced by cell compression of the MEA. The *SiC* MEA (**Fig. 6.39(b)**) on the other hand has a membrane thickness of 58 μm, which suggests that this membrane retains a higher PA doping level than the Freudenberg CX 196 MEA after the test. This is most likely due to the *SiC* layer acting as a barrier to prevent excessive leaching of PA electrolyte from the membrane. It can also be noted that the Freudenberg CX 196 MEA, shows catalyst layers that are detached from the membrane, although the *SiC* MEA exhibits some detachment of the catalyst layers from the membrane, the detachment is not as severe as in the Freudenberg CX 196 MEA. The good durability of the *SiC* MEA can be attributed to its unique structure which improves the acid-retaining capability of the MEA.

6.3 Conclusions

The use of *SiC*, *NbC* and composite *SiC/NbC* layers significantly influenced the porous microstructure and performance of these GDEs. Pore structures of the ceramic carbide layers influenced both the ohmic and charge transfer resistances of the MEAs. Although the addition of 30wt. % *NbC* to the *SiC* layer improved the ohmic resistance of the MEA, the charge transfer resistance was in fact higher than the acid-controlling region composed solely of *SiC*. The lower ohmic resistance for the *SiC*/30wt. % *NbC* MEA could be indicative of the layers improved electrolyte retention capability, but since no increase in performance was observed we can conclude that the electrolyte blocked the pores in the electrode. All other MEAs with composite *SiC/NbC* layers showed lower performances' than the MEA composed solely of an *SiC* layer, indicating that the addition of *NbC* to the *SiC* layer does not improve the properties of the acid-controlling region. Improvement in MEA durability was attained when unique GDEs were prepared by employing a novel *SiC* acid-controlling region in conjunction with an electrolyte membrane. The optimum *SiC* layer thickness and PA doping was found to be 0.2 mg cm^{-2} and 2 mg cm^{-2} respectively, these parameters yielded an MEA which achieved a peak power of 475 mW cm^{-2} at a cell voltage of 340 mV. Although the performance of the *SiC* MEA was slightly lower than that of the Freudenberg CX 196 MEA, the *SiC* MEA exhibited improved stability and displayed a voltage decay rate 48% lower than that of the Freudenberg CX 196 MEA. The higher durability exhibited by the *SiC* MEA can be attributed to the MEAs unique structure which not only acts a barrier to prevent excessive phosphoric acid from flooding the electrode, but also serves to reduce phosphoric acid leaching from the MEA.

Chapter 7: Final conclusions, Recommendations, Future work and Outputs

7.1 Final conclusions

The influence of different additives, $CsHSO_4$ and ZHP, incorporated in the CL of GDEs was evaluated with regards to improving the proton conductivity in the CL and improving the overall performance of the HT-MEAs. Concerning $CsHSO_4$; different $CsHSO_4$ loadings were evaluated as well as different binder- $CsHSO_4$ configurations in the CL. When $CsHSO_4$ was used on its own in the CL, lower proton conductivities and performances' were observed, however, improvement in proton conductivity and performance was observed upon addition of a binder to the CL. This observation can only be the result of the improved structural integrity gained by the addition of a binder to the $CsHSO_4$ CL. The PVDF- $CsHSO_4$ binder configuration provided the best performance of the MEAs containing $CsHSO_4$ in the CL. Comparison of the MEAs comprised of the PVDF-GDE and the PVDF- $CsHSO_4$ revealed that the PVDF- $CsHSO_4$ MEA exhibited a performance ~15% lower than the MEA of the PVDF-GDE. Although $CsHSO_4$ in the CL did not prove beneficial for enhancement of HT-MEA performance, further modification of $CsHSO_4$ could lead to the desired performance enhancement.

The addition of an optimum amount of ZHP to a PTFE GDE proved to improve not only the proton conductivity and cell performance, but the stability of the MEAs as well. A content of 30wt. % ZHP (re. dry PTFE) was found to be optimum in the CL for performance enhancement. Durability analysis revealed that the 30wt. % ZHP MEA showed a 90% improvement in MEA stability, which can be attributed to ZHP's

good thermal properties as well as its hygroscopic nature which serves to aid phosphoric acid hydration.

The introduction of a ceramic carbide layer as an acid-controlling region in the MEA structure revealed that the MEA performance for these MEAs depends not only on the kind of ceramic carbide used, but also on the thickness and doping level of the layer. The best performance was achieved with a 0.2 mg cm^{-2} *SiC* layer loading and a phosphoric acid doping of 2 mg cm^{-2} H_3PO_4 . A performance loss of ~8% is observed when compared to a standard MEA with no *SiC* layer, although this is an acceptable loss if we consider that the stability tests showed that the *SiC* MEA showed a ~70% improvement in durability when compared to the standard MEA. The improved durability can be attributed to the *SiC* acid-controlling region preventing excess phosphoric acid from flooding the electrodes as well as improving the MEAs phosphoric acid retention capability, since deterioration in durability arises not only from Pt deactivation due to phosphate anion adsorption but also from loss of phosphoric acid from the membrane.

7.2 Recommendations and Future work

The incorporation of ZHP into the CL proved to be beneficial for MEA stability and performance, as such the influence of ZHP on MEA performance and stability should be further evaluated at temperatures above 160 °C. A further effort should be made to see the influence of ZHP on MEA performance if the catalyst loading is reduced. In addition to these studies, efforts should be made to investigate the influence of varying *CO* concentrations in the fuel feed on ZHP MEAs performance and stability behaviour. The inclusion of a SiC acid-controlling region improved the durability of HT-MEAs, it would prove beneficial to evaluate the durability of these MEAs under different operational parameters, including but not restricted to; *CO* in the anode feed, higher operating temperature, stoichiometric reactant flow rates, *etc.* A great deal of knowledge was gained in the study of catalyst layer additives for improved proton conductivity and performance as well as modification of the MEA structure for durability enhancement. As such, future work will focus on lowering the catalyst loading and improving the performance by using automated deposition methods as well as incorporating additives such as ZHP into these catalyst layers. Once performance enhancement is attained with these GDEs, the MEAs will be upscaled and modified with an acid-controlling region for testing in a small stack, where phosphoric acid loss and durability amongst other properties will be evaluated.

7.3 Outputs

7.3.1 Publications

[1] Olivia Barron, Huaneng Su, Vladimir Linkov, Bruno G. Pollet, Sivakumar Pasupathi, *CsHSO₄ as proton conductor for high temperature polymer electrolyte membrane fuel cells*, Journal of Applied Electrochemistry 44 (2014) 1037-1045.

[2] Olivia Barron, Huaneng Su, Vladimir Linkov, Bruno G. Pollet, Sivakumar Pasupathi, *Enhanced performance and stability of high temperature proton exchange membrane fuel cell by incorporating zirconium hydrogen phosphate in catalyst layer*, Journal of Power Sources 278 (2015) 718-724.

[3] Olivia Barron, Huaneng Su, Vladimir Linkov, Bruno G. Pollet, Sivakumar Pasupathi, *Stability enhancement of high temperature proton exchange membrane fuel cell by development of acid-controlling region*.

Intended Journal: Journal of Power Sources

Status: To be submitted



[4] Huaneng Su, Cecil Felix, Olivia Barron, Piotr Bujlo, Bernard J. Bladergroen, Bruno G. Pollet, Sivakumar Pasupathi, *High-Performance and Durable Membrane Electrode Assemblies for High-Temperature Polymer Electrolyte Membrane Fuel Cells*, Electrocatalysis 5 (2014) 361-371.

[5] Huaneng Su, Ting-Chu Jao, Olivia Barron, Bruno G. Pollet, Sivakumar Pasupathi, *Low platinum loading for high temperature proton exchange membrane fuel cell developed by ultrasonic spray coating technique*, Journal of Power Sources 267 (2014) 155-159.

7.3.2 Conferences

[1] O. Barron, S. Pasupathi, V. Linkov, B. G. Pollet, *Zr(HPO₄)₂ in the catalyst layers of high temperature PEMFCs* (poster presentation), Carisma 2014, 1-3 December 2014, Cape Town, South Africa.

[2] O. Barron, S. Pasupathi, B. G. Pollet, *An investigation of CsHSO₄ ionomer and PTFE binder in catalyst layers of GDEs for HT-PEMFCs* (poster presentation), International Hydrogen and Fuel Cell Conference 12-15 July 2013, Napa Valley, California.

[3] O. Barron, S. Pasupathi, V. Linkov, B. G. Pollet, *Gas diffusion electrodes for high temperature PEMFCs* (poster), 13th Topical Meeting of the International Society of Electrochemistry, 7-10 April 2013, Pretoria, South Africa.



[4] S. Pasupathi, C. Felix, O. Barron, P. Bujlo, H. Su, B. Pollet, *HT-PEMFC components to systems – An overview of activities at HySA Systems*, 3rd CARISMA International Conference 2012, 3-5 September 2012, Copenhagen, Denmark.

References

1. Tominaka, S., et al., *Electrochemical analysis of perpendicular mesoporous Pt electrode filled with pure water for clarifying the active region in fuel cell catalyst layers*. Journal of Power Sources, 2010. **195**(8): p. 2236-2240.
2. Gode, P., et al., *Influence of the composition on the structure and electrochemical characteristics of the PEFC cathode*. Electrochimica Acta, 2003. **48**(28): p. 4175-4187.
3. Oono, Y., et al., *Influence of operating temperature on cell performance and endurance of high temperature proton exchange membrane fuel cells*. Journal of Power Sources, 2010. **195**(4): p. 1007-1014.
4. Sang Hern Seo, C.S.L., *A study on the overall efficiency of direct methanol fuel cell by methanol crossover current*. Applied Energy, 2010. **87**: p. 2597-2604.
5. Wannek, C., W. Lehnert, and J. Mergel, *Membrane electrode assemblies for high-temperature polymer electrolyte fuel cells based on poly(2,5-benzimidazole) membranes with phosphoric acid impregnation via the catalyst layers*. Journal of Power Sources, 2009. **192**(2): p. 258-266.
6. Shao, Y., et al., *Proton exchange membrane fuel cell from low temperature to high temperature: Material challenges*. Journal of Power Sources, 2007. **167**(2): p. 235-242.
7. Pan, C., et al., *Preparation and operation of gas diffusion electrodes for high-temperature proton exchange membrane fuel cells*. Journal of Power Sources, 2007. **172**(1): p. 278-286.
8. Lobato, J., et al., *Study of the influence of the amount of PBI-H₃PO₄ in the catalytic layer of a high temperature PEMFC*. International Journal of Hydrogen Energy, 2010. **35**(3): p. 1347-1355.
9. Dupuis, A.-C., *Proton exchange membranes for fuel cells operated at medium temperatures: Materials and experimental techniques*. Progress in Materials Science, 2011. **56**(3): p. 289-327.
10. Antolini, E. and E.R. Gonzalez, *Ceramic materials as supports for low-temperature fuel cell catalysts*. Solid State Ionics, 2009. **180**(9-10): p. 746-763.
11. Frey, T. and M. Linardi, *Effects of membrane electrode assembly preparation on the polymer electrolyte membrane fuel cell performance*. Electrochimica Acta, 2004. **50**(1): p. 99-105.
12. Zhang, Y., et al., *Study on a novel manufacturing process of membrane electrode assemblies for solid polymer electrolyte water*

- electrolysis*. Electrochemistry Communications, 2007. **9**(4): p. 667-670.
13. Tang, H., et al., *A comparative study of CCM and hot-pressed MEAs for PEM fuel cells*. Journal of Power Sources, 2007. **170**(1): p. 140-144.
 14. Cho, Y.-H., et al., *Effect of platinum amount in carbon supported platinum catalyst on performance of polymer electrolyte membrane fuel cell*. Journal of Power Sources, 2007. **172**(1): p. 89-93.
 15. Chris Yang, S.S., A.B. Bocarsly, S. Tulyani, J.B. Benziger, *A comparison of physical properties and fuel cell performance of Nafion and zirconium phosphate/Nafion composite membranes*. Journal of Membrane Science, 2004. **237**: p. 145-161.
 16. Marianowski, L.G., *160 °C Proton Exchange Membrane (PEM) Fuel Cell System Development*, 2001, Gas Technology Institute: Des Plaines.
 17. Prasanna, M., et al., *Influence of cathode gas diffusion media on the performance of the PEMFCs*. Journal of Power Sources, 2004. **131**(1-2): p. 147-154.
 18. Gervasio, D., *FUEL CELLS – PROTON-EXCHANGE MEMBRANE FUEL CELLS / Gas Diffusion Layers*, in *Encyclopedia of Electrochemical Power Sources*, J. Garche, Editor 2009, Elsevier. p. 806-809.
 19. M.T. Outeiro, R.C., A.S. Carvalho, A.T. de Almeida, *A parameter optimized model of a Proton Exchange Membrane fuel cell including temperature effects*. Journal of Power Sources, 2008. **185**(2): p. 952-960.
 20. Haile, S.M., *Fuel cell materials and components*. Acta Materialia, 2003. **51**: p. 5981-6000.
 21. Martin Winter, R.J.B., *What Are Batteries, Fuel Cells, and Supercapacitors?* Chemical Reviews, 2004. **104**: p. 4245-4269.
 22. Barbir, F., *PEM Fuel Cells: Theory and Practice*. 1 ed 2005: Elsevier Academic Press.
 23. Kirubakaran, A., S. Jain, and R.K. Nema, *A review on fuel cell technologies and power electronic interface*. Renewable and Sustainable Energy Reviews, 2009. **13**(9): p. 2430-2440.
 24. Grove, W.R., *The Correlation of Physical Forces*. 6 ed 1874, London: Longmans, Green & Co.
 25. Grove, W.R., *On the Gas Voltaic Battery. Voltaic Action of Phosphorus, Sulphur and Hydrocarbons* Philosophical Transactions of the Royal Society of London, 1845. **135**: p. 351-361.
 26. Grubb, W.T. and L.W. Niedrach, *Batteries with Solid Ion-Exchange Membrane Electrolytes: II . Low-Temperature*

- Hydrogen-Oxygen Fuel Cells*. Journal of the Electrochemical Society, 1960. **107**(2): p. 131-135.
27. R. Greyvenstein, M.C., W. Kriel, *South Africa's opportunity to maximise the role of nuclear power in the global hydrogen economy*. Nuclear Engineering and Design, 2008. **238**: p. 3031-3040.
 28. Hall, P.J., *Energy storage: The route to liberation from the fossil fuel economy?* Energy Policy, 2008. **36**: p. 4363-4367.
 29. M. Stanley Whittingham, R.F.S., Thomas Zawodzinski, *Introduction: Batteries and Fuel Cells*. Chemical Reviews, 2004. **104**(10): p. 4243-4244.
 30. Ball, M. and M. Wietschel, *The future of hydrogen – opportunities and challenges* ☆. International Journal of Hydrogen Energy, 2009. **34**(2): p. 615-627.
 31. Larminie, J., *Fuel Cells*, in *Kirk-Othmer Encyclopedia of Chemical Technology* 2005, John Wiley & Sons. p. 199-228.
 32. Barbir, F., *PEM Fuel Cells*, in *Fuel Cell Technology* 2006, Springer London. p. 27-51.
 33. Inc., E.G.T.S., *Fuel Cell Handbook* 7ed 2004, West Virginia: US Department of Energy.
 34. Mikkola, M., *Experimental Studies on Polymer Electrolyte Membrane Fuel Cell Stacks in Engineering Physics and Mathematics* 2001, Helsinki University of Technology. p. 106.
 35. Fan, S.S.M., *Performance Characterization of the High Temperature Direct Alcohol Fuel Cell*, in *Chemical and Biological Engineering* 2012, The University of British Columbia: Vancouver.
 36. Eddy De Geeter, M.M., Staf Spaepen, William Stinissen, Georges Vennekens, *Alkaline fuel cells for road traction*. Journal of Power Sources, 1999. **80**: p. 207-212.
 37. P. Gouérec, L.P., J. Denizot, E. Sanchez-Cortezon, J.H. Miners, *The evolution of the performance of alkaline fuel cells with circulating electrolyte*. Journal of Power Sources, 2004. **129**(193-204): p. 193.
 38. Bischoff, M., *Molten carbonate fuel cells: A high temperature fuel cell on the edge to commercialization*. Journal of Power Sources, 2006. **160**: p. 842-845.
 39. L. Carrette, K.A.F., U. Stimming, *Fuel Cells - Fundamentals and applications*. Fuel Cells, 2001. **1**(1): p. 5-39.
 40. Morita H, K.M., Mugikura Y, Izaki Y, Watanabe T, Masuda Y, et al., *Performance analysis of molten carbonate fuel cell using a Li/Na electrolyte*. Journal of Power Sources, 2002. **112**: p. 509-518.

41. K. Tanimoto, T.K., M. Yanagida, K. Nomura, Y. Miyazaki, *Optimization of the electrolyte composition in a $(Li_{0.52}Na_{0.48})_{2-2x}AE_xCO_3$ ($AE = Ca$ and Ba) molten carbonate fuel cell*. Journal of Power Sources, 2004. **131**: p. 256-260.
42. Dicks, A.L., *Molten carbonate fuel cells*. Current Opinion in Solid State and Materials Science, 2004. **8**: p. 379-383.
43. Minh, N.Q., *Solid oxide fuel cell technology—features and applications*. Solid State Ionics, 2004. **174**: p. 271-277.
44. Badwal, S.P.S., *Stability of solid oxide fuel cell components*. Solid State Ionics, 2001. **143**: p. 39-46.
45. Bin Lin, S.W., Xingqin Liu, Guangyao Meng, *Simple solid oxide fuel cells*. Journal of Alloys and Compounds, 2010. **490**: p. 214-222.
46. Aschenbrenner, N., *Gentle Energy*, in *Pictures of the Future 2002*, www.siemens.com.
47. Nigel Sammes, R.B., Knut Stahl, *Phosphoric acid fuel cells: Fundamentals and applications*. Current Opinion in Solid State and Materials Science, 2004. **8**: p. 372-378.
48. J. Larminie, A.D., *Fuel cell systems explained 2000*, London: John Wiley & Sons, Inc.
49. Rak-Hyun Song, S.D., Dong-Ryul Shin, *Effect of silicon carbide particle size in the electrolyte matrix on the performance of a phosphoric acid fuel cell*. Journal of Power Sources, 2002. **106**: p. 167-172.
50. M. Neergat, A.K.S., *A high-performance phosphoric acid fuel cell*. Journal of Power Sources, 2001. **102**: p. 317-321.
51. E. Passalacqua, P.L.A., M. Vivaldi, A. Patti, V. Antonucci, N. Giordano, K. Kinoshita, *The influence of Pt on the electrooxidation behavior of carbon in phosphoric acid*. Electrochimica Acta, 1992. **37**(15): p. 2725-2730.
52. S.K. Kamarudin, F.A., W.R.W. Daud, *Overview on the application of direct methanol fuel cell (DMFC) for portable electronic devices*. International Journal of Hydrogen Energy, 2009. **34**: p. 6902-6916.
53. Satterfield, M.B., et al., *Mechanical properties of Nafion and titania/Nafion composite membranes for polymer electrolyte membrane fuel cells*. Journal of Polymer Science Part B: Polymer Physics, 2006. **44**(16): p. 2327-2345.
54. T.S. Zhao, C.X., R. Chen, W.W. Yang, *Mass transport phenomena in direct methanol fuel cells*. Progress in Energy and Combustion Science 2009. **35**: p. 275-292.
55. Jianbing Zang, L.D., Yingdan Jia, Hong Pan, Zhenzhen Gao, Yanhui Wang, *Core-shell structured SiC@C supported platinum*

- electrocatalysts for direct methanol fuel cells*. Applied Catalysis B: Environmental, 2014. **144**: p. 166-173.
56. Chandan, A., et al., *High temperature (HT) polymer electrolyte membrane fuel cells (PEMFC) – A review*. Journal of Power Sources, 2013. **231**: p. 264-278.
 57. Song, C. and J. Zhang, *Electrocatalytic Oxygen Reduction Reaction*, in *PEM Fuel Cell Electrocatalysts and Catalyst Layers*, J. Zhang, Editor 2008, Springer London. p. 89-134.
 58. Kucernak, A.R. and E. Toyoda, *Studying the oxygen reduction and hydrogen oxidation reactions under realistic fuel cell conditions*. Electrochemistry Communications, 2008. **10**(11): p. 1728-1731.
 59. Zhang, J., et al., *High temperature PEM fuel cells*. Journal of Power Sources, 2006. **160**(2): p. 872-891.
 60. Zhang, C.S.a.J., *PEM Fuel Cell Electrocatalysts and Catalyst Layers in Fundamentals and Applications*, J. Zhang, Editor 2008, Springer: London. p. 89-134.
 61. W.H.J. Hogarth, J.C.D.d.C., G.Q. Lu, *Solid acid membranes for high temperature (>140 °C) proton exchange membrane fuel cells*. Journal of Power Sources, 2005. **142**: p. 223-237.
 62. Hensley, J.E., et al., *The effects of thermal annealing on commercial Nafion® membranes*. Journal of Membrane Science, 2007. **298**(1-2): p. 190-201.
 63. Yang, C., *A comparison of physical properties and fuel cell performance of Nafion and zirconium phosphate/Nafion composite membranes*. Journal of Membrane Science, 2004. **237**(1-2): p. 145-161.
 64. P. Costamagna, C.Y., A.B. Bocarsly, S. Srinivasan, *Nafion 115/zirconium phosphate composite membranes for operation of PEMFCs above 100 °C*. Electrochimica Acta, 2002. **47**: p. 1023-1033.
 65. Tang, H., et al., *Self-assembled Nafion–silica nanoparticles for elevated-high temperature polymer electrolyte membrane fuel cells*. Electrochemistry Communications, 2007. **9**(8): p. 2003-2008.
 66. Cindrella, L., et al., *Surface modification of gas diffusion layers by inorganic nanomaterials for performance enhancement of proton exchange membrane fuel cells at low RH conditions*. International Journal of Hydrogen Energy, 2009. **34**(15): p. 6377-6383.
 67. E. Antolini, E.R.G., *Ceramic materials as supports for low-temperature fuel cell catalysts*. Solid State Ionics, 2009. **180**: p. 746-763.
 68. Antunes, R.A., et al., *Corrosion of metal bipolar plates for PEM fuel cells: A review*. International Journal of Hydrogen Energy, 2010. **35**(8): p. 3632-3647.

69. Nikam, V. and R. Reddy, *Corrugated bipolar sheets as fuel distributors in PEMFC*. International Journal of Hydrogen Energy, 2006. **31**(13): p. 1863-1873.
70. C. Yang, P.C., S. Srinivasan, J. Benziger, A.B. Bocarsly, *Approaches and technical challenges to high temperature operation of proton exchange membrane fuel cells*. Journal of Power Sources, 2001. **103**: p. 1-9.
71. A. Heinzl, G.B., W. Lehnert, *Fuel Cells – Proton-Exchange Membrane Fuel Cells | High Temperature PEMFCs*. Encyclopedia of Electrochemical Power Sources, 2009: p. 951-957.
72. Li, Q., et al., *The CO Poisoning Effect in PEMFCs Operational at Temperatures up to 200°C*. Journal of The Electrochemical Society, 2003. **150**(12): p. A1599-A1605.
73. Das, S.K., A. Reis, and K.J. Berry, *Experimental evaluation of CO poisoning on the performance of a high temperature proton exchange membrane fuel cell*. Journal of Power Sources, 2009. **193**(2): p. 691-698.
74. Cho, E., et al., *Characteristics of the PEMFC Repetitively Brought to Temperatures below 0°C*. Journal of The Electrochemical Society, 2003. **150**(12): p. A1667-A1670.
75. Qingfeng Li, R.H., Jens Oluf Jensen, and Niels J. Bjerrum, *Approaches and Recent Development of Polymer electrolyte membranes Operating at temperatures above 100°C*. Chemistry of Materials, 2003. **15**(26): p. 4896–4915.
76. Li, Q., et al., *High temperature proton exchange membranes based on polybenzimidazoles for fuel cells*. Progress in Polymer Science, 2009. **34**(5): p. 449-477.
77. Oono, Y., A. Sounai, and M. Hori, *Influence of the phosphoric acid-doping level in a polybenzimidazole membrane on the cell performance of high-temperature proton exchange membrane fuel cells*. Journal of Power Sources, 2009. **189**(2): p. 943-949.
78. Oh, H.-S., J.-H. Lee, and H. Kim, *Electrochemical carbon corrosion in high temperature proton exchange membrane fuel cells*. International Journal of Hydrogen Energy, 2012. **37**(14): p. 10844-10849.
79. Pollet, B., *Let's Not Ignore the Ultrasonic Effects on the Preparation of Fuel Cell Materials*. Electrocatalysis, 2014. **5**(4): p. 330-343.
80. J.I. Goldstein, D.E.N., P. Echlin, D.C. Joy, C. Fiori, E. Lifshin, *Scanning Electron Microscopy and X-ray Microanalysis: A text for Biologists, Materials Scientists and Geologists* 1981, New York: Plenum Press.

81. D.E. Newbury, D.C.J., P. Echlin, C.E. Fiori, J.I. Goldstein, *Advanced Scanning Electron Microscopy and X-ray Microanalysis* 1986, New York: Plenum Press.
82. Oatley, C.W., *The Scanning Electron Microscope, Part 1: The Instrument* 1972, London: Cambridge University Press.
83. J.I. Goldstein, D.E.N., P. Echlin, D.C. Joy, C.E. Lyman, E. Lifshin, L. Sawyer, J.R. Michael, *Scanning Electron Microscopy and X-ray Microanalysis* 3ed 2003, New York: Springer.
84. Rajarathnam, D.D., *Instrumental chemical analysis: Basic principles and techniques*, 2004.
85. Parikh, N., J.S. Allen, and R.S. Yassar, *Microstructure of Gas Diffusion Layers for PEM Fuel Cells*. *Fuel Cells*, 2012. **12**(3): p. 382-390.
86. Yuan, X., et al., *AC impedance technique in PEM fuel cell diagnosis—A review*. *International Journal of Hydrogen Energy*, 2007. **32**(17): p. 4365-4380.
87. Y. Oono, T.F., A. Sounaib, M. Horia, *Influence of operating temperature on cell performance and endurance of high temperature proton exchange membrane fuel cells*. *Journal of Power Sources*, 2010. **195**: p. 1007-1014.
88. Wainright, J.S., et al., *Acid-Doped Polybenzimidazoles: A New Polymer Electrolyte*. *Journal of The Electrochemical Society*, 1995. **142**(7): p. L121-L123.
89. Weng, D., et al., *Electro-osmotic Drag Coefficient of Water and Methanol in Polymer Electrolytes at Elevated Temperatures*. *Journal of the Electrochemical Society*, 1996. **143**(4): p. 1260-1263.
90. Kwon, K., et al., *Maximization of high-temperature proton exchange membrane fuel cell performance with the optimum distribution of phosphoric acid*. *Journal of Power Sources*, 2009. **188**(2): p. 463-467.
91. J.-T. Wang, R.F.S., J. Wainright, M. Litt and H. Yu, *A H₂/O₂ Fuel cell using acid doped polybenzimidazole as polymer electrolyte* *Electrochimica Acta*, 1996. **41**(2): p. 193-197.
92. Linares, J.J., et al. *Poly(2,5-benzimidazole) membranes: Physico-chemical characterization and high temperature PEMFC application*. 2011. Boston, MA.
93. Asensio, J., *Proton-conducting membranes based on poly(2,5-benzimidazole) (ABPBI) and phosphoric acid prepared by direct acid casting*. *Journal of Membrane Science*, 2004. **241**(1): p. 89-93.

94. J. A. Asensio, a.P.G.m.-R., *Recent developments on proton conducting poly(2,5-benzimidazole) (ABPBI) membrane for High Temperature Polymer Electrolyte membrane Fuel Cells*. Fuel Cells, 2005. **5**(3): p. 336-343.
95. Li Qingfeng, H.A.H., Niels J. Bjerrum, *Oxygen reduction on carbon supported platinum catalysts in high temperature polymer electrolytes*. Electrochimica Acta, 2000. **45**: p. 4219-4226.
96. Lobato, J., et al., *PBI-based polymer electrolyte membranes fuel cells Temperature effects on cell performance and catalyst stability*. Electrochimica Acta, 2007. **52**(12): p. 3910-3920.
97. Angioni, S., et al., *Novel aryloxy-polybenzimidazoles as proton conducting membranes for high temperature PEMFCs*. International Journal of Hydrogen Energy, 2011. **36**(12): p. 7174-7182.
98. Asensio, J.A., S. Borrós, and P. Gómez-Romero, *Enhanced conductivity in polyanion-containing polybenzimidazoles. Improved materials for proton-exchange membranes and PEM fuel cells*. Electrochemistry Communications, 2003. **5**(11): p. 967-972.
99. Carollo, A., et al., *Developments of new proton conducting membranes based on different polybenzimidazole structures for fuel cells applications*. Journal of Power Sources, 2006. **160**(1): p. 175-180.
100. Justo Lobato, P.C.n., Manuel A. Rodrigo, Diego Úbeda, F. Javier Pinar, *Enhancement of the fuel cell performance of a high temperature proton exchange membrane fuel cell running with titanium composite polybenzimidazole-based membranes*. Journal of Power Sources, 2011. **196**: p. 8265-8271.
101. Kumbharkar, S.C., et al., *Variation in acid moiety of polybenzimidazoles: Investigation of physico-chemical properties towards their applicability as proton exchange and gas separation membrane materials*. Polymer, 2009. **50**(6): p. 1403-1413.
102. Li, M. and K. Scott, *A polymer electrolyte membrane for high temperature fuel cells to fit vehicle applications*. Electrochimica Acta, 2010. **55**(6): p. 2123-2128.
103. Wang, R.F., et al., *Platinum free ternary electrocatalysts prepared via organic colloidal method for oxygen reduction*. Electrochemistry Communications, 2008. **10**(4): p. 523-526.
104. C. Hasiotis, V.D., C. Kontoyannis, *New polymer electrolytes based on blends of sulfonated polysulfones with polybenzimidazole*. Electrochimica Acta, 2001. **46**: p. 2401-2406.
105. Pinar, F.J., et al., *Titanium composite PBI-based membranes for high temperature polymer electrolyte membrane fuel cells. Effect on titanium dioxide amount*. RSC Advances, 2012. **2**(4): p. 1547.

106. Linares, J.J., et al., *Poly(2,5-benzimidazole) Membranes: Physico-Chemical Characterization Focused on Fuel Cell Applications*. Journal of The Electrochemical Society, 2012. **159**(7): p. F194-F202.
107. Fujigaya, T., M. Okamoto, and N. Nakashima, *Design of an assembly of pyridine-containing polybenzimidazole, carbon nanotubes and Pt nanoparticles for a fuel cell electrocatalyst with a high electrochemically active surface area*. Carbon, 2009. **47**(14): p. 3227-3232.
108. Jin, Y.C., M. Okada, and T. Hibino, *A comparative study of Pt/C cathodes in Sn_{0.9}In_{0.1}P₂O₇ and H₃PO₄ ionomers for high-temperature proton exchange membrane fuel cells*. Journal of Power Sources, 2011. **196**(11): p. 4905-4910.
109. Li, H. and S.J. Liao, *Preparation of large Co nanosheets with enhanced coercivity by a magnetic-field-assisted solvothermal approach free of surfactants, complexants or templates*. Journal of Magnetism and Magnetic Materials, 2009. **321**(17): p. 2566-2570.
110. P. Mazur, J.S., M. Paidar, K. Bouzek, *Gas diffusion electrodes for high temperature PEM type fuel cells-role of a polymer binder and method of the catalyst layer deposition*. Journal of Applied Electrochemistry, 2011. **41**: p. 1013-1019.
111. Su, H., et al., *Optimization of gas diffusion electrode for polybenzimidazole-based high temperature proton exchange membrane fuel cell: Evaluation of polymer binders in catalyst layer*. International Journal of Hydrogen Energy, 2013. **38**(26): p. 11370-11378.
112. Felix, C., et al., *Optimisation of electrophoretic deposition parameters for gas diffusion electrodes in high temperature polymer electrolyte membrane fuel cells*. Journal of Power Sources, 2013. **243**: p. 40-47.
113. Eiji Higuchi, K.O., Kenji Miyatake, and H.U.a.M. Watanabe, *Gas diffusion electrodes for polymer electrolyte fuel cell using suldonated polyimide*. Research on Chemical Intermediates, 2006. **32**(5-6): p. 533-542.
114. Justo Lobato, P.C., Manuel A, Rodrigo, Diego Úbeda, F. Javier. Pinar and J.J. Linares., *Optimisation of the Microporous Layer for a Polybenzimidazole-based High Temperature PEMFC. Effect of carbon content*. Fuel Cells, 2010. **10**(5): p. 770.
115. Park, J.O., Kwon, K., Cho, M.D., Hong, S.-G., Kim, T.Y., Yoo, D.Y., *Role of binders in HTPEMFC electrode abstract*. Journal of the Electrochemical Society, 2011. **158**(6): p. B675-B681.
116. Sossina M. Haile, D.A.B., Calum R. I. Chisholm & Ryan B. Merle, *Solid acids as fuel cell electrolytes*. Nature, 2001. **410**: p. 910-913.

117. Lavrova, G., et al., *Intermediate-temperature fuel cell based on the proton-conducting composite membranes*. *Solid State Ionics*, 2006. **177**(19-25): p. 2129-2132.
118. Piao, J., S. Liao, and Z. Liang, *A novel cesium hydrogen sulfate-zeolite inorganic composite electrolyte membrane for polymer electrolyte membrane fuel cell application*. *Journal of Power Sources*, 2009. **193**(2): p. 483-487.
119. Lee, H.-K., et al., *A study on the characteristics of the diffusion layer thickness and porosity of the PEMFC*. *Journal of Power Sources*, 2004. **131**(1-2): p. 200-206.
120. Kim, J.-R., J.S. Yi, and T.-W. Song, *Investigation of degradation mechanisms of a high-temperature polymer-electrolyte-membrane fuel cell stack by electrochemical impedance spectroscopy*. *Journal of Power Sources*, 2012. **220**: p. 54-64.
121. Clearfield, A. and J.A. Stynes, *The preparation of crystalline zirconium phosphate and some observations on its ion exchange behaviour*. *Journal of Inorganic and Nuclear Chemistry*, 1964. **26**(1): p. 117-129.
122. Alberti, G., et al., *On the mechanism of diffusion and ionic transport in crystalline insoluble acid salts of tetravalent metals—I Electrical conductance of zirconium bis (monohydrogen orthophosphate) monohydrate with a layered structure*. *Journal of Inorganic and Nuclear Chemistry*, 1978. **40**(3): p. 533-537.
123. Amani Al-Othman, A.Y.T., Wendy Pell, Sadok Letaief, and B.A.P. Tara J. Burchell, Marten Ternan, *Zirconium phosphate as the proton conducting material in direct hydrocarbon polymer electrolyte membrane fuel cells operating above the boiling point of water*. *Journal of Power Sources*, 2010. **195**: p. 2520-2525.
124. Amphlett, C.B., L.A. McDonald, and M.J. Redman, *Synthetic inorganic ion-exchange materials—I zirconium phosphate*. *Journal of Inorganic and Nuclear Chemistry*, 1958. **6**(3): p. 220-235.
125. Çelik, S.Ü., A. Bozkurt, and S.S. Hosseini, *Alternatives toward proton conductive anhydrous membranes for fuel cells: Heterocyclic protogenic solvents comprising polymer electrolytes*. *Progress in Polymer Science*, 2012. **37**(9): p. 1265-1291.
126. Yong-Il Park, J.-D.K., M. Nagai, *High proton conductivity in ZrP-PTFE composites*. *Journal of Material Science Letters* 2000. **19**: p. 1735-1738.
127. Hill, M.L., et al., *Zirconium hydrogen phosphate/disulfonated poly(arylene ether sulfone) copolymer composite membranes for proton exchange membrane fuel cells*. *Journal of Membrane Science*, 2006. **283**(1-2): p. 102-108.

128. Xie, Z., et al., *Gas diffusion electrodes containing ZHP/Nafion for PEMFC operation at 120°C*. Journal of Electroanalytical Chemistry, 2006. **596**(1): p. 38-46.
129. Su, H., et al., *A novel dual catalyst layer structured gas diffusion electrode for enhanced performance of high temperature proton exchange membrane fuel cell*. Journal of Power Sources, 2014. **246**: p. 63-67.
130. Su, H., et al., *Enhanced performance of polybenzimidazole-based high temperature proton exchange membrane fuel cell with gas diffusion electrodes prepared by automatic catalyst spraying under irradiation technique*. Journal of Power Sources, 2013. **242**: p. 510-519.
131. Thomas J. Schmidt, J.B., *Properties of high-temperature PEFC Celtec[®]-P 1000 MEAs in start/stop operation mode*. Journal of Power Sources, 2008. **176**: p. 428-434.
132. C.Wannek, B.K., H.-F.Oetjen, H. Lippert, and J. Mergel, *Durability of ABPBI-based MEAs for High Temperature PEMFCs at Different Operating Conditions*. Fuel Cells, 2008. **8**: p. 87-95.
133. S. Yu, L.X., and B. C. Benicewicz, *Durability Studies of PBI-based High Temperature PEMFCs*. Fuel Cells, 2008. **8**: p. 165-174.
134. A.D. Modestov, M.R.T., V.Ya. Filimonov, N.M. Zagudaeva, *Degradation of high temperature MEA with PBI-H₃PO₄ membrane in a life test*. Electrochimica Acta, 2009. **54**: p. 7121-7127.
135. Murahashi, T., *Reference Module in Chemistry, Molecular Sciences and Chemical Engineering* 2009: Elsevier.
136. Wannek, C., et al., *Redistribution of phosphoric acid in membrane electrode assemblies for high-temperature polymer electrolyte fuel cells*. International Journal of Hydrogen Energy, 2009. **34**(23): p. 9479-9485.
137. Zhai, Y., et al., *Degradation Study on MEA in H₃PO₄/PBI High-Temperature PEMFC Life Test*. Journal of The Electrochemical Society, 2007. **154**(1): p. B72-B76.
138. Matar, S., A. Higier, and H. Liu, *The effects of excess phosphoric acid in a Polybenzimidazole-based high temperature proton exchange membrane fuel cell*. Journal of Power Sources, 2010. **195**(1): p. 181-184.
139. Chang Sun Kong, D.-Y.K., Han-Kyu Lee, Yong-Gun Shul, Tae-Hee Lee, *Influence of pore-size distribution of diffusion layer on mass-transport problems of proton exchange membrane fuel cells*. Journal of Power Sources, 2002. **108**: p. 185-191.

140. M. I. Caires, M.L.B., E. A. Ticianelli, E. R. Gonzalez, *Preparation and characterization of matrices for phosphoric acid fuel cells*. Journal of Applied Electrochemistry, 1997. **27**: p. 19-24.
141. R.-H. Song, D.-J.K., C.-S. Kim and D.-R Shin, *Electrochemical evaluation of single cell in phosphoric acid fuel cell by ac impedance technique*. Journal of New Materials for Electrochemical Systems, 2001. **4**: p. 47-50.

